UNIVERSITY OF OKLAHOMA

GRADUATE COLLEGE

Signal Processing Techniques for Spatial and Frequency-Varying Wave Propagation Through Multi-Layer Stack-Ups

A DISSERTATION

SUBMITTED TO THE GRADUATE FACULTY

in partial fulfillment of the requirements for the

Degree of

DOCTOR OF PHILOSOPHY

By

RACHEL JARVIS

Norman, Oklahoma

2024

Signal Processing Techniques for Spatial and Frequency-Varying Wave Propagation Through Multi-Layer Stack-Ups

A DISSERTATION APPROVED FOR THE
SCHOOL OF ELECTRICAL AND COMPUTER ENGINEERING

BY THE COMMITTEE CONSISTING OF

Dr. Jay McDaniel, Chair

Dr. Justin Metcalf

Dr. Nathan Goodman

Dr. Hong Liu

Dr. Michael Detamore

Acknowledgments

The support and encouragement from my primary advisor and chair, Dr. Jay McDaniel, has been indispensable to my success as a graduate student and researcher. He showed me what it means to practice excellence while enjoying the journey. After 5 years of working together, Dr. McDaniel's attention to detail has been instilled into my daily practice. He has always pushed me to realize my full potential, even if I was not convinced at the time, and I would not have gotten my NSF Graduate Research Fellowship or tenure-track faculty position without his encouragement. In addition to all of the academic and professional support, Dr. McDaniel's friendship has been invaluable for my development as a person. Navigating new challenges as an adult, like first-time home ownership, was much better with his help (and copious amounts of his barbecue).

I would also like to thank Dr. Justin Metcalf for sharing his technical and professional expertise on this project. An interesting technical problem becomes even more fun to work on when all of the collaborators are invested in the cause driving the project. Dr. Metcalf has always supported my pursuit of my interests and worked hard to help me get where I wanted to go.

The collaborative environment at the Advanced Radar Research Center (ARRC) provided a sounding board for my present research and inspiration for future en-

deavors. The students, staff, and faculty have made me feel welcome to bring my whole self to work and have generously shared their many talents, interests, and expertise with me. In particular, I would like to thank Rylee Mattingly for collaborating with me on side projects and reminding me that there is a whole world to be excited about beyond my research project.

I am grateful for the National Science Foundation Graduate Research Fellowship that supported this work under Grant No. 20-34710. I would also like to thank all of the staff members of ARRC as well as the School of Electrical and Computer Engineering at the University of Oklahoma.

Finally, I would like to thank my parents, Marty and Karla Jarvis, and my grandparents, Jerald and Lois White, for their continued support throughout all of my academic and life endeavors. None of my work would have been possible without their sacrifices and encouragement.

Table of Contents

List of Tables

List of Figures

Abstract

Radar is classically used over optical sensors to sense objects regardless of weather or daylight conditions. In this case, a waveform is transmitted through the air and reflects off the outside of an object back to the radar. Radar has since been extended to sense within objects. Common applications are non-destructive evaluation, ground penetrating radar, and remote sensing. In this case, the incident wave is reflected by the contrast of electrical properties between materials. More recently, radar has been leveraged for biomedical applications, such as vital sign sensing and imaging within the body. Biomedical imaging radar (BIR) is a promising non-ionizing method to sense within the body. Some potential features to extract could be tumors, brain bleeds, or foreign objects.

A general assumption in radar operation is that the reflected waveform has the same structure as the transmitted waveform. The wave's velocity of propagation is dependent upon the medium and the frequency. Thus, if the reflected wave has traveled through a medium other than air, the received waveform is more stretched out in time than the transmitted waveform. Applying a traditional matched filter in this case yields a degraded range profile, and the returns do not appear at the correct physical location. If the wave only travels through air and one other non-dispersive medium, the range calculation can be easily adjusted. This scenario is

commonly encountered in remote sensing. However, more complex scenes such as the human body, are composed of several media with electrical properties that vary across frequency at different rates. Existing techniques are not able to fully leverage radar's pulse compression gain in this case.

In this research, the challenge of radar wave propagation through multiple media is addressed. First, the wave propagation mechanics are studied to understand how the received waveform is distorted. Then, a matched filter is adapted to compensate for this spatial and frequency-dependent distortion in the frequency-modulated continuous wave (FMCW) radar case. The compensation scheme is demonstrated in simulation, and then an FMCW prototype system is built to apply the velocity correction to measured data. The proposed compensation technique is successfully applied to measure a scene with a metal plate placed immersed in a box of oil at various ranges, and more advanced range profile enhancement is explored. The proposed technique is shown to overcome a crucial challenge faced by a BIR.

Chapter 1

Introduction

Classically, the signal of interest in radar operation is an electromagnetic reflection from the outside of an object, arriving at some time delay Δt, which is used to determine the object's location and velocity. The transmitted radar waveform propagates through the air, reflects off the outside of an object, and returns through air to the radar receiver, as illustrated in Fig. 1.1. Though this mode is most common, with applications such as air traffic control or weather radar, several important radar applications fall outside this modality. Ground penetrating radar and remote sensing aim to collect information from *internal* layers, either within the earth or within layers of snow and ice.

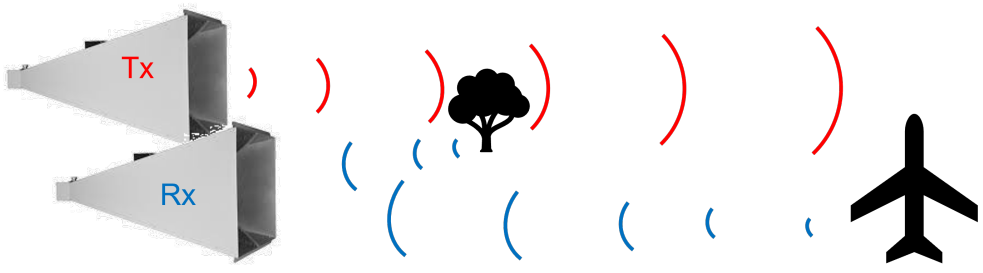

Figure 1.1: Illustration of classic radar operation with a transmitted electromagnetic wave reflection off of the outside of scatterers in free space

To extract information or form a radar image of an object, sufficient dynamic range and signal-to-noise ratio (SNR) are required. According to the radar range equation, the power received and, subsequently, the SNR can be increased by increasing the power transmitted [1]. Typical radar transmit power is limited by system component power handling or spectrum regulations set by the Federal Communications Commission (FCC). Because radar usually operates on inanimate objects, human safety is not considered in typical radar literature.

The radar return from the outside of an object is a function of the object's size, material, shape, and orientation as well as the operating frequency and polarization [2]. When radar is used instead to inspect a target's inside, the signal of interest is the power reflected at a boundary inside the object/ground rather than the initial air-object boundary. The amount of power reflected depends on the difference between the materials' wave impedances and how much power is attenuated on the way to and from that boundary. Air's conductivity is almost zero, and the attenuation as a wave propagates through the air is typically considered negligible [3]. On the other hand, many materials, such as biological tissue, are extremely lossy, and significantly attenuate propagating waves [4]. As a result, signals reflected from boundaries within the body will be very small. This power dissipation is challenging from a signal extraction standpoint, but the power absorption can also impact patient safety. If the layers are electrically thin, then the wave can re-reflect multiple times within layers before returning to the radar, creating a more complex range profile. Another consequence of propagating through different media is that the wave's velocity of propagation slows down in materials other than air. The generated range profile or image will be distorted if this change is not accounted for.

While microwave imaging radar has been proposed as a non-ionizing alternative to computed tomography (CT) scans, the power attenuated within the body is dissipated as heat, which can harm biological tissue [5, 6]. In the microwave frequency range, the International Commission on Non-Ionizing Radiation Protection (ICNIRP) defines restrictions in terms of specific absorption (SA) and absorbed energy density (U_{ab}) to ensure that the body is not heated above an unsafe level [7]. Both these quantities increase with increased incident power; thus, these regulations will limit the maximum transmitted power and, consequently, the SNR. Maintaining human safety is another consideration required in biomedical radar design.

Due to improvements in hardware dynamic range capabilities, biomedical imaging radar (BIR) at microwave frequencies is becoming more feasible [8, 9, 10]. For BIR to be robust enough to operate successfully in multiple areas of the body, several problems must be addressed. Even with high dynamic range performance, the skin reflection can still obscure the desired internal reflection. The skin reflection must be reduced either during the time of collection or in post-processing. The current BIR systems are faster than MRI, but collections can still last for several minutes. Implementing a more efficient radar architecture could improve image quality. Finally, several simplifications are often made on the behavior of the electromagnetic wave within the body that limit the areas of the body to which BIR can currently be applied. For example, techniques for breast tumor detection often assume a uniform velocity of propagation within the body. However, this assumption would not be acceptable when attempting to image a sinus cavity.

Ground penetrating radar (GPR) and remote sensing have been handling propagation through layered media for decades with varying strategies. Both Gaussian

UWB pulses and frequency-modulated continuous wave (FMCW) radar are implemented to measure layers of snow and ice [11, 12]. As the majority of these measurements are collected on a moving airborne platform, slower modalities like step frequency continuous wave (SFCW) are less practical for wide bandwidths. These snow measurements commonly assume a single, constant dielectric value when computing layer thicknesses [11, 12].

Variations in soil layer composition yield dielectric values that vary more than snow layers. Thus, techniques have been developed to mitigate distortion from varying permittivity along the path of wave propagation to correctly reconstruct the reflectivity of the underground object of interest. Often, a ray tracing approximation is applied to reconstruct the wave propagation through the layers [13]. Ray tracing assumes that the conductivity is low enough that attenuation is negligible within the layers, which is an acceptable approximation for soil. In [14], the compensation is instead calculated by the shape of the hyperbola parameters generated by point targets. This technique also assumes negligible soil conductivity and requires a point scatterer to be present in each layer. In [15], a ray tracing algorithm is adapted to map the velocity of propagation through each voxel in a holographic imaging mode of a breast phantom. This algorithm assumes that the velocity of propagation is constant over frequency.

While all materials have electrical properties that vary across frequency, the change in materials like dry air is negligible, even over wide bandwidths. However, as system bandwidth capabilities increase, the frequency-varying, or dispersive, behavior of materials begins to impact image quality because a changing permittivity alters the angle of refraction [3]. Using adaptations of techniques commonly em-

ployed in inverse scattering problems, a radar image can be formed of an object in a single known, dispersive medium [16].

This work aims to address variations in a radar waveform's velocity of propagation across both space and frequency to take advantage of radar enhancement techniques developed for other applications and construct an accurate representation of the physical scene. To initially address these challenges, this work focuses on a single range profile rather than an entire image. First, wave propagation through electrically thin multi-layer stackups is studied to calculate the boundary conditions between material layers. The results apply to a variety of problems, such as radar cross-section analysis or radiation safety evaluation, that analyze the wave propagation through electrically thin layers. Then, a technique is proposed to compensate for frequency and spatially varying electric properties in range profile creation. A MATLAB simulator is created for initial validation of the proposed techniques. Then, a prototype FMCW radar is assembled to measure layered media and further validate the proposed techniques. Finally, range sidelobe suppression techniques are adapted for the changing propagation velocity to improve the visibility of small scatterers. This technique could enhance existing ground penetrating radar imaging or unlock new BIR capabilities.

Chapter 2

Electromagnetic Propagation Within Layered Media

A radar observes the superposition of copies of the transmitted waveform reflected back from all scatterers within the scene, in addition to interference and noise. Then, the received samples are processed to learn more about the scatterers in the scene. Not all radar applications aim to capture reflections off objects that behave as point targets. Hence, a good understanding of how the incident wave might interact with the objects in the scene is crucial for proper reconstruction. This study requires some understanding of electromagnetic wave propagation and material properties.

2.1 Electromagnetic Fundamentals

The electric field of a forward-traveling wave in the z-direction of a lossy medium is given by

$$\mathbf{E}(z) = E_0 e^{-\gamma z} = E_0 e^{-(\alpha + j\beta)z} \tag{2.1}$$

where γ is the propagation constant, α is the attenuation constant (Np/m), and β is the phase constant (rad/m) [3]. The phase term is given by

$$\beta = \omega\sqrt{\mu\varepsilon}\left\{\frac{1}{2}\left[\sqrt{1+\left(\frac{\sigma}{\omega\varepsilon}\right)^2}+1\right]\right\}^{1/2} \tag{2.2}$$

where ω is the angular frequency, σ is electrical conductivity, and ε is permittivity. The values of σ, ε, and ω all affect α, given by

$$\alpha = \omega\sqrt{\mu\varepsilon}\left\{\frac{1}{2}\left[\sqrt{1+\left(\frac{\sigma}{\omega\varepsilon}\right)^2}-1\right]\right\}^{1/2} . \tag{2.3}$$

Permittivity is often provided in terms of a dielectric constant, which is the permittivity relative to free-space (ε_0), approximately equal to $\frac{1}{36\pi} \times 10^{-9}$ F/m. The relative permittivity (ε_r) for a general material is complex-valued, defined as

$$\varepsilon_r = \varepsilon_r' - j\varepsilon_r'' = \frac{\varepsilon}{\varepsilon_0} . \tag{2.4}$$

The real part of (2.4) represents the material's ability to store the energy of an externally applied electric field, while the imaginary component describes the loss [3]. The imaginary permittivity is related to the conductivity by

$$\sigma = \omega\varepsilon_r''\varepsilon_0 . \tag{2.5}$$

Another way to describe a material is by the loss tangent, defined as

$$\tan\delta = \frac{\varepsilon_r''}{\varepsilon_r'} . \tag{2.6}$$

The loss tangent is the ratio between energy lost to energy stored, derived from plotting ε_r' and ε_r'' on the complex plane. Thus, even if one material has a lower conductivity than another, the overall loss tangent can be higher, depending on ε_r'. Permeability describes a material's behavior in the presence of a magnetic field. The materials considered for multi-media propagation (e.g., snow, soil, human tissue) typically have a permeability equal to the free-space permeability, μ_0, which is approximately $4\pi \times 10^{-7}$ H/m.

The wavelength (λ) of an electromagnetic wave is given by

$$\lambda = \frac{2\pi}{\beta} \,, \tag{2.7}$$

and the velocity of propagation (v_p) is given by

$$v_p = \frac{\omega}{\beta} = \frac{\omega}{2\pi}\lambda \,. \tag{2.8}$$

It is important to note that the wavelength increases in media with a slower velocity of propagation. For a time-harmonic waveform, the time-averaged power density is related to the electric field ($\mathbf{E}$) and the magnetic field ($\mathbf{H}$) with Poynting's Theorem as follows:

$$S = \mathcal{R}(\mathbf{E} \times \mathbf{H}^*) \cdot \hat{\mathbf{n}} = \frac{|\mathbf{E}|^2}{2}\mathcal{R}\left\{\frac{1}{\eta^*}\right\} \tag{2.9}$$

where $\hat{\mathbf{n}}$ is the unit-normal vector to the body surface and η is the wave impedance of the material, given by [3] to be:

$$\eta = \sqrt{\frac{\mathrm{j}\omega\mu}{\sigma + \mathrm{j}\omega\varepsilon}}. \tag{2.10}$$

In radar applications, power magnitude is often represented on the decibel scale, with 0 dB representing 1 W and 0 dBm corresponding to 1 mW.

2.1.1 Modeling Material Behavior

Because the electrical properties of a material affect the rate and magnitude of wave propagation, as seen in (2.1) and (2.8), then it is essential to understand the material properties relevant to the application of interest. Several mechanisms may contribute to the material's electrical behavior on the molecular, atomic, and electronic levels. Materials with a consistent behavior across frequency are commonly used as substrates for circuit boards, but many everyday materials are somewhat or very dispersive over a wide bandwidth meaning that the group delay through the material is a function of frequency.

A material's permittivity behavior is a function of several mechanisms occurring within the material across the entire thickness, molecule, atom, and electron levels. For example, water has a high permittivity due to the strong dipole orientation [17]. On the other hand, ionic conduction is the primary driver behind the permittivity of borosilicate glass [18]. Each mechanism is associated with its own relaxation time or rate of dispersion, and one material likely has several contributing mechanisms that vary in contribution magnitude across frequency. The Cole-Cole and the Debye are two common models that represent this phenomenon mathematically. A number is often placed before the Cole-Cole to designate how many relaxation times (dispersions) are included in the model [19].

The 4-Cole-Cole model, commonly used to represent human tissue, is defined

as

$$\hat{\varepsilon}_r(\omega) = \varepsilon_\infty + \sum_{n=1}^{4} \frac{\Delta\varepsilon_n}{1 + (j\omega\tau_n)^{1-\alpha_n}} + \frac{\sigma_i}{j\omega\varepsilon_0} \tag{2.11}$$

where ε_∞ is the permittivity at field frequencies with $\omega\tau >> 1$, σ_i is the static ionic conductivity, n is the dispersion index, α describes the distribution of the dispersion, and the magnitude of each dispersion ($\Delta\varepsilon_n$) is defined as

$$\Delta\varepsilon = \varepsilon_\infty - \varepsilon_s \ . \tag{2.12}$$

On the other hand, the Debye model is a simplified version of the Cole-Cole, with α_n in (2.11) set to 0. The Debye complex permittivity is defined as

$$\varepsilon = \varepsilon_\infty + \frac{\varepsilon_s - \varepsilon_\infty}{1 + j\omega\tau} \tag{2.13}$$

where ε_s is the permittivity at field frequencies with $\omega\tau << 1$. While the Debye model does not include a parameter to represent the broadening of the dispersion distribution, the simpler equation is sometimes employed in high-efficiency applications [20].

2.2 Measurement of Material Properties

Electrical properties in literature are often only provided for a single frequency, and the measurement frequency is not always disclosed. However, the behavior of real-world materials can change significantly over frequency, particularly in the microwave frequency range, so using a single value introduces error in the propagation calculations. Therefore, the properties must be measured across the frequency

range of interest. In the 500 MHz to 20 GHz range, a vector network analyzer (VNA) is the most common measurement instrument. A VNA most commonly collects frequency-dependent scattering parameters, S_{11} and S_{21}, called the reflection and transmission coefficients, respectively. S_{11} measures the magnitude and phase received at port 1 relative to the power transmitted at port 1, while S_{21} measures the power received at port 2 relative to port 1. To extract information about a component, such as an amplifier or filter, the VNA ports are connected to the component through cables. However, for material characterization, there are no ports to plug cables into, so the fields must enter the material in a different manner.

If the size and shape of the material can be manipulated, the unknown material can be measured with the transmission line method. The material is embedded into a transmission line, such as a waveguide or coaxial cable, and the VNA collects transmission and reflection coefficient values through the transmission line [21]. The frequency capabilities of this measurement method depend on the size of the sample holder and the cutoff frequency of the transmission line [17]. Instead of shaping the material for the sample holder, an antenna can be placed on either side of the material for a free-space measurement method. In this case, the VNA collects reflection or transmission measurements of the fields propagating between the antennas to extract the electrical properties. The frequency range of this method depends on the antenna bandwidth as well as the size of the sample relative to the antenna aperture. At low frequencies, a large sample would be needed to fill the large antenna aperture [22].

Resonant structures can be used to evaluate a sample for relatively narrowband measurements. By including the unknown material in the resonant structure, the

sample properties can be extracted by the resonant frequency. This technique can be carried out with a resonant cavity, such as a cavity resonator, or a ring resonator can be placed on top of a material [23, 24]. This technique is often employed to measure the exact permittivity of a circuit board substrate, as the manufacturing process yields some variation across boards.

The open-ended coaxial probe method employs a fixture at the end of a coaxial transmission line to distribute fringing fields into the sample. The sample's properties affect the magnitude and phase of the fields reflected back to the VNA. In contrast to the transmission line and open air methods, the sample must be effectively infinitely thick, meaning that the majority of the fringing fields should be contained within the sample [17]. The most challenging aspect of this method is maintaining good contact with solid samples. An air gap between the probe and the sample yields measurement error.

Proper calibration is crucial for accurate results in all of the above methods. Even phase changes from moving cables can introduce errors. These methods generally assume the material is homogeneous, and the values are averaged across the sensing volume for inhomogeneous media. The best probe for a particular application will depend on the sample's mechanical properties, such as the shape and rigidity, the frequency range of interest, the size of the measurement bandwidth, and the budget.

The Keysight N1501A high temperature probe is used for measurements in this work as it is capable of operating over the entire frequency range of interest in a single capture using the open-ended coaxial probe method. The anticipated samples may be quite thick, flexible, or liquid, so the coaxial probe is valued for collecting

Figure 2.1: Measurement configuration for Keysight N1501A High Temperature Probe and Keysight Fieldfox

measurements without creating thin slabs of a certain thickness, like in the waveguide transmission line method [25]. The probe is operated with a Keysight FieldFox N9917B Portable Microwave Analyzer, and the Keysight Materials Measurement Suite is run on a Dell laptop. The probe is calibrated within the measurement software with measurements of the air, a short, and 23°C deionized water. The measurement software accounts for changes in water's permittivity over temperature, so the measured temperature is provided to the calibration configuration. Liquid samples are placed in a paper cup, as shown in Fig. 2.1, while solid samples are raised to the probe with a small scissor lift. For accurate results, the probe datasheet states that samples should be at least $20/\sqrt{|\overline{\varepsilon_r *}|}$ mm thick [26]. For example, if the sample has a relative permittivity of 3, the sample must be at least 11.6 mm thick.

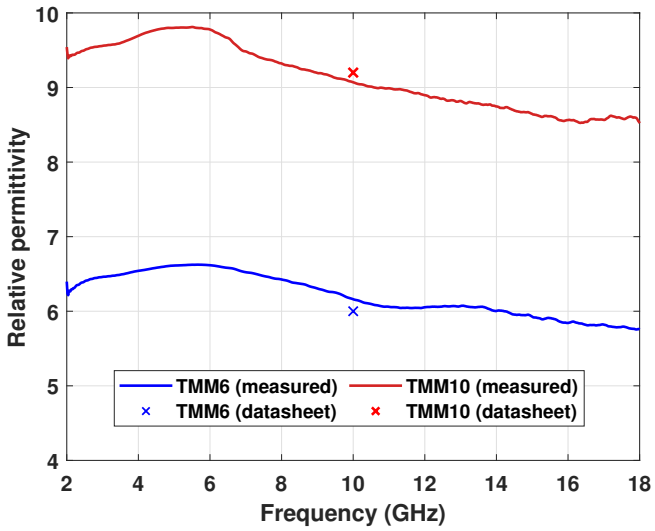

Figure 2.2: Measured permittivity of Rogers TMM boards compared to the datasheet provided permittivity at 10 GHz

The initial measurements are conducted with a material with well-defined properties to ensure the probe functions as expected. The Rogers TMM series boards have a wide selection of permittivity options and high thickness availability. This ceramic material complies with the probe's sample thickness requirements after removing the copper and stacking two half-inch thick boards together. Two substrate types are measured: TMM6 and TMM10, and the results are compared to the expected permittivity at 10 GHz provided on the datasheet, as shown in Fig. 2.2. It is important to note that this board datasheet provides only an average value for all boards manufactured, not for the specific board shipped to the user. At 10 GHz, the measured value is within the manufacturing and measurement tolerances for both samples, providing confidence in the probe's functionality. As expected, the substrates' permittivities vary only slightly across frequency. Note that the N1501A probe is ideal for semi-solid or liquid materials, as even a slight difference in sur-

face flatness with a solid material can cause an air gap and increase measurement error. This probe's measurement of ceramic boards is effective, but maintaining proper contact between the sample and the probe is challenging.

The probe is then used to measure several liquids readily available within a laboratory or a household. These results are later used to select candidates for radar measurements. The materials in this study are deionized water, household white vinegar (4% acetic acid), 50% ethanol, 70% isopropanol (rubbing alcohol), 100% isopropanol, and canola oil. To better see the measured permittivity in Fig. 2.3, the materials are broken into two groups: higher and lower permittivity.

Though water is commonly estimated to have a constant permittivity for low-frequency applications, the permittivity drops by more than 25% from 2 to 14 GHz, as shown in Fig. 2.3a. This result is similar to water measurements presented across literature [27, 28, 29]. It should be noted that deionized water is specifically used due to its predictable electrical composition, and any water with additional impurities may have differing performance. Household distilled white vinegar is only 4% acetic acid, meaning that the mixture is 96% water. Therefore, the vinegar permittivity measurement closely following the curve of the water permittivity is expected. For the three alcohol mixtures, the permittivity drops as the amount of alcohol increases, corresponding to a decrease in water content. The permittivity of canola oil is even lower than the 100% isopropanol, shown in Fig. 2.3b, and varies the least over frequency, which aligns well with the study of cooking oils in the literature [30]. Finally, the measured permittivity of air is approximately equal to free-space permittivity, as expected.

The loss tangent is the other property to consider for radar performance. A

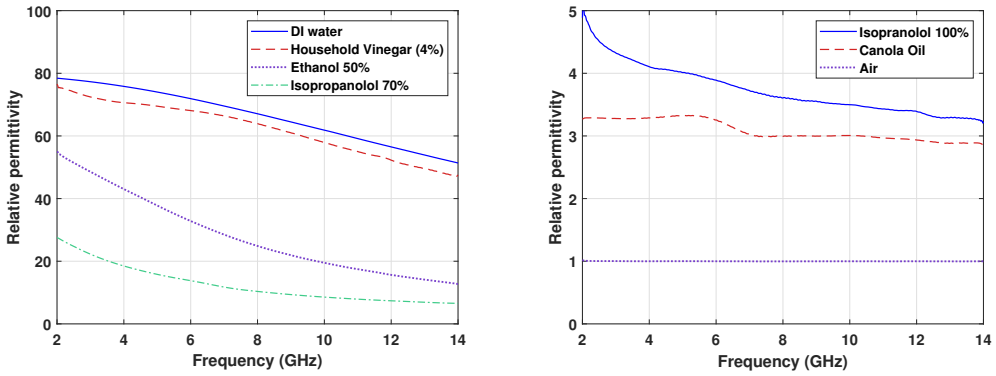

(a) Higher permittivity materials

(b) Lower permittivity materials

Figure 2.3: Relative permittivity of several liquids measured with a Keysight N1501A high temperature dielectric probe

high loss tangent makes water an unpopular choice as a propagation medium in this frequency range. When comparing materials, one may have a lower imaginary permittivity component but still have a higher loss tangent due to a relatively low real permittivity. This relationship occurs with the alcohols in Fig. 2.4. Even though the imaginary component of their permittivity is lower than DI water, the relatively low real permittivities drive them to have a higher loss tangent. Canola oil has a particularly low loss tangent, which is seen across several other varieties of cooking oils as well [31].

2.3 Propagation Through Layers

With an understanding of each propagation medium's electrical properties, the magnitude and phase of the wave's propagation through the medium can be analytically predicted. Boundary conditions describe how much of a wave travels from one medium to another. Understanding boundary conditions is important from a

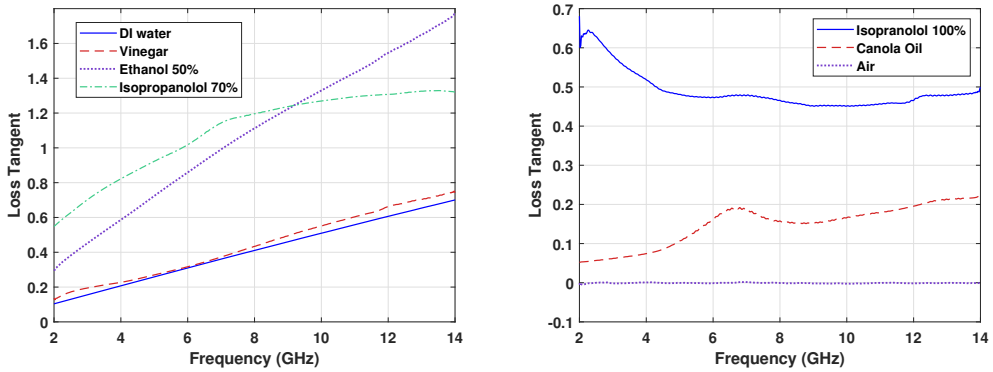

(a) Higher permittivity materials

(b) Lower permittivity materials

Figure 2.4: Loss tangent of several liquids measured with a Keysight N1501A high temperature dielectric probe

radar perspective to accurately predict the received power. For biomedical applications, understanding the power levels through each layer is also important for human safety compliance.

Suppose there is an electromagnetic wave traveling through layer 0 towards layer 1, as depicted by E_i in Fig. 2.5. The E-field reflected at the boundary between layer 0 and layer 1 (E_r) is related to the incident E-field (E_i) by the reflection coefficient ($\Gamma_{0,1}$). When the layers are approximated as infinitely thick, the reflection

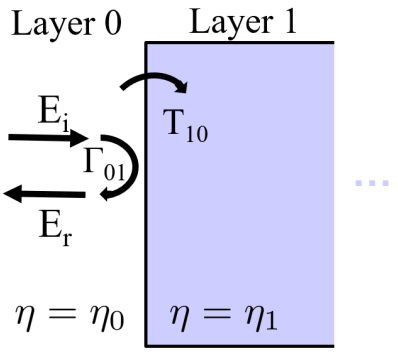

Figure 2.5: Reflection and transmission coefficients for two infinite media

coefficient is defined as

$$\Gamma_{0,1} = \frac{E_r}{E_i} = \frac{\eta_1 - \eta_0}{\eta_1 + \eta_0} \ . \tag{2.14}$$

In this case, the reflection coefficient is only a function of the wave impedance of the two media. The transmission coefficient that describes the fields transmitted from layer 0 into layer 1 is related to the reflection coefficient by

$$T_{10} = \frac{2\eta_1}{\eta_1 + \eta_0} = 1 + \Gamma_{01} \ . \tag{2.15}$$

The transmissivity of a boundary describes how much power is transmitted through the boundary, given by

$$Transmissivity = 1 - |\Gamma|^2 \ . \tag{2.16}$$

Transmissivity is often more directly applicable to radar applications as the link budget calculations and component performance specifications are typically completed in terms of power.

For layers less than a wavelength thick, significant interactions occur among the layers, leading to altered overall boundary conditions [32]. In this case, the E-field reflected from a boundary is the superposition of the initial reflection from (2.14) and the reflections from the boundaries beyond the initial boundary of interest. Considering only a single reflection beyond the initial boundary, the total reflection coefficient for a field incident upon two layers ($\mathbf{\Gamma_2}$) is given by

$$\mathbf{\Gamma_2} = \frac{E_r}{E_i} = \Gamma_{01} + T_{10}\Gamma_{12}T_{01}e^{-2\gamma_1\ell_1} \ . \tag{2.17}$$

The return from the boundary between layers 1 and 2 interferes with the reflection off the initial boundary, constructively if the two reflections are in phase with each other or destructively if the reflections are out-of-phase. The magnitude of the reflected field is lower than the incident field because only a portion of the field is reflected, and the field is attenuated along its path through a lossy medium. Therefore, complete cancellation does not occur in the destructive case.

The two reflections included in (2.17) have the most magnitude, but the wave can be reflected back and forth inside layer 1 any number of times before exiting the stackup. Fig. 2.6 summarizes the possible paths and phase progressions. To include infinitely many reflections in layer 1, the reflected field from (2.17) becomes:

$$\mathbf{\Gamma_2} = T_{10}\Gamma_{12}T_{01}e^{-2\gamma_1\ell_1}\sum_{n=0}^{\infty}\left(\Gamma_{10}\Gamma_{12}e^{-2\gamma_1\ell_1}\right)^n \ . \tag{2.18}$$

With the infinite geometric series format for some expression, r, given by:

$$\sum_{n=0}^{\infty} r^n = \frac{1}{1-r} \ , \tag{2.19}$$

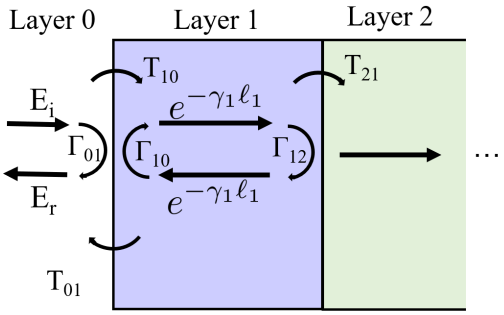

Figure 2.6: Reflection and transmission coefficients and phase progression for a two-layer model

the infinite sum in (2.18) is simplified to be:

$$\mathbf{\Gamma_2} = T_{10}\Gamma_{12}T_{01}\frac{e^{-2\gamma_1\ell_1}}{1-\Gamma_{10}\Gamma_{12}e^{-2\gamma_1\ell_1}} \ . \tag{2.20}$$

For three layers of material, the interaction of reflections within the stackup is more complex. Fig. 2.7 summarizes the possible propagation paths. At each boundary, a portion of the wave is reflected, and the rest is transmitted to the next layer, opening up many combinations of paths that contribute to the total reflection. The total reflection coefficient accounting for only direct reflections is the sum of the field reflected off the boundary between layers 2 and 3 and the two-layer result given by (2.17). To include infinitely many reflections within layer 2 as well as the reflection off the boundary between layers 2 and 3, the appropriate terms are added to (2.20) as

$$\mathbf{\Gamma_3} = \mathbf{\Gamma_2} + T_{10}T_{21}\Gamma_{23}T_{12}T_{01}\frac{e^{-2(\gamma_1\ell_1+\gamma_2\ell_2)}}{1-\Gamma_{21}\Gamma_{23}e^{-2\gamma_2\ell_2}} \ . \tag{2.21}$$

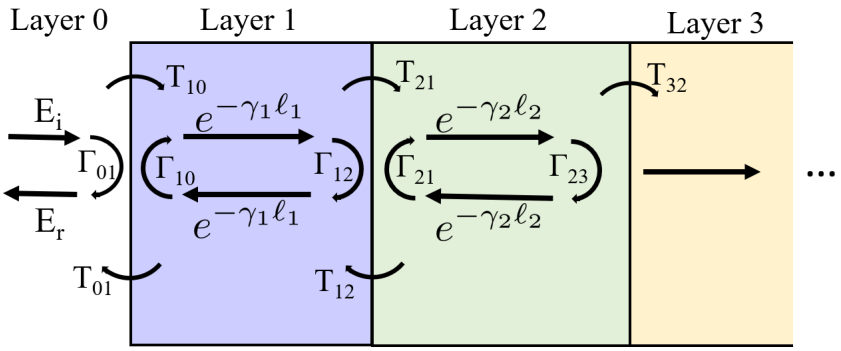

Figure 2.7: Reflection and transmission coefficients and phase progression for a three-layer model

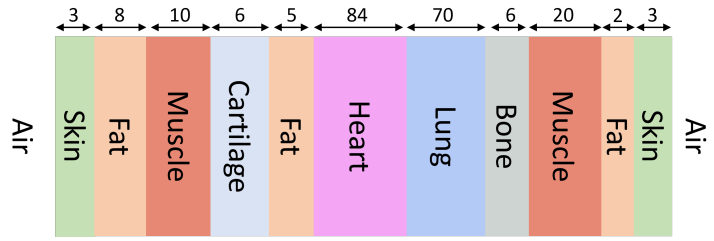

Figure 2.8: Planar representation of Duke thoracic cavity from Virtual Population with layer thicknesses in mm (not to scale) as provided in [33]

2.3.1 Calculations with a Biological Model

To study the impact of including multiple reflections, the calculated total reflection in biological tissue is studied as a relevant geometry. When the body is electrically large, full-wave electromagnetic simulations are computationally intensive. A simplified model can still provide the desired information while reducing computational requirements. Some models simplify the geometry by representing the body as a planar or cylindrical stack-up [33, 34, 35]. Other models, such as the Ansys human body model (HBM), maintain a realistic 3-dimensional shape, but several tissues, including skin, muscle, and fat, are replaced with a single, average material.

For this study, the planar tissue geometry from the planar representation of the thoracic cavity used in [33], developed from the Duke Virtual Population model, is selected, as shown in Fig. 2.8 [37]. The goal is to analyze the impact of including multiple reflections on the calculated total reflection in biological tissue. A wave is normally incident upon the skin layer on the left, where air is layer 0, skin is layer 1, fat is layer 2, etc. The tissue parameters are defined across frequency according to [4]. Only the first two layers of the Duke model, skin and fat, are initially

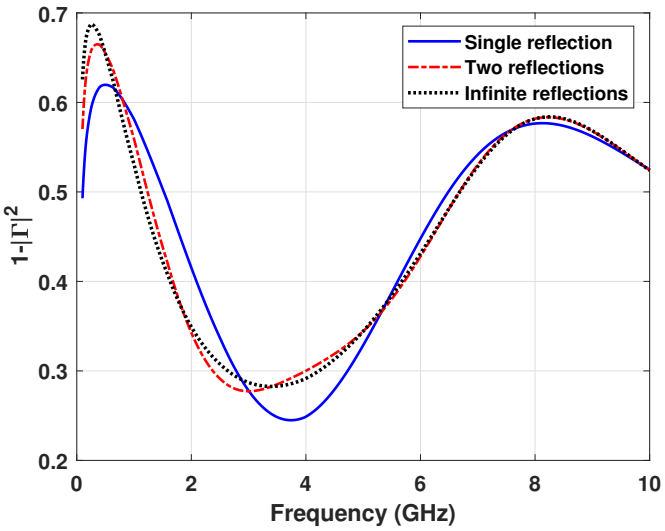

Figure 2.9: Calculated transmissivity through the air-skin boundary calculated using a stackup with skin and fat layers with various numbers of reflections allowed off of the skin-fat boundary [36]

considered. The transmissivity at the air-skin interface is calculated using values of $n = 0, 1$, and ∞ in (2.18) and shown in Fig. 2.9 to compare the impact of including multiple reflections within the skin layer. The destructive interference due to the skin layer being a quarter-wavelength thick results in a minimum transmissivity just below 4 GHz. Adding more reflections shifts the frequency response as more complex interference occurs within the skin layer. As the frequency increases, the skin layer is electrically larger, and fields are attenuated more as they travel through the tissue. As a result, the multiple reflections have less impact on the transmissivity at higher frequencies.

Next, the transmissivity at the air-skin interface is examined with a varying number of layers included in the calculation. As each subsequent layer is added, the calculation consists of the direct path from the air through the stackup to the layer's

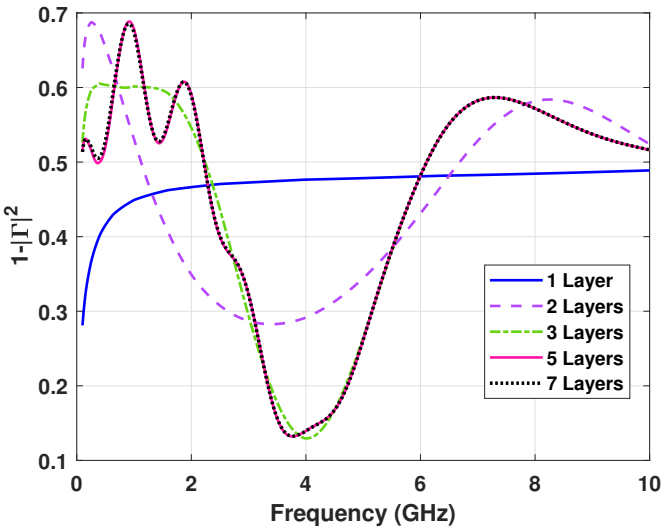

Figure 2.10: Transmissivity through air-skin boundary as a function of the number of tissue layers included in the calculation [36]

back boundary and back through the stackup to the air and infinite reflections within that layer. This calculation protocol shall be referred to as the baseline scenario. Cross terms, including multiple reflections across more than one layer, are omitted in this study. For example, the scenario where the incident wave enters the stackup traveling to the right, reflects off the muscle-cartilage boundary, reflects off the fat-skin boundary, and reflects off the muscle-cartilage boundary again before traveling out of the stackup to the left is not included in this study. The impact of this cross term omission is studied through comparison to a full-wave solver in Section 2.4.

Transmissivities calculated with a varying number of layers are shown in Fig. 2.10. When only the skin layer is included, the calculated transmissivity is equivalent to the case in (2.14), where the two layers are infinitely thick. In this case, the increase in transmissivity over frequency is due to the decrease in the skin's wave impedance over frequency. The calculated transmissivity changes signifi-

cantly across the 1, 2, and 3-layer cases. Adding more than three layers to the calculation yields only subtle differences in transmissivity compared to the 3-layer case, particularly at the high frequencies. This behavior is expected because the magnitude of the reflections from deep within the stackup decreases as frequency increases.

2.4 Comparison to Simulation

The mathematics presented in Section 2.3 are compared to a full-wave simulation in Ansys High Frequency Structure Simulator (HFSS). Ansys HFSS is a finite-element method (FEM) full-wave electromagnetic solver, and the results will contain contributions from all non-trivial cross-terms, which are more terms than what is practical to include in a manual calculation. The Duke thoracic stackup in Fig. 2.8 will be implemented in a Floquet simulation. This type of configuration creates effectively infinitely wide slabs of tissue, so information about the wave propagation along the depth of the body can be isolated. Furthermore, this Floquet port configuration eliminates edge/corner effects from occurring within slabs that would not be present within the 3-D human body geometry. Slabs are constructed for each layer with side lengths of 40 mm and thicknesses corresponding to the respective tissue thickness from Fig. 2.8. Primary and secondary boundaries are assigned across from one another on the sides. A 50 mm air box is included between the front skin layer and the transmitting Floquet port, and a perfectly matched layer (PML) is placed directly on the back face of the tissue stackup, as shown in Fig. 2.11. The tissue parameters are defined in the same manner as in Section 2.3.1.

To compare the calculations from Section 2.3.1 to the simulation, the local spe-

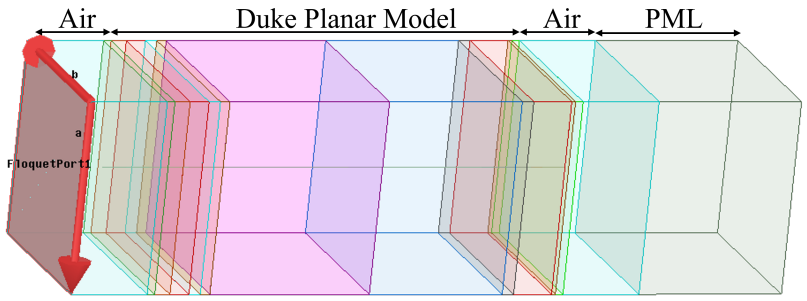

Figure 2.11: Floquet port configuration for planar Duke thoracic cavity simulation

cific absorption rate (SAR) at the skin surface is studied. SAR is a measure of how much power is absorbed by the body. This quantity is useful for the current study of wave propagation because it indicates how much power is entering the skin layer, and SAR will be explored more in Section 3.2. SAR is extracted from $\mathbf{\Gamma}$ with (3.2) as follows:

$$SAR = \frac{-\alpha_1 |1 + \mathbf{\Gamma}|^2 |E_i|^2}{\rho_1 \eta_1} \tag{2.22}$$

where α_1, η_1, and ρ_1 are the first layer's attenuation constant, wave impedance, and mass density, respectively. The SAR value calculated without cross terms is compared to the simulated local SAR at the skin layer's surface for models with a varying number of layers, shown in Fig. 2.12. The calculated values closely align with the simulation for the 1- and 2-layer cases. A larger difference between simulation and calculation for the 3-layer case indicates that the full-wave simulation includes propagation behavior not captured in (2.21).

The 3-layer model is studied further to determine if including a scattering cross term in the calculation improves the agreement between calculated and simulated results. In this model, the most significant expected cross term is a wave traveling into the stackup, reflecting off the fat-muscle boundary, the skin-air boundary,

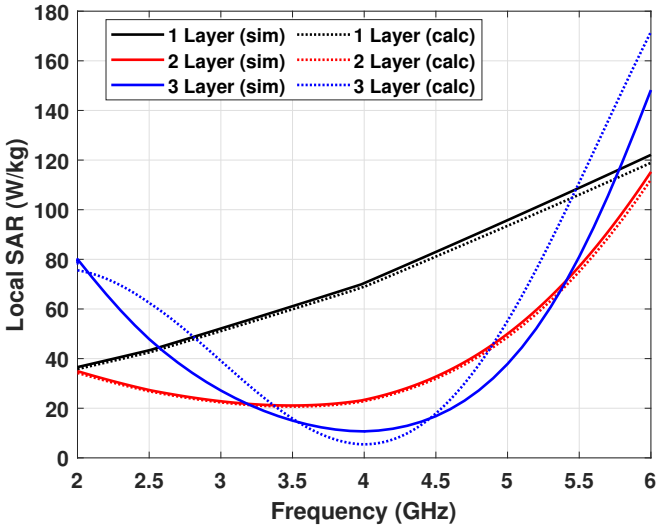

Figure 2.12: Calculated and simulated local SAR at the skin surface with 1, 2, and 3 layers in the model [36]

and the skin-fat boundary, and then exiting the stackup. In this case, the primary reflection at the back of the fat layer is reflected within another layer (skin) before returning to the surface. In Fig. 2.13, the simulated local SAR is compared to calculations that do and do not include this cross term in addition to the baseline scenario. The calculation with the cross term is better aligned with the simulation results. While these results are close, infinitely many more cross terms could be added to refine the calculation. As more layers are added to the model, the possible cross terms become even more complex. For consistency, only the cross term mentioned above is included in the remainder of this work's analysis.

Because the heart and lung layers are so electrically large and the returns from beyond these layers are orders of magnitude smaller than the primary air-skin reflection, a seven-layer stackup, consisting of the initial skin layer through the lung layer, is examined to approximate the entire thoracic cavity. The SAR calculated

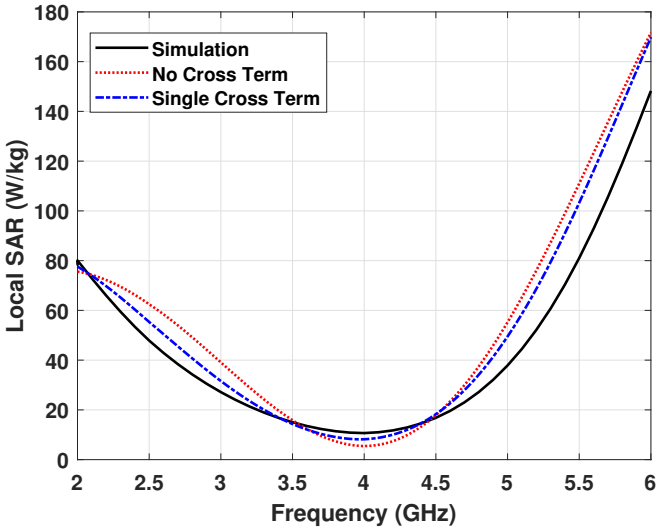

Figure 2.13: Local SAR at the skin surface of the 3-layer model calculated with and without including a cross-layer scattering term compared to simulation

with a single cross term of a return ringing within the skin layer before exiting the body is compared to the simulated local SAR in Fig. 2.14. As expected, the calculated values are closer to simulation at higher frequencies where the layers are electrically larger and more complex propagation paths are more lossy.

In the "1 layer" case, only the skin is included, so $\Gamma_{air,skin}$ is calculated with (2.14). Including the fat layer in the calculation significantly changes the calculated transmissivity, as shown with the "2 layer" case. Adding another layer further alters the response, though the "2 layer" and "3 layer" cases converge above above 7 GHz as the electrical size of the layers increases. Farther into the torso, reflections are significantly attenuated before returning to the air-skin boundary, and the heart and lung layers are electrically large. Thus, modeling layers beyond the heart does not have a visible impact on the air-skin transmissivity.

Because the heart and lung layers are so electrically large and the returns from

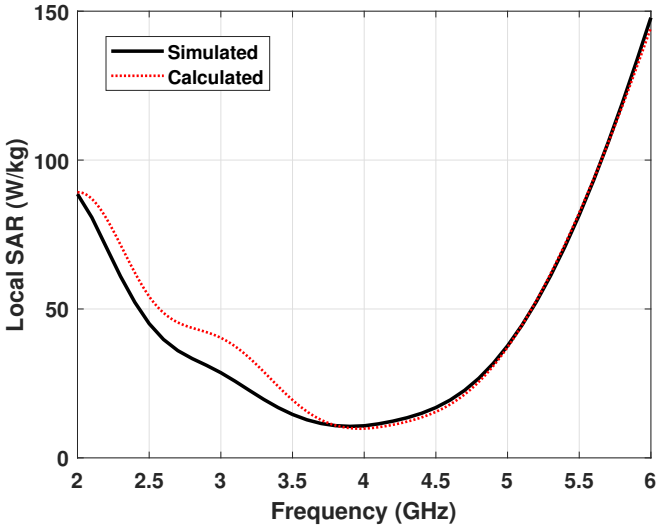

Figure 2.14: Calculated and simulated local SAR at the skin surface with seven layers in the model

beyond these layers are orders of magnitude smaller than the primary air-skin reflection, a seven-layer stackup, consisting of the initial skin layer through the lung layer, is examined to approximate the entire thoracic cavity. The SAR calculated with a single cross term of a return ringing within the skin layer before exiting the body is compared to the simulated local SAR in Fig. 2.14. As expected, the calculated values are closer to simulation at higher frequencies where the layers are electrically larger and more complex propagation paths are more lossy. The overall shape is similar to the SAR shown in [38], though exploring the contributing phenomena was not the focus of that work.

The tradeoff space between accuracy and complexity for modeling the specific absorption rate at the surface of a planar thoracic cavity representation has been studied. Reflections from boundaries within the stackup interact with the field at the surface, and a single-layer model is not an appropriate simplification of a

multi-layer stackup when the layer thicknesses are not electrically large. Multiple reflections, or ringing, occur within each layer and across multiple layers. While the field magnitude decreases with each reflection, modeling multiple reflections within a layer still impacts the reflection coefficient, particularly at lower frequencies. As more layers are added to the model, more possible cross terms can be added to capture the various combinations of increasingly complex propagation paths. Multi-path interference explains why explicitly modeling tissue or dielectric layers is often necessary for simulation. Even though the results have been focused on the thoracic cavity, the principles are applicable to any region of the body, as electrically small layers are present throughout.

Chapter 3

Biological Considerations

The study of how each individual frequency behaves while traveling through multiple media in Chapter 2 is helpful, but more context is necessary to make decisions within the radar design tradeoff space for a biomedical imaging radar (BIR). Typical radar design must consider the system itself and any restrictions on the spectrum in its propagation path. The target properties are also studied to learn what reflection to expect back at the radar. While these factors are also important for a BIR design, human safety must also be considered. BIR is a relatively new imaging modality, but other imaging techniques have been balancing signal quality with patient safety for decades. Practices like studying as much phenomenology as possible on a stand-in phantom before human testing help advance the technology more quickly. This chapter serves as a tutorial on human considerations for a radar engineer who is used to working with inanimate objects.

3.1 Medical Imaging

Medical imaging collects information from within the body without destructively cutting through the tissue to the area of interest. Imaging performance oper-

ates within a tradeoff between image quality and cost, both in the literal financial sense and in the abstract sense of time, portability, and patient safety. Some important image quality metrics are resolution, signal-to-noise ratio (SNR), and clutter-to-noise ratio (CNR). The best imaging modality selection depends on the region of interest, urgency, budget, and patient risk factors.

3.1.1 Traditional Techniques

Computed Tomography (CT) scans are the "gold standard" in the medical community and use the differential attenuation of X-rays (ionizing radiation) passing through the body to diagnose soft tissue. CT scans are fast and score high in the resolution and SNR image quality categories, and several contrast agents can be added to enhance the image [39]. However, a study found a 24% increase in cancer incidence among people who received a CT scan as a child compared to those who did not [40]. Thus, non-ionizing imaging technologies are crucial for repetitive diagnosis situations.

Common non-ionizing options include ultrasound and magnetic resonance imaging (MRI). Ultrasound transmits an acoustic wave and detects the reflections from boundaries between different acoustic impedance values. Acoustic waves fail to penetrate some materials like bone and air cavities, so ultrasound is not a viable option for many regions, including the brain and lungs. MRI creates an image based on the nucleus's longitudinal and transverse relaxation times and proton density, all of which vary across tissues, depending on their respective water content. MRI produces high image quality for soft tissue throughout the body, but the process is slow and expensive. Some patients must be sedated if unable to lay still for over an

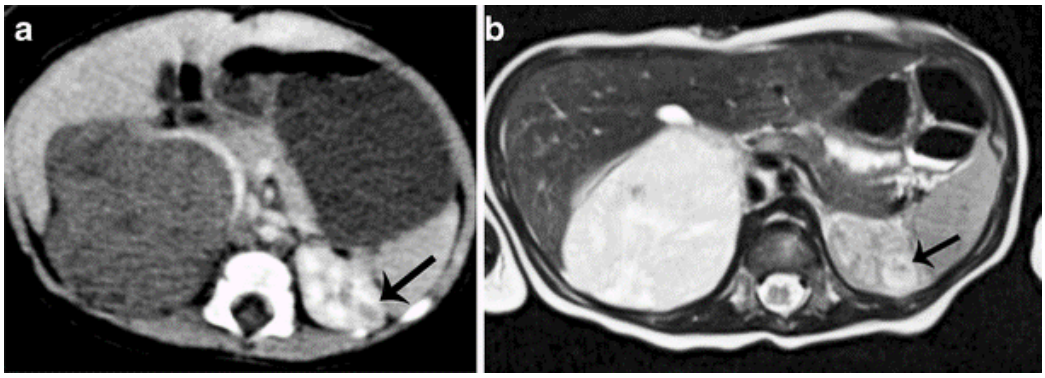

Figure 3.1: Axial CT (a) and T2-weighted MRI (b) images from [41] of a 6-month-old girl with a kidney lesion (arrow)

hour. Contrast agents have been developed for both ultrasound and MRI to enhance image quality [42, 43]. Example images produced by CT and MRI are compared in Fig. 3.1. As expected, MRI yields better contrast within soft tissue, enabling a clear visualization of a kidney lesion.

3.1.2 Microwave Imaging

To overcome the limitations of ultrasound and MRI while avoiding the ionizing radiation used in X-ray and CT, researchers have been investigating the possibility of microwave imaging, which detects the scattering from discontinuities in electrical properties. For example, a malignant breast tumor has a higher permittivity and conductivity than healthy tissue and will scatter a portion of incident electromagnetic waves [45]. Because of this high material contrast and the frequent screening for breast tumors, a great deal of the recent microwave imaging research has been focused on breast cancer detection [46, 47]. Most of the current literature utilizes either radar or tomography to produce an image. Tomography involves a complex inverse scattering problem to extract the dielectric properties while radar collects

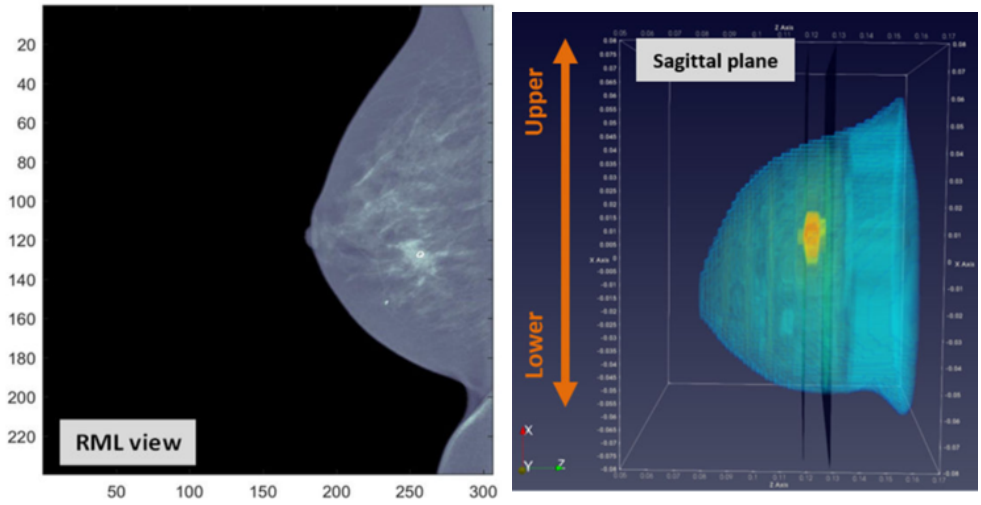

(a) X-Ray

(b) Microwave

Figure 3.2: Clinically measured images from [44] of a patient's right breast with a palpable Invasive Ductal Carcinoma, viewed from the side

backscattered energy, which struggles in low contrast scenarios [10]. The current most common radar modes are step frequency continuous wave (SFCW) or ultra-wideband (UWB) pulse, such as a Gaussian pulse [48, 49, 50]. Both tomography and radar can succeed with commercial off-the-shelf (COTS) or inexpensive hardware, but neither of these modalities is particularly fast or power-efficient.

To achieve sufficient dynamic range, many microwave imaging systems often place the antennas in a matching medium, reducing unwanted skin reflection while increasing the reflections received from the desired inner layer [51]. This solution is feasible for many regions, e.g., the breast or liver. However, for imaging regions within the head, such as the sinus cavity, the patient's head would need to be submerged in the matching liquid, which is impractical. Similar to traditional modalities, some experimental microwave imaging systems employ contrast agents to detect tumors better [52, 53, 54]. The prototype BIR system from [55] is com-

pared to a traditional X-Ray mammogram in Fig. 3.2. While the resolution and sensitivity are better in the X-Ray image, the tumor is still visible in the microwave image.

Current BIR capabilities are primarily limited by insufficient dynamic range and measurement resolution. Radar hardware, both components and system architectures, has improved in recent years for even better dynamic range and bandwidth. Furthermore, developments in radar signal processing help unmask small scatterers that may be hidden in initial results [56]. Current radar prototypes often rely on commercial off-the-shelf (COTS) architectures, which allows for fast results but limits the ability to take advantage of the enhancements developed by radar engineers.

3.1.3 Phantoms

Biomedical technology development relies on phantoms, or stand-ins, for humans during the research and development phase, similar to mannequins in car safety crash tests or animal trials of new pharmaceuticals. This practice avoids human exposure to a product of unknown safety and lowers the cost of the trials. Replicating all tissue properties with a single material is impractical, so the relevant behavior requirements must be prioritized.

Representing the body can be especially challenging because phenomenology occurs all the way down to the ionic level up to the entire length of the body, and capturing the relevant behavior requires an understanding of the underlying cause. For microwave imaging, the electrical permittivity and conductivity are the most important in modeling the electromagnetic wave propagation through each tissue

layer. For human safety studies, the thermal behavior of the phantom is also considered. It is challenging to satisfy the electrical performance over the entire frequency range of interest and also replicate the tissues' mechanical behavior.

Microwave imaging phantoms range in cost, durability, and safety, as some materials are hazardous to use [57, 58]. The phantoms have been developed and refined for many areas of the body, including the knee, chest, skin, and breast [59, 60, 61, 62]. The manufacturing process can range from fume hoods and vacuum chambers with long cure times to more simple 3D-printed structures [60, 62]. Some phantoms can maintain the same properties for many months while others degrade in a matter of hours or days. The most widely utilized database of tissue electric properties is given in [4]. However, tissue properties, notably tumors and abnormalities, are still an area of active research [63, 64]. Data collection is challenging due to the changes in tissue properties after death or after the material is extracted from the body. Furthermore, An individual's dielectric properties may vary over time, and there is some variation across the population. This feature can be exploited for applications such as dehydration detection or ablation monitoring [65, 66]. Another consequence of the dielectric property variance is that no single phantom will perfectly represent all people. As a result, phantom stability may be favored over incrementally increased accuracy in some applications [67].

3.2 Human Safety Regulations

The power attenuated within the body due to tissue conductivity is dissipated as heat, which can harm biological tissue [5, 6, 68]. In the microwave frequency range, the International Commission on Non-Ionizing Radiation Protection (ICNIRP) de-

fines restrictions in terms of specific absorption (SA) and absorbed energy density (U_{ab}) to ensure that the body is not heated above an unsafe level.

The ICNIRP defines SA as the incremental energy (dW) absorbed in an incremental mass (dm) with units of J/kg, which can be re-written with the tissue mass density, ρ (kg/m^3), and differential volume, dV, as

$$\text{SA} = \frac{dW}{dm} = \frac{dW}{\rho dV} \, . \tag{3.1}$$

The SA is averaged over a 10 g cube of tissue, and the maximum allowable SA depends on the region, duration, and frequency of the exposure [7]. Simulations typically model the incident wave at a steady state and yield SAR values, and then the SAR is integrated over time to calculate the corresponding SA values. The peak spatial average SAR (psSAR) value is of most interest because psSAR represents the area of highest radiation absorption.

SAR was already introduced in Section 2.4 as an indicator of how much power flows into the body, and the value was given as a function of the air-skin reflection coefficient. As shown in [69], the power dissipated in the body, and the corresponding SAR can also be written directly as a function of the electric field within the tissue. The SAR at location z is given by

$$\text{SAR}(z) = \frac{-\alpha |E|^2}{\rho \eta} \tag{3.2}$$

where α is the tissue's frequency-dependent attenuation constant, E is the electric field, ρ is the tissue mass density, and η is the tissue's wave impedance [69].

The ICNIRP publication provides basic restrictions (BR) regarding average

SAR for frequencies below 6 GHz for exposures longer than six minutes [7]. Above 6 GHz, the power is dissipated more quickly and does not penetrate as far into the body, so the restriction is in terms of the absorbed power density at the body's surface. The 2020 ICNIRP publication defines time-dependent BR for local exposures shorter than six minutes to prevent tissue from heating too quickly [7]. From 100 kHz to 6 GHz, the ICNIRP BR for head or trunk exposures lasting less than six minutes is defined in terms of SA as

$$\text{SA} \leq 3.6(0.05 + 0.95\sqrt{t/360}), \text{ for } t < 360 \text{ s} \tag{3.3}$$

where t is the exposure duration in seconds, and the SA (kJ/kg) is averaged over a 10 g cube of tissue. From 6 GHz to 300 GHz, the BR is given in terms of the epithelial energy density. The BR is defined by U_{ab} averaged over a 4 cm^2 square as follows:

$$\text{U}_{ab} \leq 36(0.05 + 0.95\sqrt{t/360}), \text{ for } t < 360 \text{ s} . \tag{3.4}$$

The expression inside parentheses in (3.3) and (3.4) ranges from 0.05 to 1 when $t = 0$ and $t = 360$ seconds, respectively. When t is small relative to 360, the constant 0.05 dominates the expression. Thus, the basic restrictions are almost constant for exposure durations lasting only a fraction of a second. For example, the SA limit changes from 180.2 to 181.8 J/kg when the exposure duration changes from 1 μs to 100 μs. On the other hand, increasing the exposure duration from 1 s to 100 s corresponds to a 5.5 times higher allowable SA value. When multiple

frequencies are involved, ICNIRP provides the additional restriction of

$$\sum_{i=100\ kHz}^{6\ GHz} \frac{\mathrm{SA}_i}{\mathrm{SA}_{BR}} + \sum_{i=6\ GHz}^{300\ GHz} \frac{\mathrm{U}_{ab,i}}{\mathrm{U}_{ab,BR}} \leq 1 \tag{3.5}$$

where SA_i is the SA at each frequency, $\mathrm{U}_{ab,i}$ is the absorbed energy density at each frequency, SA_{BR} and $\mathrm{U}_{ab,BR}$ are the SA and U_{ab} values of the basic restrictions, respectively [7].

These restrictions frame further tradeoffs in BIR design. Because the exposure criteria must be satisfied for all values of time from 0 to 6 minutes, individual pulses, as well as the pulse train as a whole, must be considered. For example, for several pulses of a given radar waveform, halving the duty cycle but doubling the transmit power yields the same specific absorption and absorbed power density, but the exposure of a single pulse must also satisfy regulations [70].

Only biomedical radar applications must consider the safety restrictions of intentionally radiating a human, and it is important to understand how this affects the radar design tradeoff space. When forming a radar image, some of the system parameters that affect the image quality are dynamic range, range resolution, cross-range resolution, and SNR. The dynamic range is the difference between the largest and smallest power that the radar can handle. The radar must have a dynamic range large enough to avoid saturation from antenna coupling and close-range scatterers while still being sensitive enough to detect the signal of interest. Even if the desired signal is above the thermal noise floor, the information cannot be extracted without sufficient dynamic range, and increasing the transmit power does not help overcome dynamic range deficiencies. Instead, the system is re-designed to han-

dle a higher dynamic range, or the environment is altered to reduce dynamic range requirements.

The SNR depends on the location and physical properties of the target of interest. For example, extracting information from the skin return with mm-wave frequencies would be possible, but this work's frequency range is typically used to extract information beyond the skin return. To maintain general applicability, the absolute SNR will not be analyzed. Instead, the SNR parameters that depend on the waveform and power transmitted will be focused on to study relative SNR. For pulse compression waveforms, the SNR increases by the product of the time spent illuminating the target and the bandwidth of operation [1]. Coherently integrating N pulses decreases thermal noise because the signal of interest is present in every pulse, while zero-mean thermal noise that is distributed as a zero-mean Gaussian function is uncorrelated between pulses and will decrease according to the central limit theorem. Therefore, the SNR will increase by a factor of N.

A plane-wave incidence is simulated in Ansys High-Frequency Structure Simulator (HFSS) to obtain constant look exposure values from 2-18 GHz. The power absorbed will vary with the exposed region and the body's proportions. Therefore, no single simulation can represent all biomedical radar use cases, and the simulation geometry must be selected to represent the specific exposure scenario of interest. Because this initial analysis is not focusing on any specific application, the thoracic cavity is selected to provide results for one feasible application. Duke is a member of the Virtual Family, a set of human models for electromagnetic exposure studies [37]. The same planar representation of Duke's thoracic cavity shown in Fig. 2.8 is arranged in the same simulation configuration as Fig. 2.11.

The incident plane wave is vertically polarized and normally incident upon the surface of the skin layer. The electromagnetic field behavior at the edge of a human body will be different from this planar representation because in a real body, the skin wraps all the way around the outside, and some internal organs do not extend across the full width of the torso. Therefore, the planar model is most representative of the human body at the center. The width of the tissue slabs is selected to be 250 mm to ensure no edge effects impact the center where the exposures are calculated. The peak spatial average SAR (psSAR) is extracted from 2-6 GHz using the average SAR calculated with the HFSS built-in implementation of IEEE/IEC Std 62704 [71]. The absorbed power density from 6-18 GHz is extracted by integrating the Poynting vector through the surface of a 4 cm^2 square placed on the skin's surface in the center of the slab.

The SNR factor for two waveforms is analyzed: linear frequency modulation (LFM) and the second-derivative Gaussian pulse. The LFM waveform is considered for pulse widths of 240 μs and 1 ms and bandwidths of 2-6, 2-12, 2-18, and 6-18 GHz. Second-derivative Gaussian pulses with widths of 83.1 ps and 42 ps are considered, which correspond to center frequencies of 2.5 GHz and 7.5 GHz, and 10-dB bandwidths of 5 GHz and 10 GHz, respectively. The SNR factor describes waveform-specific pulse compression gain, coherent integration gain, and received power. The SNR factor (kW/m^2) is defined as $S_{inc}NBT$ where S_{inc} is the incident power density (kW/m^2), N is the number of pulses, B is the bandwidth, and T is the pulse duration. The received power is proportional to the power incident upon the body, as described in the radar range equation [1].

3.2.1 FMCW

One of the most common radar imaging modalities is FMCW. With stretch processing, FMCW receivers can utilize a low sample rate on the order of 10 kHz for short-range applications. An FMCW radar transmits an LFM waveform, which is given by

$$x(t) = \text{rect}\left((t-T)/T\right)\cos(2\pi F_0 t + \pi\gamma t^2)\ , \tag{3.6}$$

where F_0 is the initial frequency, and γ is the chirp rate, defined as B/T. The instantaneous frequency of the LFM at time t is

$$f(t) = F_0 + \gamma t\ . \tag{3.7}$$

The total SA for frequencies below 6 GHz is computed as the time-integral of psSAR. Though SAR is a function of frequency, (5.3) is used to relate the instantaneous frequency to time. Similarly, the total U_{ab} above 6 GHz is the time-integral of S_{ab}. The full restriction from (3.5) then becomes

$$\frac{1}{SA_{\text{BR}}}\int_{T_6} psSAR(t)\ dt + \frac{1}{U_{\text{ab,BR}}}\int_{T_{6+}} S_{\text{ab}}(t)\ dt \leq 1\ . \tag{3.8}$$

where $T_6 = \{t : f(t) \leq 6\text{ GHz}\}$, $T_{6+} = \{t : f(t) > 6\text{ GHz}\}$, and $T_6, T_{6+} \subset [0, T]$.

Because the basic restrictions must be satisfied for all values of t, then (3.8) must be satisfied for T and all possible segments of T. Even with an assumption that the incident power density is constant across frequency, the frequency-dependent electrical properties of the body yield a frequency-dependent absorption of the incident electromagnetic wave. The tissue geometry also plays a role in the

absorption across frequency. Therefore, even though the basic restriction evaluated at time T (BR_T) is satisfied, the exposure accumulated in a segment of T, defined as $T_{\text{seg}} = \{t : t_1 \leq t \leq t_2\}$ for $t_1 \geq 0$ and $t_2 \leq T$, may not satisfy $\text{BR}_{T_{\text{seg}}}$.

If the SA and U_{ab} basic restrictions are satisfied for $t = T$, the following inequalities must be satisfied to also comply with the basic restrictions for any duration shorter than T:

$$\frac{\int_{T_{\text{seg}}} psSAR(t)\ dt}{\int_{T_6} psSAR(t)\ dt} \leq \frac{SA_{\text{BR},T_{\text{seg}}}}{SA_{\text{BR},T_6}},\ \text{for } f < 6\ \text{GHz} \tag{3.9}$$

if the segment is at or below 6 GHz and

$$\frac{\int_{T_{\text{seg}}} S_{\text{ab}}(t)\ dt}{\int_{T_{6+}} S_{\text{ab}}(t)\ dt} \leq \frac{U_{\text{BR},T_{\text{seg}}}}{U_{\text{BR},T_{6+}}},\ \text{for } f \geq 6\ \text{GHz} \tag{3.10}$$

if the segment is above 6 GHz. If the LFM sweep in T_{seg} contains frequencies in both regulatory bins, the segment is split and evaluated as two segments: $T_{seg,6}$ and $T_{seg,6+}$. By definition, the integral of each quantity over time is equal to the time-average value multiplied by the respective time duration. Therefore, the inequalities become

$$\frac{\overline{psSAR}_{T_{\text{seg}}} T_{\text{seg}}}{\overline{psSAR}_T T} \leq \frac{SA_{\text{BR},T_{\text{seg}}}}{SA_{\text{BR},T}},\ \text{for } f < 6\ \text{GHz} \tag{3.11}$$

and

$$\frac{\overline{S}_{\text{ab},T_{\text{seg}}} T_{\text{seg}}}{\overline{S}_{\text{ab},T} T} \leq \frac{U_{\text{BR},T_{\text{seg}}}}{U_{\text{BR},T}},\ \text{for } f \geq 6\ \text{GHz} \tag{3.12}$$

where $\bar{(\cdot)}$ denotes a time average.

To ensure that the basic restrictions are satisfied for T_{seg} if they are satisfied for T, a maximum value is defined for the disparity between the average of any given

time segment compared to the remainder of the sweep. The exposure disparity within T is defined as $\overline{\text{Exposure}}_{\text{seg}}/\overline{\text{Exposure}}_{\text{rem}}$ where $\overline{\text{Exposure}}_{\text{seg}}$ and $\overline{\text{Exposure}}_{\text{rem}}$ are the average exposure values within T_{seg} and within $T - T_{\text{seg}}$, respectively, and exposure refers to either psSAR or S_{ab}. Because the basic restrictions for psSAR and S_{ab} change at the same rate with respect to time, the maximum allowable exposure disparity will be the same for both psSAR and S_{ab}.

While the psSAR depends upon the tissue geometry, the S_{ab} is primarily a function of the air-skin boundary condition. The reflection at a boundary is dictated by each medium's permittivity and conductivity [3]. The electrical properties of biological tissue vary gradually with frequency, and the largest S_{ab} disparity that occurs in the simulated planar Duke model from 6-18 GHz is 1.07 [34]. The behavior of psSAR is more complex. The psSAR is a function of the superposition of all electric fields in the averaging area, as given by (3.2), and the electrical size of the layers plays a role in addition to the conductivity and permittivity. Thus, the psSAR pattern varies more over frequency.

The maximum psSAR disparity of the planar Duke model is calculated with the results from the psSAR simulation. For each segment size, T_{seg}, all possible

System	T_6	Maximum psSAR Disparity		
		$T_{\text{seg}}/T_6 = 0.1$	$T_{\text{seg}}/T_6 = 0.5$	$T_{\text{seg}}/T_6 = 0.99$
[72]	7.5 μs	4804	1250	738
[8]	60 μs	1696	442	261
[73]	1.67 ms	324	85.8	51.2
Simulation		2.36	1.58	1.68

Table 3.1: Maximum allowed exposure disparity calculated for different LFM sweep durations compared to the maximum psSAR disparity occurring in a 2-6 GHz simulation of the planar thoracic Duke model

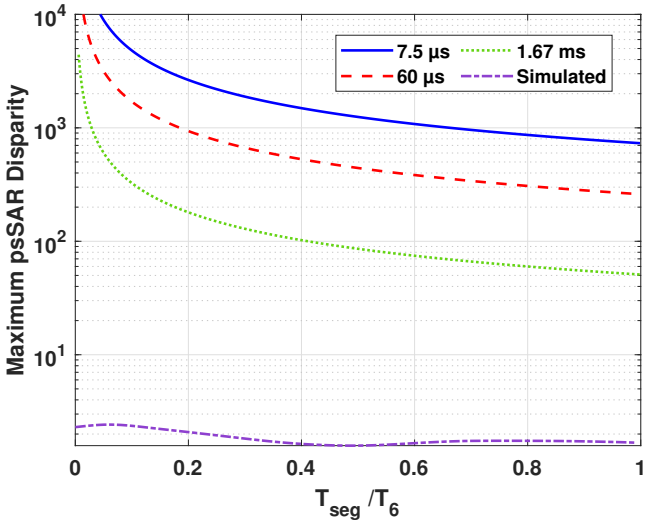

Figure 3.3: Maximum allowed psSAR disparity calculated for several values of T_6 listed in Table 3.1 compared to the disparity in simulated planar Duke model psSAR values

combinations of splitting up the psSAR values into T_{seg} and T_6 are evaluated, and the maximum occurring disparity for that segment size is recorded. The result is plotted as the "Simulated" trace in Fig. 3.3 for all possible ratios of T_{seg}/T_6. The overall highest simulated disparity is 2.42, which occurs at $T_{\text{seg}}/T_6 = 0.06$. For comparison, (3.11) is evaluated to find the maximum allowed disparity for values of T_6 that have been implemented in the FMCW systems provided in Table 3.1, and the results are plotted in Fig. 3.3. Similar results can be shown for T_{6+}. Even though the psSAR has a higher simulated disparity than the S_{ab}, both simulated disparities are orders of magnitude smaller than the calculated allowed values listed in Table 3.1 and Fig. 3.3. Thus, when evaluating exposure on time scales implemented in FMCW radar systems, the frequency-dependent exposure due to biological tissue properties and geometry does not vary enough to violate BR_{Tseg} if BR_T is

satisfied. Therefore, the remaining analysis is conducted for full pulse durations.

Because the LFM frequency change is constant with time, the waveform duration is evenly spread across the swept bandwidth, and averaging the power over time is equivalent to averaging over frequency. Therefore, the integrals in (3.8) can be simplified to the time-average value of the integrand multiplied by the period of the sweep spent in the corresponding frequency bin. This simplification assumes that S_{inc} is constant across frequency, which is true in simulation and achievable in real hardware with the use of variable gain amplifiers. After inserting the expressions for SA_{BR} and $U_{\text{ab,BR}}$ from (3.3) and (3.4), respectively, the inequality becomes

$$\frac{T_6\overline{psSAR}_{T_6}}{3.6\left(0.05+0.95\sqrt{\frac{T_6}{360}}\right)}+\frac{T_{6+}\overline{S}_{\text{ab},T_{6+}}}{36\left(0.05+0.95\sqrt{\frac{T_{6+}}{360}}\right)}\leq 1\ . \tag{3.13}$$

As an example, if the radar sweeps from 2-18 GHz in T seconds, then the length of $|T_6|$ = 0.25T and $|T_{6+}|$ = 0.75T. The HFSS simulations of the planar Duke model provide the values of $\overline{psSAR}_{2-6}$ and $\overline{S}_{\text{ab},6-18}$. Because the same amount of time is spent at each frequency in the LFM, the simulated psSAR values from 2-6 GHz are averaged together with an even weighting to yield the time-average $\overline{psSAR}_{2-6}$ value of $1.67\times10^{-2}S_{inc}$. Similarly, the average of the simulated S_{ab} results from 6-18 GHz produce an $\overline{S}_{\text{ab},6-18}$ value of $0.527S_{\text{inc}}$. The S_{inc} restriction is then

$$S_{\text{inc}}\leq\frac{1}{T}\left(\frac{0.05+0.95\sqrt{\frac{T}{1440}}}{1.16\times10^{-3}}+\frac{0.05+0.95\sqrt{\frac{T}{480}}}{1.1\times10^{-2}}\right). \tag{3.14}$$

The values for $\overline{psSAR}_{T_6}$ and $\overline{S}_{\text{ab},T_{6+}}$ are unique to this particular body model and waveform choice, so the S_{inc} restriction varies for each region of the body.

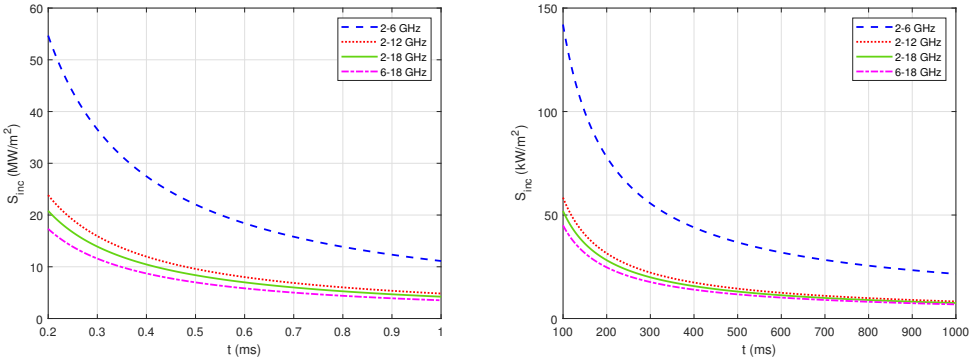

(a) (b)

Figure 3.4: LFM signal duration vs. maximum incident power density with various bandwidths for durations of (a) 0.2 to 1 ms (MW/m^2) and (b) 100 to 1000 ms (kW/m^2)

The maximum incident power density is compared for several frequency ranges in Fig. 3.4 to evaluate the potential benefits of changing the ratio of frequencies above and below 6 GHz. Even though the BR allows higher SA and U_{inc} values for longer exposure times, the absorbed energy linearly increases with time. This linear increase outpaces the increase of the BR, resulting in a decrease of the allowed incident power across time. As a result, approximately 25% more incident power density is allowed when only frequencies below 6 GHz are present. For bandwidths spanning both regulatory frequency bins, the maximum incident power density is similar.

When the time-bandwidth product is accounted for instead of just S_{inc}, the SNR factor over T takes on a different shape across pulse duration, as seen in Fig. 3.5. Because only one pulse is under consideration, N is set to 1. The T contributing to the time-bandwidth product increases more quickly than the S_{inc} decreases, allowing the maximum achievable SNR to increase with time. The maximum SNR

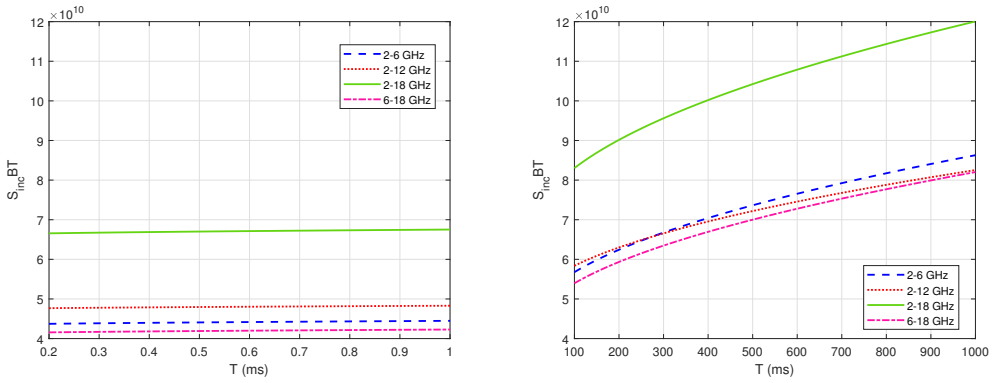

(a) (b)

Figure 3.5: LFM signal duration vs. maximum SNR factor with various bandwidths for durations of (a) 0.2 to 1 ms and (b) 100 to 1000 ms

increases slowly relative to the increase in collection time, so a shorter collection time is favorable if a modest SNR decrease is tolerable. Application-specific analysis would be necessary to determine if the rate of increase in the ideal SNR is worthwhile compared to the increase in test duration, which increases the likelihood of image degradation due to patient movement.

When multiple sweeps are employed, the restrictions must be satisfied for both the individual sweep and the entire sweep sequence. The time-dependent restrictions in (3.3) and (3.4) are not linear, so the restriction for N sweeps is not just the single-sweep restriction multiplied by N. The duty cycle (D) is defined as the percentage of time the radar is transmitting, i.e., the sweep length T divided by the pulse repetition interval (PRI). If the radar is constantly transmitting, PRI = T, and D = 100%. In (3.8), SA_{BR} and $U_{\text{ab,BR}}$ are evaluated at $t = N(PRI)$, and the $psAR_{T_6}$ and $S_{\text{ab},T_{6+}}$ are integrated over time NT.

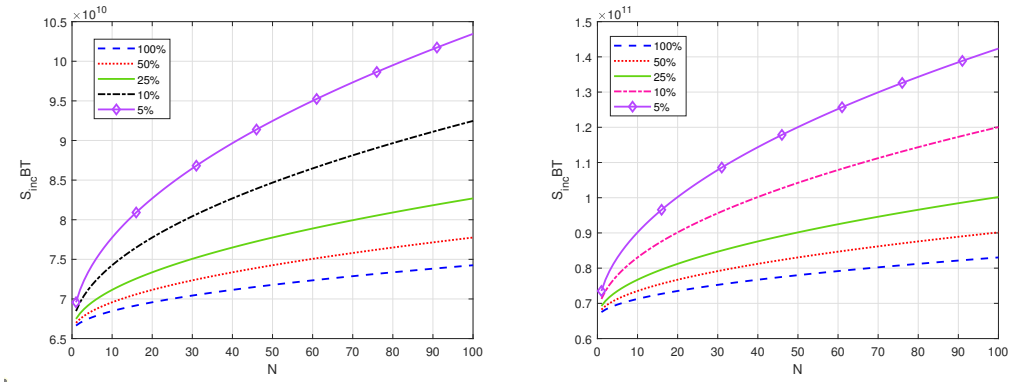

(a) 240 μs (b) 1 ms

Figure 3.6: Number of pulses vs. maximum SNR factor for various duty cycles with a pulse duration of (a) 240 μs and (b) 1 ms for a single 2-18 GHz LFM

For multiple sweeps of an LFM waveform, the restriction becomes

$$\frac{NT_6\overline{psSAR}_{T_6}}{3.6\left(0.05+0.95\sqrt{\frac{N\text{PRI}}{360}}\right)}+\frac{NT_{6+}\overline{S}_{\text{ab},T_{6+}}}{36\left(0.05+0.95\sqrt{\frac{N\text{PRI}}{360}}\right)}\leq 1\ . \tag{3.15}$$

To understand the impact of N and D on power limitations, sweeps from 2-18 GHz with two different durations are considered: 240 μs and 1 ms. Each of these durations could represent the sweep time capabilities of two different systems considered in the design process. The coherent processing interval (CPI) is the total length of all pulses, equal to NT/D. In this case, the pulse is not shortened to decrease D. Instead, the PRI is increased, so there is more time between pulses. Applying (3.15) to the 2-18 GHz LFM leads to a maximum SNR factor of

$$S_{\text{inc}}NBT\leq\left(\frac{0.05+0.95\sqrt{\frac{NT}{1440D}}}{7.25\times10^{-14}}+\frac{0.05+0.95\sqrt{\frac{NT}{480D}}}{6.88\times10^{-13}}\right)\ . \tag{3.16}$$

The relationship between N and the maximum SNR factor for several duty cycles

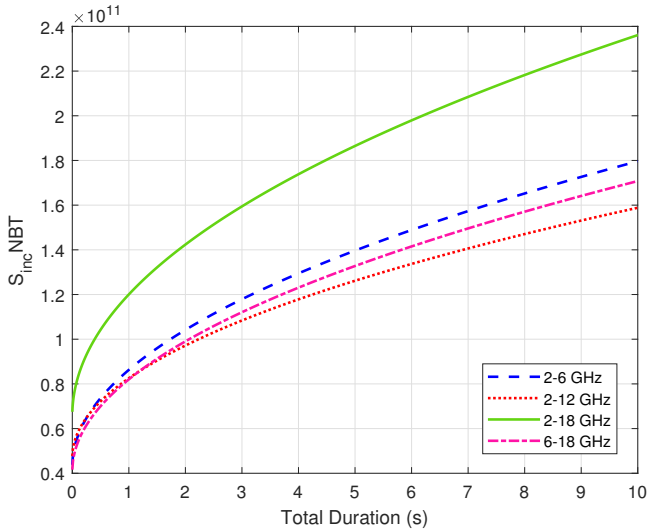

Figure 3.7: Total collection time vs. maximum SNR factor for LFM of various bandwidths repeated N times

is presented in Fig. 3.6. For a particular selection of N and D, a longer pulse length produces a higher SNR factor, as expected from the increased time illuminating the target. For each value of N, smaller values of D yield a higher SNR factor. However, the SNR factor increase in (3.16) is smaller than the increase in test duration. For example, in Fig. 3.6b, reducing the duty cycle from 100% to 5% corresponds to a 20× longer CPI, but the maximum SNR factor for N = 70 only increases by 62%. The duty cycle reduction could be an intentional design choice or a system hardware limitation.

When considering the SNR factor in terms of (3.15), it can be seen that for a given bandwidth, the maximum SNR factor depends only on the CPI. Thus, for a given CPI, varying the N, D, and T combination does not impact the SNR factor. Increasing the total test time will increase the maximum SNR in ideal situations, but the tradeoff is still the longer collection time increasing the risk of smearing

due to patient movement.

For a variable bandwidth, sweeping a larger bandwidth in a given CPI increases the SNR factor, as seen in Fig. 3.7. Though the 2-6 GHz scenario has a smaller bandwidth, the higher S_{inc} allowed below 6 GHz, shown in Fig. 3.4, compensates for the decreased bandwidth in the overall SNR factor. Fig. 3.7 illustrates that the maximum achievable SNR factor depends on the total test duration and is agnostic to the specific system characteristics such as the duty cycle and pulse width. A shorter pulse width allows for more pulses in a given test duration, and a decreased duty cycle increases the allowed total exposure at the expense of longer test duration. Therefore, other design considerations, such as component availability and cost, can dictate the values of N, D, and T that compose the desired CPI.

3.2.2 UWB

A common waveform in current microwave imaging literature is the Gaussian pulse because of its improved angular resolution compared to rectangular pulses [74]. The hardware to *generate* an approximately Gaussian pulse is relatively simple. Rather than relying on high-Q components that operate well at high frequency, the UWB system operation is determined by precise timing capabilities [75, 76]. The most restricted component is the antenna because a resonating structure would prevent proper transmission of the waveform [77]. On the other hand, the hardware to *receive* a Gaussian pulse is more challenging to design. The receiver must either direct sample the received waveform, or the received waveform is passed through several mixing stages. Further, the bandwidth of a receiver is often much less than the transmitted bandwidth of the Gaussian pulse. Therefore, the Gaussian pulse

must either be undersampled or transmitted multiple times and sampled at progressive frequency points. This results in either decreased resolution or an increased time to collect data.

Waveform design is more complex for the Gaussian pulse than the LFM. Unlike rectangular pulses, defined by the pulse width, a Gaussian pulse is described by its full width at half maximum (FWHM) or (χ) because the Gaussian pulse's time extent is ideally infinite. The time-bandwidth product is fixed for a given derivative order because the bandwidth increases proportionally to any decrease in FWHM, as stated by the Fourier uncertainty principle. The pulse width sets the center frequency; however, the waveform spectrum is not symmetrical about the center frequency. Thus, the derivative order for a given application is selected based on the desired center frequency and bandwidth relationship as well as the spectral shape for regulatory spectrum restriction purposes. Like the LFM, the Gaussian range resolution is defined by $v_p\chi$/2 if a Hilbert transform is used for envelope detection, where v_p is the electromagnetic wave velocity of propagation. However, the processing is more complex than the matched filter. For the LFM, the CPI is defined as NT/D, whereas the Gaussian pulse's CPI is commonly described by a pulse repetition frequency (PRF) as N/PRF rather than a duty cycle.

Commonly, a first-derivative Gaussian pulse is generated, and then the transient response of the transmit antenna applies a time derivative, yielding a second derivative Gaussian pulse incident upon the patient [78, 79, 80, 81]. Therefore, the second derivative Gaussian pulse will be the focus of this analysis, though the concepts are similar for other derivative variations. The second-derivative Gaussian

pulse is given by

$$x(t) = \frac{2}{\tau^2} e^{-(t/\tau)^2} \left(\frac{2t^2}{\tau^2} - 1 \right) \tag{3.17}$$

where τ is a time constant that shapes the pulse but is *not* the FWHM. The corresponding frequency spectrum is

$$X(f) = -2\sqrt{2}\tau\pi^2 f^2 e^{-(\pi\tau f)^2} \ . \tag{3.18}$$

The time-bandwidth product of this waveform is fixed to 0.42, which is much smaller than an LFM waveform [82]. Note, the time-bandwidth product of a 2-18 GHz LFM with a duration of 240 μs is 3.8 $\times 10^6$.

Two FWHM values will be considered to conduct the radiation analysis: 83.1 and 42 ps, corresponding to center frequencies of 2.5 and 7.5 GHz and 10-dB bandwidths of 5 GHz and 10 GHz, respectively [82]. To compute the relevant dosimetric quantities in (3.5), the normalized power spectral density (PSD) is multiplied by the simulated psSAR or S_{ab} to appropriately scale the psSAR and S_{ab} by the power present at each frequency. These expressions are then integrated across the frequency groups as follows:

$$\widehat{SAR}_{F_6} = \int_{100\text{ kHz}}^{6\text{ GHz}} |\hat{X}(f)|^2 psSAR(f) df \tag{3.19}$$

and

$$\hat{S}_{\text{ab},F_{6+}} = \int_{6\text{ GHz}}^{300\text{ GHz}} |\hat{X}(f)|^2 S_{\text{ab}}(f) df \tag{3.20}$$

where $\widehat{SAR}_{F_6}$, $\widehat{S}_{F_{6+}}$, and $\hat{X}(f)$ are the equivalent to SAR_{T_6}, $S_{\text{ab},T_{6+}}$, and the frequency representation of the waveform when the average incident power den-

sity ($\bar{S}_{\text{inc}}$) is 1 W/m, respectively, and psSAR(f) and S$_{ab}(f)$ are the frequency-dependent simulated psSAR and S$_{ab}$ for a 1 W/m incident plane wave.

The regulatory limit is then applied as

$$S_{\text{inc}}\, NT \left(\frac{\widehat{SAR}_{F_6}}{SA_{\text{BR}}} + \frac{\hat{S}_{\text{ab},F_{6+}}}{U_{\text{ab,BR}}} \right) \leq 1 \ , \tag{3.21}$$

where T is the FWHM. Inserting the expressions for the basic restrictions, the inequality becomes

$$S_{\text{inc}}\, NT \left(\frac{\frac{\widehat{SAR}_{F_6}}{3.6} + \frac{\hat{S}_{\text{ab},F_{6+}}}{36}}{0.05 + 0.95\sqrt{\frac{N}{360PRF}}} \right) \leq 1 \ . \tag{3.22}$$

This equation simplifies more than (3.14) because the same time duration is used for both regulatory frequency bins.

For the 83.1 ps pulse, the SNR factor limit is

$$S_{\text{inc}} NTB \leq 9.41 \times 10^{11} \left(0.05 + 0.95\sqrt{\frac{N}{360PRF}} \right) \ , \tag{3.23}$$

and for the 42 ps pulse, the maximum SNR factor is

$$S_{\text{inc}} NTB \leq 8.16 \times 10^{11} \left(0.05 + 0.95\sqrt{\frac{N}{360PRF}} \right) \ . \tag{3.24}$$

For the 83.1 ps pulse, 92% of the energy is contained in the 100 kHz to 6 GHz frequency bin and 8% is in the 6 GHz to 300 GHz frequency bin. For the 42 ps pulse, 22% of the energy is contained in the 100 kHz to 6 GHz frequency bin, and 78% of the energy is in the 6 GHz to 300 GHz frequency bin. The difference in the total

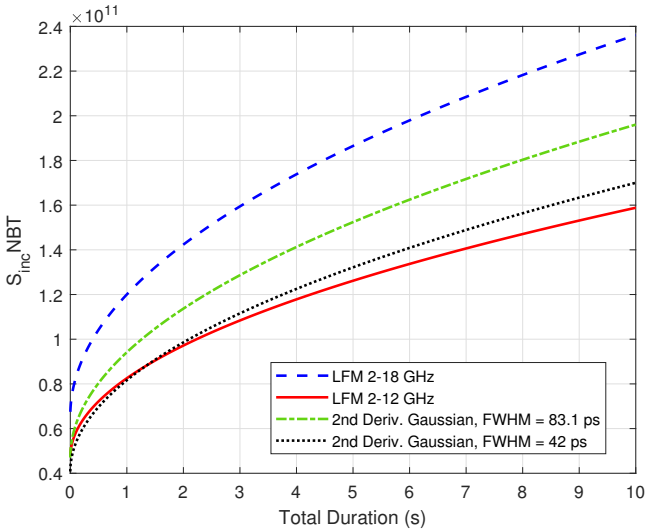

Figure 3.8: Total collection time vs. maximum SNR factor for the second-derivative Gaussian pulse and the LFM taken from Fig. 3.7 for comparison

bandwidth and the bandwidth distribution across regulatory frequency bins impacts the difference between the SNR factor of the two pulse widths. The maximum SNR factor across test time is shown in Fig. 3.8, along with the highest and lowest SNR factor scenarios studied for the LFM. Though the time-bandwidth product of the second-derivative Gaussian pulse is much smaller than the LFM, the short pulses can be rapidly accumulated to increase SNR through coherent integration.

The PRF of realistic UWB systems is typically 1-10 MHz, which corresponds

System	B (GHz)	T	PRF	Max. S_{inc}	Max. SNR Factor
FMCW [8]	2-18	240 μs	3.9 kHz	57.9 kW/m^2	8.67 $\times 10^{10}$
FMCW [83]	2.7-10.7	140 μs	5.6 kHz	79.9 kW/m^2	5.01 $\times 10^{10}$
UWB [84]	2.5-12.5	41 ps	10 MHz	132 MW/m^2	5.36 $\times 10^{10}$
UWB [85]	1.2-6.2	173 ps	1 MHz	741 MW/m^2	6.41 $\times 10^{10}$

Table 3.2: System parameters and the corresponding incident power density and SNR factor limits set by ICNIRP basic restrictions for a 100 ms exposure time

to a duty cycle lower than 0.1% [84, 85]. In contrast, FMCW systems often have duty cycles of 75-95% [8, 83]. Illuminating the body for more time decreases the allowed incident power density. Conversely, the transmit power must be increased proportionally to any duty cycle decrease to maintain the same SNR factor within a given collection time. Therefore, UWB systems require a transmit power that is at least three orders of magnitude larger than FMCW systems to achieve a similar SNR factor. Achieving a high power output is generally more difficult for UWB systems because of the short pulse duration. The allowed S_{inc} and SNR factor values for several systems are summarized in Table 3.2. The theoretically achievable SNR factor is similar for all of the systems, but the actual SNR factor capabilities may vary when implemented on real hardware.

Overall, the theoretical maximum SNR factor of the LFM and Gaussian pulse waveforms depends on the collection duration as well as the waveform's bandwidth and frequency distribution. The duty cycle of UWB systems is often several orders of magnitude lower than FMCW systems, so the transmitted power density of UWB systems must be several orders of magnitude higher to achieve a similar SNR factor in a given collection time. FMCW systems have more flexibility to operate throughout the scan time and SNR factor tradeoff region because of their high time-bandwidth product, high duty cycle capabilities, and freedom to change the pulse width and bandwidth independently. In addition, the system antennas can be chosen based on the desired size of illumination and gain requirements rather than minimizing the distortion of the Gaussian pulse. To further expand on this work, a framework for image degradation due to human movement must be built, enabling a more accurate guide for how long a realistic test duration can be.

3.3 Properties of Human Tissue

While tissue properties vary across the population, having a good estimate of the tissue permittivity and conductivity is essential for many elements of RF design, including antenna design, safety compliance, and radar link budget [34, 36, 86]. The examination of the electrical properties of human tissue is an area of active research [87, 88]. The mechanical properties of tissue can make it challenging to meet the shape or size requirements in the traditional characterization techniques discussed in Section 2.2, and changes in tissue properties depending on whether the sample is in vivo or ex vivo limits sample availability [89]. From 10 Hz to 100 GHz, human tissue displays four types of relaxation mechanisms. Each mechanism corresponds to a particular relaxation time, τ. In the extensive study by C. Gabriel, the 4-Cole-Cole model best fits the tissue behavior over the entire frequency span [90].

The IT'IS Foundation maintains a database of tissue parameter estimates and updates the values as new studies are released [91]. The permittivity and conductivity can be obtained for a selected frequency, or the 4-Cole-Cole parameters can be exported to use (2.11). The relative permittivity of the front layers of the Duke thoracic stackup used in Section 2.4 are plotted in Fig. 3.9. Tissue containing more water has a higher permittivity, as expected due to water's high permittivity, previously shown in Fig. 2.3a. The conductivity of the human materials is shown in Fig. 3.10. In general, the rate of increase of conductivity over frequency is faster than the rate of decrease of the permittivity, which yields an increasing loss tangent over frequency, which was also seen in the measurements shown in Fig. 2.4.

Note that the skin and muscle permittivities are much higher than the fat per-

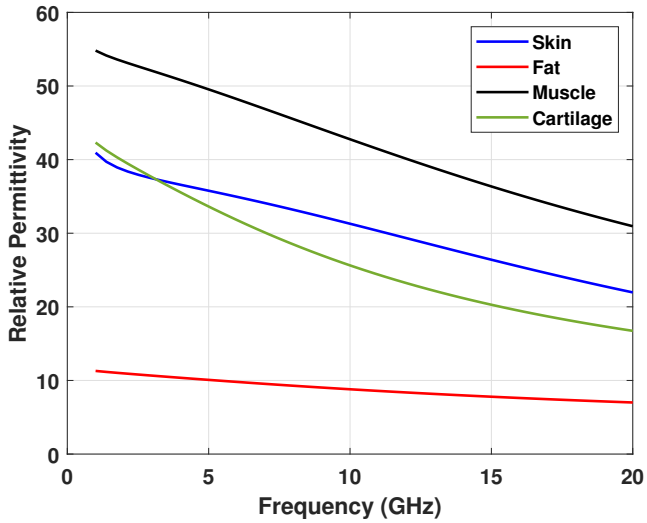

Figure 3.9: Relative permittivity of tissues according to [91]

mittivity, which lies between the skin and muscle in the thoracic stackup. As given by (2.14), a high contrast between material properties yields strong reflections. The permittivity changing from high to low and then back to high across these three layers created the changing power levels, reminiscent of a dielectric resonator, in Fig. 2.14.

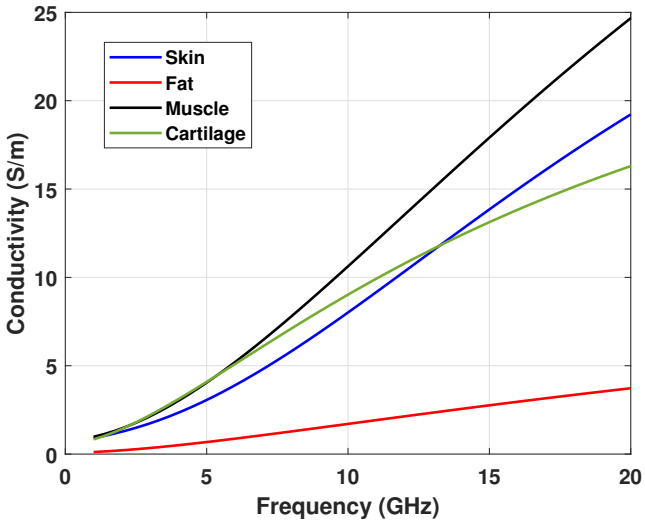

Figure 3.10: Conductivity of tissues according to [91]

Chapter 4

Radar Techniques

4.1 Range Profile Creation

In the most classic form of radar, a waveform is transmitted, reflects off of an object R_0 m away, and returns back to the radar t_0 seconds later. By measuring this delay, the radar can extract how far away the object is located with the following relation:

$$R_0 = \frac{v_p t_0}{2} \ , \tag{4.1}$$

where v_p is the electromagnetic wave's velocity of propagation, which is equal to the speed of light in free space. This information is used to construct a range profile, which consists of peaks indicating objects' location and radar cross section (size). Important metrics to assess the quality of a range profile include signal-to-noise ratio (SNR) and resolution. Signal-to-interference ratio (SIR) and signal-to-clutter ratio (SCR) also impact how well information can be extracted from a range profile. For a simple pulse, meaning a rectangular pulse of length τ containing a single

frequency, the range resolution (ΔR) is given by

$$\Delta R = \frac{v_p \tau}{2} \ , \tag{4.2}$$

meaning that the range resolution is refined by decreasing the pulse length. However, shortening the pulse decreases the transmitted energy and, subsequently, the received energy.

In most radar modes, the transmitted waveform propagates through air before reflecting off the outside of an object and traveling back toward the radar. In most cases, the scatterer of interest is an inanimate object, so the transmit power is selected based on system capabilities and spectrum regulations. The radar range equation describes the ratio of power received (P_r) to power transmitted (P_t) for a waveform reflecting off of a scatterer at range R with a radar cross section of σ, and the relationship is given by:

$$\frac{P_r}{P_t} = \frac{G^2 \lambda^2 \sigma}{(4\pi)^3 R^4 L_s L_a(R)} \ , \tag{4.3}$$

where G is the antenna gain, λ is the wavelength, L_s is system loss, and $L_a(R)$ is atmospheric loss [1].

Pulse compression waveforms aim to decouple the relationship between energy and range resolution using some sort of modulation scheme. Samples of the received waveform are typically converted to a range profile with a matched filter, which optimizes the SNR [92]. The SNR at the beginning of the receiver is given by:

$$SNR = \frac{P_r}{P_n} \tag{4.4}$$

where P_n is the noise power. The SNR of the range profile created with a pulse compression waveform is improved by its time-bandwidth product, meaning the length of time illuminating the scene and the transmitted frequency bandwidth. The white noise power of an ideal receiver is given by

$$P_n = kTB_n \ , \tag{4.5}$$

where k is Boltzmann's constant (1.38x10^{-23} J/deg), T is the receiver temperature (Kelvin), and B_n is the receiver bandwidth. In reality, each component within a receiver contributes some noise, indicated by its noise figure (F_n), and these values are cascaded together along with any component gains (G_n) to form the total noise figure, given by:

$$F = F_1 + \frac{F_2 - 1}{G_1} + \frac{F_3 - 1}{G_1 G_2} + \cdots + \frac{F_N - 1}{G_1 G_2 \cdots G_{N-1}} \tag{4.6}$$

where the index of each component corresponds to the order in which the components are encountered by the incident wave in the receive chain [92]. The total noise figure increases the noise power of the sampled data. Thus, placing a low-noise amplifier early in the receive chain is important to reduce noise.

While a single, static range profile can provide valuable information, combining multiple pulses can reveal even more details about the measurement scene. A moving target shifts the frequency of the incident wave through the Doppler effect [1]. The amount of frequency shift due to Doppler of an object moving with a radial velocity, v, is given by:

$$F_D = \frac{2v}{\lambda_0} \ , \tag{4.7}$$

where λ_0 is the transmitted wavelength. Range-Doppler plots display where the targets in the scene are located and how quickly they are moving towards or away from the radar. A popular method of radar imaging is synthetic aperture radar (SAR), where the Doppler information is leveraged to correlate the radar data with a theoretical phase history to form a pixel map indicating the scattering power within each pixel [1].

A practical consideration for creating a range profile is the signal digitization. The most fundamental requirement is the Nyquist criterion, which states that the analog signal must be sampled at a rate double the highest frequency to avoid aliasing [93]. As there may be frequencies present that are higher than the transmitted frequencies, either from system component harmonics or outside interference, filters are required to remove frequency content from outside the desired band. An analog-to-digital converter (ADC) bit resolution sets the level of magnitude of the stored details. Typically, ADCs with slower sampling rates are more affordable and/or are capable of a better bit resolution. Therefore, radar architecture is often designed to lower the required sample rate by mixing down the received signal to either an intermediate frequency (IF) or baseband (centered around 0 Hz).

4.2 Radar Trade-offs

Radar design requires working through many trade-off spaces, including weighing performance against the system's size, weight, power, and cost (SWaP-C) requirements. System performance requirements are often defined for parameters such as SNR, SCR, collection time, Doppler tolerance, and dynamic range. Radar engineers have been working since the advent of radar to optimize these trade-offs,

both in the system hardware and the post-processing.

Dynamic range is the difference between the largest and smallest signal that the radar can capture. A large dynamic range may be unnecessary if a radar collects measurements of similarly sized scatterers with minimal near-range clutter or interference. On the other hand, sensing within the body highly prioritizes a significant dynamic range. The reflection off the air-skin boundary is much larger than a reflection received from deep within the body, and both reflections are typically too close in time to temporally separate through other means, such as range gating [34]. If possible, the dynamic range requirements are reduced. One method is receiver blanking, where the receiver is shut off during the largest return and then turned back on for the desired smaller return. This practice is common when the largest return is from close-range ground clutter and the desired scatterer is far away. Another strategy is applying electromagnetic matching to reduce the large scatterer, such as applying a matching medium to reduce the external skin reflection [51]. The dynamic range that a system can handle can also be increased by utilizing an ADC with more bit resolution. With a reasonable estimate of the received power levels, the amplifiers within the system can be carefully selected to amplify the signals as much as possible without being pushed into saturation. A mixer with higher power-handling capabilities is helpful as well.

In additive noise, the most straightforward method to improve the measurement's SNR is to increase the transmit power if the system can handle it and spectrum use restrictions allow. If this is not possible, a common SNR improvement strategy is to increase the time spent illuminating the target, either to improve the pulse compression gain or coherently average multiple transmissions together [1].

This strategy is effective if the scene is sufficiently stationary and the dominant noise is uncorrelated, which is the case with additive white Gaussian noise (AWGN) [1]. If the noise is correlated or the actual performance limiter is the signal-to-clutter ratio (SCR), averaging does not provide significant measurement quality improvement. Unlike additive noise, clutter is multiplicative, so increasing the transmit power does not help raise the signal of interest above clutter levels. To improve SCR, utilizing more directive antennas can physically limit how much clutter is being illuminated during the collection.

Quickly changing environments require even more radar design considerations. A waveform's Doppler tolerance describes how well the range profile integrity is maintained when increasingly large amounts of Doppler shift are applied [94]. Long pulse lengths or coherent integration schemes of many pulses also pose an issue because the target may migrate in range within a single pulse or blur across averaging points. This challenge is encountered in classic radar applications when a vehicle moves quickly. Biomedical radars may experience similar effects when inspecting the torso due to the breathing-induced chest motions [95].

With the increased availability of software-defined radios (SDR), implementing more unique waveforms has become feasible for a larger population. The radar waveform selection is a significant driver of the system's SWaP-C requirements. Orthogonal Frequency-Division Multiplexed (OFDM) waveforms have begun to be used for radar despite the waveform's high peak-to-average-power ratio because each of its high temporal efficiency and potential for dual-purpose radar and communications fusion [96]. Time-domain pulsed waveforms like the Gaussian pulse can be generated with simple hardware, but the high sampling bandwidth require-

ment and lack of pulse compression gain pose a challenge. These pulsed waveforms have been common in biomedical imaging applications because of the high spatial resolution [76].

Biomedical radar applications also commonly use step frequency continuous wave (SFCW) and frequency-modulated continuous wave (FMCW) radar modes [97, 98]. An SFCW radar transmits and receives a single frequency before moving on to the subsequent frequency until the desired bandwidth has been populated. A VNA, which is already available in many workspaces, can function as an SFCW radar. The primary disadvantage to SFCW radar is how long it takes to cover the desired bandwidth due to the energy-inefficient transmission and reception of only one frequency at a time. Because each frequency is individually mixed down to baseband, an extremely narrow IF filter can be implemented to reduce thermal noise. While this narrow IF filter is beneficial from a noise perspective, shifting this narrow filter across each frequency band and waiting for the signal to settle adds significant time to the measurement [99]. FMCW radar waveforms solve the temporal challenge of SFCW radar, and the next section elaborates upon the features of this modality.

4.3 FMCW Radar

FMCW radar is of interest in this work because a high bandwidth can be achieved with low sample rate requirements and relatively fast collection time [100]. A radar pulse with linearly increasing frequency, also known as a chirp, is transmitted. The received signal, which is a superposition of delayed copies of the transmitted waveform, is mixed with the transmitted signal. The phase difference between the re-

ceived and reference chirps yields a mixer output of frequencies corresponding to the ranges of the scatterers, often referred to as "beat frequencies." Beat frequencies are much lower than those in the transmitted waveform, particularly for close-range scatterers or systems with slow chirp rates. To extract range information, the matched filter is simply the Fourier transform of the mixer output, as the peaks in the frequency domain correspond to the ranges of the scatterers.

The transmitted waveform, $x(t)$, with initial frequency F_o and pulse width T_p is defined as

$$x(t) = \text{rect}\Big((t - 0.5T_p)/T_p\Big)\cos(2\pi F_o t + \pi\gamma t^2) \tag{4.8}$$

where t is time, and γ is the chirp rate related to the transmitted bandwidth (B) by

$$\gamma = \frac{B}{T_p}\ . \tag{4.9}$$

The received signal ($x_r(t)$) is a delayed copy of $x(t)$. The time delay of a return from an object at range R_o obeys the relation in (4.1). Therefore, the received signal

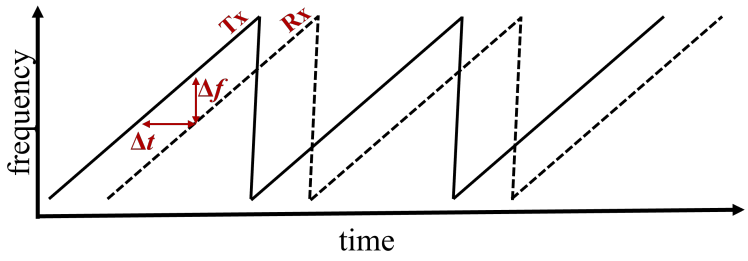

Figure 4.1: Frequency content over time of linear frequency-modulated chirps in an FMCW radar mode

is

$$x_r(t) = \alpha(f)\text{rect}\Big((t - 0.5T_p)/T_p\Big)\cos\Big(2\pi F_o(t - \tau_o) + \pi\gamma(t - \tau_o)^2\Big) \tag{4.10}$$

where $\alpha(f)$ is the frequency-dependent attenuation, given by the radar range equation in (4.16). Direct sampling $x_r(t)$ would require an enormous sampling bandwidth to achieve fine range resolution with a wide transmitted bandwidth. Instead, stretch processing is commonly applied to reduce the sampling bandwidth requirement while maintaining the transmitted waveform bandwidth [101]. The frequency content over time of a series of chirps is shown in Fig. 4.1.

Stretch processing reduces the required sampling bandwidth by mixing $x_r(t)$ with a reference copy of the transmitted waveform before reaching the ADC. If the reference signal is delayed by τ_0, corresponding to a range of R_0, then the output of the mixing process is

$$\begin{aligned} x_{r,IF}(t) =& \text{rect}\Big(\frac{t - \tau - 0.5T_p}{T_p}\Big)e^{j8\pi\gamma R_0(R-R_0)/c^2} \\ & \cdot \Big[e^{-j4\pi F_0(R-R_0)/c}e^{j2\pi(-2\gamma(R-R_0)/c)t}e^{j4\pi\gamma(R-R_0)^2/c^2}\Big] . \end{aligned} \tag{4.11}$$

The first term of the second line provides Doppler information across pulses, and the third term is the residual video phase, which can be leveraged in some advanced synthetic aperture radar (SAR) techniques [1]. The second term is most interesting for extracting range information because it is a complex sinusoid with a frequency that is linearly dependent on range. The frequency of this term is referred to as the

beat frequency (F_b), given by

$$F_b = -2\gamma(R - R_0)/c \; . \tag{4.12}$$

As the received signal has a rectangular amplitude envelope, the Fourier transform of the sinusoid yields a sinc function centered at the beat frequency [1]. Thus, the required sampling bandwidth has been reduced from B or $2B$, depending on if a quadrature channel is implemented, down to the bandwidth of the beat frequencies (B_{IF}), which is

$$B_{IF} = 2\gamma R_w/c \tag{4.13}$$

where R_w is the range swath. If the ADC only collects a single, real data channel, then the minimum sample rate is $2B_{IF}$.

As mentioned above, the range profile is stored in the range-dependent frequencies, and the sampled received signal must be transformed to the frequency domain to yield range-dependent peaks. In this case, the matched filter is the discrete Fourier transform (DFT), commonly depicted as

$$Y_{r,IF}(\omega) = DFT(x) = \sum_{n=0}^{N-1} e^{-j\omega n} \tag{4.14}$$

where n is the frequency index and $Y_{rIF}(\omega)$ is the frequency spectrum of the received mixed-down data. However, for digital implementation, it is easier to ana-

lyze the DFT in its matrix form, be represented as

$$Y_{r,IF}(\omega) = DFT(x) = \begin{bmatrix} e^{j\omega_0\tau_0} & e^{j\omega_1\tau_0} & \dots & e^{j\omega_{N-1}\tau_0} \\ e^{j\omega_0\tau_1} & e^{j\omega_1\tau_1} & \dots & e^{j\omega_{N-1}\tau_1} \\ \vdots & \vdots & \ddots & \vdots \\ e^{j\omega_0\tau_{M-1}} & e^{j\omega_1\tau_{M-1}} & \dots & e^{j\omega_{N-1}\tau_{M-1}} \end{bmatrix}, \tag{4.15}$$

where τ_m is a sample time step.

The range resolution (ΔR) is related to the bandwidth by

$$\Delta R = \frac{v_p}{2B} = \frac{v_p}{2\gamma T_p}. \tag{4.16}$$

Note that when traveling through a medium with a v_p slower than the speed of light, the resolution will be better than in free space, an effective superresolution effect. This means that radar transmitted into the body can achieve a better resolution with less bandwidth than free-space radar applications.

While the frequency content within the transmitted chirp is ideally continuous throughout the bandwidth, signal generators cannot achieve this. Instead, discrete frequencies are transmitted sequentially, with some uniform spacing, Δf. To avoid aliasing, care must be taken to ensure that the farthest scatterer does not exceed the maximum unambiguous range (R_{max}), which is

$$R_{max} = \frac{v_p}{2\Delta f}\ . \tag{4.17}$$

A more prominent challenge in FMCW radars employing stretch processing than many other architectures is $1/f$ noise, commonly referred to as pink or flicker

noise. The noise is highest at low frequencies and decreases in magnitude with a slope of $1/f$, as evident from its average mean-square value ($overlinee^2$), given by [102] to be:

$$\overline{e^2} = \int (k_e^2/f)df \tag{4.18}$$

where k_e is a component-specific constant value. Especially for short-range applications, pink noise can be of higher magnitude than white noise [103]. This frequency-dependent noise is more challenging to handle than white noise because it is temporally correlated, meaning that coherent integration does not improve the SNR.

The beat frequency can be manipulated by either changing the transmit signal or the range to the target. The beat frequency can be increased by increasing the transmit frequency spacing or decreasing the dwell time at each point. The frequency spacing must still be fine enough to meet the unambiguous range requirements in (4.17). Increasing the range to the target also increases the beat frequency; however, the received signal is significantly more attenuated due to the increased spherical spreading loss, proportional to R^4 in (4.3). To overcome this, optical delay lines can be employed to increase the range without significantly increasing the loss. On the other hand, if a lower beat frequency is desired to reduce sample speed requirements, an optical delay line can be added to the reference signal path. When the reference signal is more delayed, there will be the smallest phase difference and, subsequently, the smallest beat frequency, with received signals at a delay similar to the reference delay.

Chapter 5

Compensation for Changing Velocity of Propagation

The matched filter described in (4.15) assumes the phase rotation across the matrix is uniform in relation to time and frequency progression, i.e., all of the matrix entries are evenly spaced. This assumption is valid for classic radar applications where the transmitted wave travels at a constant rate through the air. When the transmitted waveform instead travels through multiple media, the rate of phase rotation is non-homogeneous. As the wave travels through a medium other than free space, the phase progression slows down, according to (2.8). With multiple media, there is a varying phase progression along the spatial dimension of the received data. If the media properties vary across the transmitted bandwidth, then there is a second variance along the frequency dimension. If a matched filter is not a perfect representation of the received waveform, either in amplitude envelope or phase progression, then the output range profile is not composed of ideal sinc functions. Typically, the sidelobes are raised, and the main lobe is broadened. This chapter aims to explore the consequences of varying velocities of propagation on the output range profile in simulation and derive a method to compensate for these changes.

5.1 Compensation Through Space

While the actual phase progression is a function of the material properties across the transmitted bandwidth, the received data in stretch processing has already been down-converted to a much narrower IF bandwidth. In stretch processing, the sample progression recorded by the ADC does not directly correspond to the range of the scatterers. In other words, sample K does not represent scatterers farther away than sample $K-1$. Particularly in close-range systems, the spacing between ADC samples may be much greater than the entire range swath. Instead, the sample sequence represents the progression through the transmitted waveform. For an upward-chirping LFM, sample K corresponds to a higher frequency within the transmit waveform than $K-1$. The sinusoids with range-dependent beat frequencies can be extracted by looking at all of the ADC samples over time, as described in Section 4.3.

Suppose the electrical parameters of the materials in the range profile are relatively constant over frequency, either due to a narrow operation bandwidth or stable material properties. In that case, compensation is only necessary across space. With an estimate of the materials' expected electrical properties and physical geometry, a compensatory matched filter is constructed by compressing the rate of rotation along the columns of (4.15) proportionally to the expected velocity of propagation across space. Instead of implementing evenly-spaced values of ω in the exponents corresponding to evenly-spaced beat frequencies, the spacing across the ω vector reflects the stretching of the received waveform. To increase the phase progression between two samples and therefore compensate for the velocity-induced stretching,

the spacing between frequency points ($\Delta\omega$) within medium K is set to

$$\Delta\omega(k) = \frac{c}{v_{p(k)}}\Delta\omega_0 \tag{5.1}$$

where $\Delta\omega_0$ is the frequency resolution in free-space, $v_p(k)$ is the anticipated velocity of propagation within medium K, and c is the free-space velocity of propagation. Each beat frequency can be compensated for based on the previous beat frequency's corresponding physical location and the expected $\Delta\omega$ for the current range bin. This recursive relationship is stated as

$$\omega_n = \omega_{n-1} + \Delta\omega_n \ . \tag{5.2}$$

Thus, the compensatory matched filter matrix appears the same as in (4.15), except the progression of the ω values across the rows is no longer linearly spaced, but rather, spaced according to (5.1).

5.2 MATLAB Simulation Configuration

First, the impact of the velocity compensation matrix is studied through simulation to isolate the effects of the signal processing without other confounding system variables. Some radar simulations are conducted at baseband to reduce computational complexity. For this work, wave propagation is explicitly modeled at RF to capture the correct frequency-dependent behavior. The simulation process is summarized in Fig. 5.1. First, propagation parameters are calculated for each layer based on each user-defined layer thickness, permittivity, and conductivity. The user-

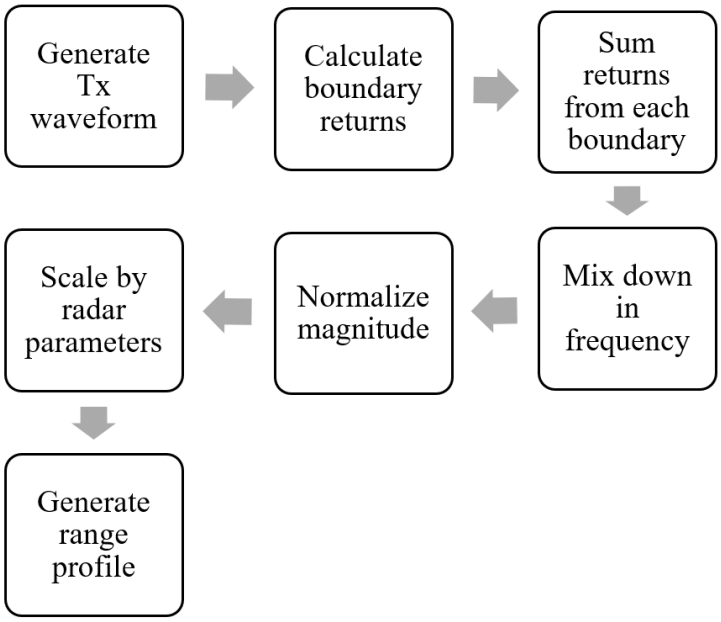

Figure 5.1: Block diagram of radar simulation

defined electrical properties are linearly interpolated to align with the simulation's frequency grid. The reflection off each boundary, as well as the attenuation and phase change within each layer, are calculated with these material properties. The transmitted radar waveform is created based on the user-defined bandwidth, center frequency, and sample rate. For each boundary, a copy of the transmit waveform is scaled in magnitude and phase to correspond to the calculated propagation to the boundary and back to the radar as well as the reflection coefficient of the boundary according to (2.14). As the received waveform is the superposition of all the reflections, the calculated returns are added together with the user-defined noise.

To mimic the frequency downconversion in an FMCW system, the simulation's received signal is element-wise multiplied by the transmitted waveform. This multiplication yields two products: one centered at the difference between the two input

frequencies and one at the sum of the two input frequencies. To avoid a high sample rate or aliasing, only the product at the difference of the input frequencies is desired. After downconversion, a low-pass filter is applied to the signal, with a cut-off frequency equal to twice the defined ADC sample rate. The filtered signal is then resampled at the ADC sample rate. At this stage, the downsampled signal is normalized to ensure that the height of the range profile matches a physical system. First, the normalization factor is calculated as the L2-norm of the downsampled transmit signal. By dividing the downsampled receive signal by this factor, a range profile height of "1" corresponds to a received reflection that is equal in power to the transmit waveform. The normalized frequency content can then be multiplied by the relevant radar parameters to match the power levels in a physical radar system, as defined by the radar range equation and the waveform time-bandwidth product [1]. At this stage, the simulated data are ready for range processing. For a matched-filter output, the samples are match filtered with a fast Fourier transform (FFT) to view the range profile in the form of beat frequencies. This stage is also where the FFT can instead be replaced with the compensatory matrix.

To verify the performance of the compensation matrix, simulations of several scenarios are executed with increasing complexity. Unlike actual radar operation,

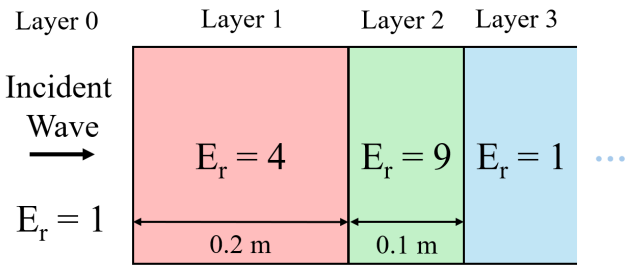

Figure 5.2: Target configuration for initial FMCW simulation

Parameter	Simulated Value
Frequency Range	5-11 GHz
Chirp Length	1 ms
Tx Frequency Spacing	10 MHz
Power	Normalized
RF sample rate	27.5 GHz
IF sample rate	1 MHz

Table 5.1: Radar parameters implemented in simulation of dielectric slabs

the exact material properties and thickness are known because the simulation defines the parameters. The simulation will still suffer from the consequences of sampling a waveform, including straddle loss, where the magnitude of the return is reduced when a reflection originates from between two range bins [1, 104]. In dielectric media, range straddling is dictated by the "effective" range bin location with respect to the bandwidth, not the physical dimension. For example, the range bin spacing in a relative permittivity of 9 is effectively 1/3 the spacing compared to the same bandwidth in free space, as given by (4.16).

The first simulated range profile is three dielectric slabs with permittivities that are constant across frequency and have no conductivity to study a radar scene that changes through space. The specific dielectric configuration is shown in Fig. 5.2. The third layer is effectively infinite, meaning no reflections originate beyond the boundary between layers 2 and 3. This configuration yields a result that can be easily calculated using (2.8) for comparison because the permittivities yield v_p values that are integer multiples of c. Table 5.1 summarizes the initial radar parameters. Suppose a physical boundary occurs in the middle of a range bin. In that case, a weighted average value is assigned as that bin's $\Delta\omega$ when calculating the spacing in the compensation matrix.

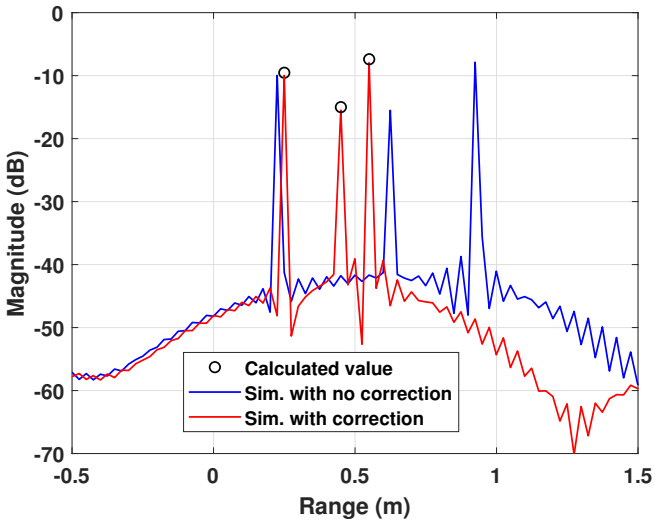

Figure 5.3: Simulated range profile of three dielectric slabs processed with the traditional matched filter and the compensatory matched filter compared to analytically calculated values

The initial simulated range profiles with the matched filter and compensatory matched filter are shown in Fig. 5.3. The calculated locations and power levels are plotted as circles. The power levels are normalized such that a complete reflection off the layer 0-layer 1 boundary would result in a range profile peak at 0 dB. Because the compensation is done after downsampling, the map from IF to RF frequencies will not be able to capture the entirety of the RF behavior perfectly. The sidelobe structure is changed slightly due to the addition of discontinuities in the phase progression within the v_p phase compensation matrix. Overall, the compensation matrix successfully aligns the boundary reflections to the correct range location while maintaining the same power level. As materials in the real world are not lossless, the experiment is repeated with a conductivity of 0.5 assigned to Layer 1. The subsequent range profiles are shown in Fig. 5.4. The added condcutivity

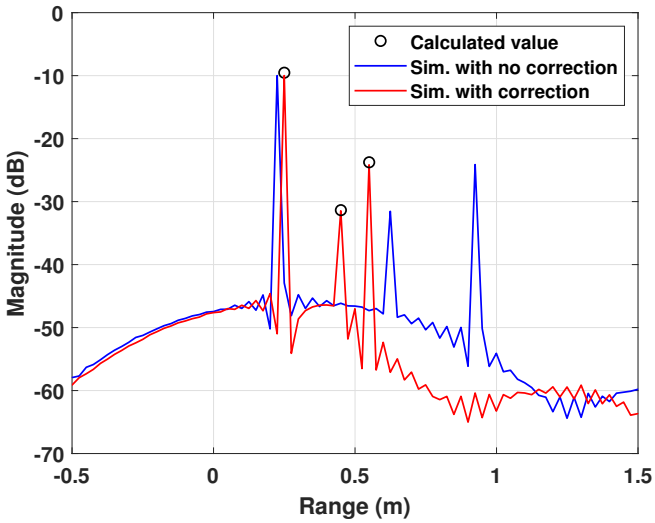

Figure 5.4: Simulated range profile of one lossy and two lossless dielectric slabs processed with the traditional matched filter and the compensatory matched filter compared to analytically calculated values

attenuates the returns originating beyond layer one, but the returns still appear at the correct range and magnitude.

5.3 Compensation Across Space and Frequency

While some materials do have a permittivity and conductivity that are relatively constant over a wide bandwidth, many materials, including the human tissue discussed in Section 3.3 and the liquids measured in Section 2.2, have electrical properties that vary over frequency. This dispersive behavior means that at a given point in space, the velocity of propagation will vary depending on which frequency in the transmitted waveform is currently incident. The spatial compensation discussed above will not wholly capture the propagation phenomena, so it is essential also to consider frequency-varying materials in this analysis.

Because the material information is at RF while the sampled data is at IF, an extra step is necessary to correct behavior at the frequencies of propagation. The ADC sample spacing is constant in time, but the distance the wave travels between samples is a function of both the wave's point in space (i.e., which material it is in) and the RF frequency contributing to the sample. Therefore, each ADC sample must be matched to the RF frequency that arrived at the radar at the sample collection time. Recall that the ideal transmitted chirp, given by (4.8), has a defined relationship between frequency and time. Thus, the transmitted ω can be calculated for a receive sample time t with

$$\omega(t) = 2\pi(F_0 + \gamma t) \ . \tag{5.3}$$

If the chirp and the ADC collection begin simultaneously, then the linear chirp over time can be mapped to the ADC sample times using this relationship. For example, an ADC collected at $t = 50$ ms corresponds to the frequency at the center of a 100 ms chirp. For short-range applications, the propagation delay from the radar to a scatterer is orders of magnitude less than the time between ADC samples. However, if this is not the case, then an adjustment factor could be added to the mapping to account for delay (e.g., the ADC sample at 15 μs corresponds to the point in the chirp at t = 14 μs).

Building upon the compensatory modifications to the DFT matrix discussed in Section 5.1 that varied the phase progression across the beat-frequency/range dimension, the full compensatory matrix must also vary along the ADC sample/-

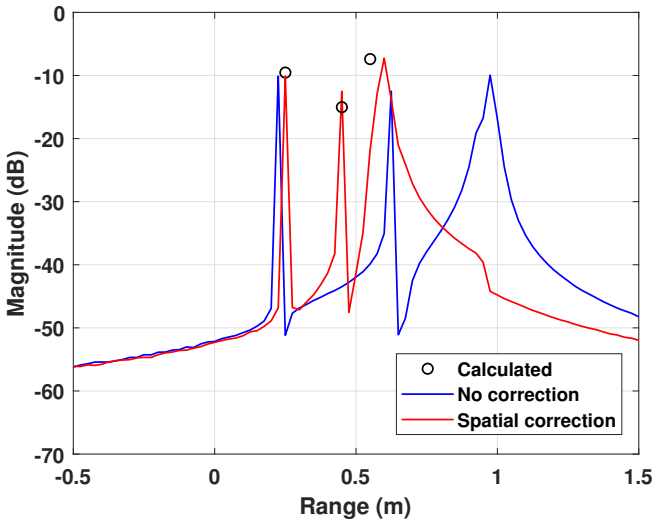

Figure 5.5: Simulated range profile of one dispersive dielectric slab between two slabs with constant permittivity, processed with the traditional matched filter and a compensation matrix with corrections only along the spatial domain compared to analytically calculated values

transmitted RF dimension. The compensatory transform (CT) is then

$$CT(x) = \begin{bmatrix} e^{j\omega_0\tau_{0,0}} & e^{j\omega_1\tau_{0,1}} & \dots & e^{j\omega_{n-1}\tau_{0,n-1}} \\ e^{j\omega_0\tau_{1,0}} & e^{j\omega_1\tau_{1,1}} & \dots & e^{j\omega_{n-1}\tau_{1,n-1}} \\ \vdots & \vdots & \ddots & \vdots \\ e^{j\omega_0\tau_{m},0} & e^{j\omega_0\tau_{m},1} & \dots & e^{j\omega_0\tau_{m,n-1}} \end{bmatrix} \tag{5.4}$$

where $\tau_{m,n}$ is given by

$$\tau_{m,n} = \tau_{m-1,n-1} + \frac{v_{p(m,n)}}{c}\tau_0 \tag{5.5}$$

where τ_0 is the ADC sample spacing and $v_{p(m,n)}$ is the anticipated velocity of propagation at spatial sample m and frequency n.Requiring *a priori* knowledge of the

media stackup initially seems unreasonable. However, many valid assumptions can be made without comprehensive prior knowledge. For example, the skin layer on the outside of the body is generally consistent across the population within a few μm. The unknown boundary is often at the end of a range profile, like detecting a tumor or brain bleed. In these cases, the final layer thickness may be unknown, but the path to the boundary of interest is fairly simple to estimate. Some recent work in microwave tomography supplements measurements with optical or infrared imaging to better estimate the geometry [55].

To study compensation across two dimensions in simulation, the configuration in Fig. 5.2 is altered such that layer 2 has a varying permittivity. The relative permittivity is set to vary linearly from 8 at 5 GHz to 10 at 11 GHz. The spatial compensation used in Section 5.1 is applied, utilizing the mean permittivity to represent layer 2, and the results are shown in the "Spatial correction" trace in Fig. 5.5. While the peak from the front of layer 3 is moved in the correct direction, the peak is broad. By applying the correction across both the space and frequency dimensions of the matrix, the beat frequency smearing is corrected, as shown in Fig. 5.6. While difficult to see with the current sample rates, increasing the phase progression also visually pushes the sidelobes together, which is why there is not as deep of a null between peaks two and three after the full compensation scheme has been applied.

Suppose layer 2's permittivity decreased with frequency and varied even more. The simulated range profile in Fig. 5.2 is updated such that layer 2's permittivity now begins at 11 at 5 GHz and decreases to 7 at 11 GHz. The subsequent range profiles are given in Fig. 5.7. The uncorrected peak is even wider from the beat frequency smearing. By applying the correction across both space and frequency,

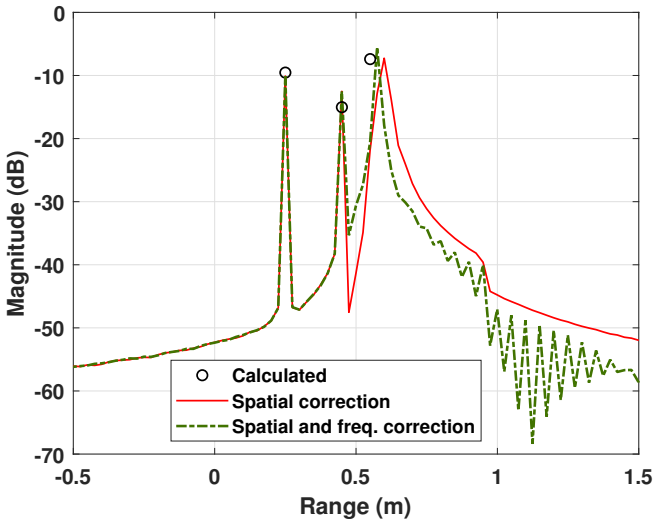

Figure 5.6: Comparison of range profiles created with compensation across space vs. space and frequency for a dispersive dielectric stackup

the peaks are successfully condensed to the appropriate width. However, the magnitude of the second and third peaks does not align perfectly with the calculation. One contributing factor is that the sidelobes from the peaks interfere with each other.

This technique has been demonstrated to work well when the permittivity is exactly known a priori. However, this constraint is not always feasible, particularly for biological tissue. To investigate the impact of error in the permittivity estimation on the range profile compensation, some error is intentionally introduced into the simulation. The same simulation parameters from Fig. 5.5 are used here. The permittivity estimate for layers 1 and 2 is increased and decreased by 10%, and the subsequent range profiles are compared to the range profile created using the correct values in Fig. 5.8. As expected, if the permittivity estimate is too low, the range profile is not condensed enough. On the other hand, a high permittivity estimate compresses the range profile too much. While the correct permittivity estimate is

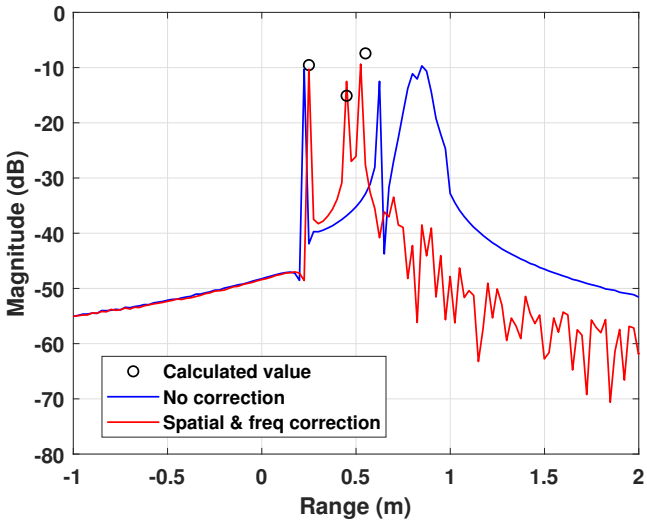

Figure 5.7: Simulated range profile with a decreasing permittivity assigned to layer 2, created with and without spatial and frequency-based velocity compensation compared to analytically calculated values

ideal, both range profiles generated with incorrect estimates are still closer to the actual values than the range profile with no correction from Fig. 5.5.

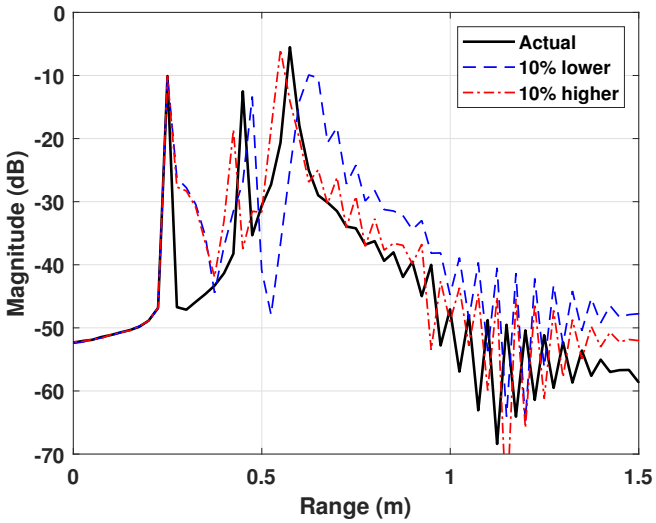

Figure 5.8: Simulated range profile with a decreasing permittivity assigned to layer 2, with velocity compensation completed with the simulated (actual) electrical parameters as well as with parameters 10% above and below the actual parameters

Chapter 6

Hardware Development and Initial Measurements

While simulations provide valuable feedback on a technique, physical measurements indicate how well a technique works in reality. Radar simulations typically only include ideal component behavior, so the impact of non-ideal behavior, such as harmonics and distortion, is not captured. This work aims to provide a demonstrator for the concepts explored in Chapter 5. Ultra-wideband FMCW systems often require custom hardware including filter banks and mixing stages [8, 72, 73]. In this initial investigation, only a prototype system is necessary. With access to several existing radar systems and spare components at the Advanced Radar Research Center, the goal is to create a radar by purchasing minimal new components. The initial FMCW radar prototype system is designed to operate from 2-14 GHz with scatterers placed a few meters away from the antennas.

6.1 Initial Component Selection

The component selection for an FMCW radar is critical for performance. The signal generator's sweep speed sets the chirp rate and subsequent beat frequencies, as described by (4.12). Some signal generators and mixers produce larger harmon-

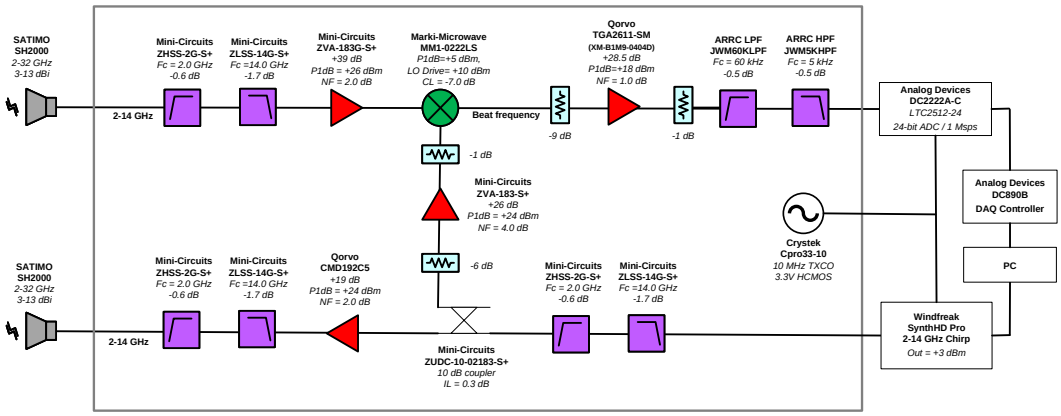

Figure 6.1: Block diagram of initial FMCW radar design

ics than others, which require significant filtering efforts to ensure a useful range profile can be extracted. The antenna directivity affects how much clutter is allowed into the capture as well as how much antenna coupling is received by the radar. The initial FMCW radar design for this work is shown in Fig. 6.1. The bandpass filtering at RF suppresses harmonics generated by any of the components, while the filtering before the ADC prevents aliasing from signals above half of the ADC sample rate. This particular ADC samples only real data with a single channel, so a Hilbert transform is applied in post-processing to yield complex samples [105]. The amplifiers and attenuators are selected to maximize SNR while avoiding saturation at any of the components.

To minimize phase noise, the signal generator and ADC are synchronized with a 10 MHz crystal oscillator. For initial experimentation, a Windfreak SynthHD Pro signal generator is selected due to its wide bandwidth (10 MHz to 24 GHz) and ease of use with a desktop control application. This signal generator must dwell at each frequency point for 1 ms, and a point spacing of 15 MHz or smaller

is required to satisfy the maximum unambiguous range requirement from (4.17). These restrictions lead to an overall slow chirp rate. The low chirp rate combined with the close target range creates a beat frequency on the order of 100 Hz. Most COTS RF components are not designed to function that low in frequency.

Maintaining signal integrity in both the time and frequency domain is critical for creating a quality range profile. Capacitors are often installed on RF transmission lines to behave as high-pass filters to isolate the transmission line from unwanted DC offsets. The size of the DC blocking capacitor sets its 3-dB cutoff frequency, given by

$$f_c = \frac{1}{2\pi RC} \tag{6.1}$$

where R corresponds to the transmission line's 50 Ω impedance and C is the capacitance. On the Minicircuits Galli-74+ amplifier selected for the IF path, the original DC blocking capacitors were 0.47 μF, corresponding to a cutoff frequency of 6.8 kHz. Increasing these capacitors to 50 μF allows frequencies as low as 65 Hz to pass through the amplifier. Another component that must be evaluated for low-frequency compatibility is the mixer. Even if a mixer chip supports an IF output down to DC, the connectorized version may have more restrictions. Connectorized mixers often employ a transformer that does not support low IF output frequencies. At the time of this publication, the Marki Microwave MM1-0222LS mixer used in this system is one of the only connectorized options that supports the required RF input bandwidth while also outputting low IF frequencies. To reduce the harmonics and interference allowed into the system from the signal generator and the environment around the radar, filters are placed at the signal generator output and both antenna ports. An additional filter is placed in the IF chain before the ADC

to remove any frequency content above the ADC's Nyquist frequency (half of the sampling rate) [93].

Designing a low-loss IF filter is challenging for a low cutoff frequency. The design process is the same as any low-pass lumped element filter, but component availability is more limited for the large capacitances and inductances required to achieve the low cut-off frequency. Thus, the realizable design may vary from the component values calculated with filter design equations. Inductors intended for high-power applications are selected because they have a low DC resistance, which reduces insertion loss. In this work, the original filter was selected to reject frequencies above 50 kHz for a 175.44 kHz ADC sample rate. As discussed in more detail later in this section, a downsample factor can be implemented to increase the SNR. With a downsample factor of 4, the effective sample rate is 43.9 kHz. Therefore, the IF filter must reject frequencies above 21.9 kHz. As the short-range beat frequencies of interest in this work will fall well below this frequency, the cutoff frequency is allowed to be decreased to accommodate the available components. The frequency response of the 11th-order filter designed with commercially available components, as simulated in Keysight Advanced Design System (ADS), has a cut-off frequency of 16.2 kHz, as shown in Fig. 6.2. The fabricated filter is shown in Fig. 6.3.

Setting the correct power levels for system components ensures proper operation. The antennas selected for this system are on hand at the Advanced Radar Research Center for project measurements. The antenna bandwidth is much broader than necessary (2-32 GHz), which comes at the cost of lower directivity compared to standard gain horn antennas, with a 3-dB beamwidth of 120° at 2 GHz. The

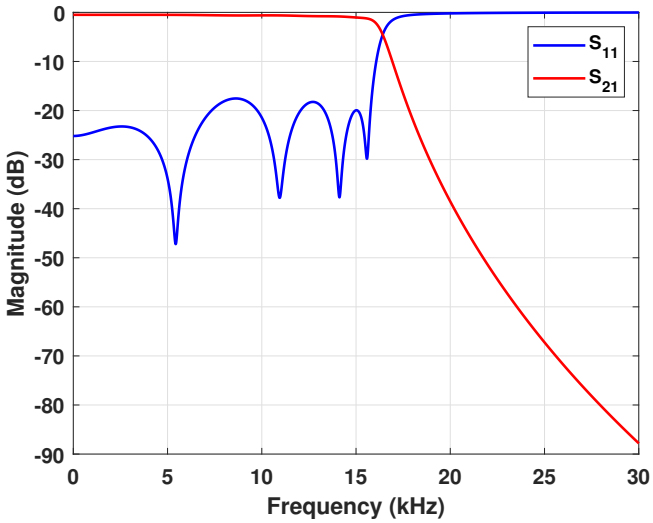

Figure 6.2: Simulated frequency response of low-pass filter designed for the receiver's IF path

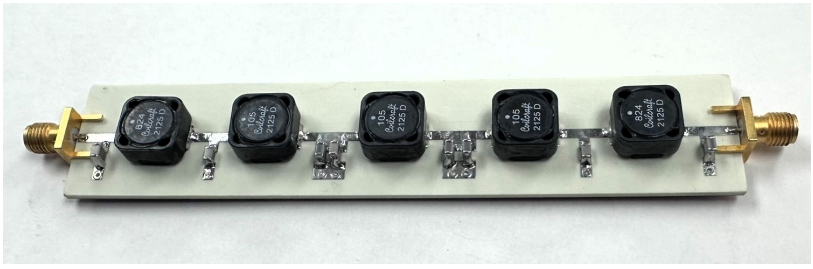

Figure 6.3: Low-pass filter fabricated for the receiver's IF path

selected amplifiers operate with high fidelity within their respective linear regions, and attenuators are placed, if necessary, to maintain linear operation. In the original design, the antenna coupling was the highest power return, which meant additional attenuation had to be added, lowering the system dynamic range. Metal baffles are placed between the antennas to reduce the received antenna coupling. The baffles have been measured to increase the antenna isolation by 25 dB. This improvement allows for less attenuation to be applied to the signals of interest, increasing dy-

namic range.

While the RF components are selected to handle 2-14 GHz, the initial system bandwidth is limited by the number of samples the ADC can hold. The Windfreak signal generator's minimum dwell time paired with the required frequency spacing to satisfy the maximum unambiguous range criterion results in a chirp that is 0.8 s long. The ADC can capture 65536 samples at one time, and the 10 MHz reference clock yields a sample rate of 175.44 ksps. Therefore, the ADC can only hold 0.37 s or 5.6 GHz of bandwidth. The operation parameters for the initial system are summarized in Table 6.1.

6.1.1 System Modifications

Beyond this initial design, a microcontroller has been added to trigger the signal generator and the analog-to-digital converter (ADC) to begin operation simultaneously. This triggering ensures that future collections aiming to study the velocity of propagation will have samples that begin at the same time as the chirp, which is necessary for the compensation algorithm. Even if the signal generator is set to

Parameter	**System Value**
Frequency Range	2-7.6 GHz
Chirp Length	373 ms
Tx Frequency Spacing	15 MHz
Tx Power (VNA Port)	3 dBm
Tx Power (Antenna Port)	19-24 dBm
ADC sample rate	175.44 kHz
ADC resolution	24 bits
ADC ENOB	14 bits

Table 6.1: Initial system parameters

transmit continuously, there may still be small gaps between chirps as the components are reset. Triggering the signal generator and ADC together ensures that the received signal appears within the same indices each time, simplifying data post-processing.

As discussed in Section 4.3 and in the above component selection process, there are challenges that come with extremely low beat frequencies. An example range profile measured with this system is shown in Fig. 6.4 along with a line sloped according to the expected pink noise distribution ($1/f$). The range profile is dominated by pink noise until about $R = 40$ m, where the additive white noise power is larger than the pink noise power. Ideally, the system is modified to move the signals of interest up into the white noise-dominant frequency range. In this system's case, increasing the beat frequency is not practical without major component modifications. The shortest optical delay line on hand at the Advanced Radar Research Center exceeded the maximum unambiguous range capabilities of the transmitter's chirp rate. Because a particular dwell time is required for the signal generator to move between frequencies, generating a waveform with finer spacing to increase the unambiguous range subsequently slows down the chirp—a slower chirp results in a lower beat frequency, negating the benefit of the optical delay line.

If a different transmitter were implemented to decrease the dwell time on each point, the pink noise power would decrease proportionally to the time decrease. However, the time spent illuminating the target is also decreased, so the time-bandwidth product is also reduced proportionally to any dwell time reduction, which negates the benefits of reducing the pink noise. Thus, no modifications are made to improve pink noise at this time. There are other benefits to reducing the chirp

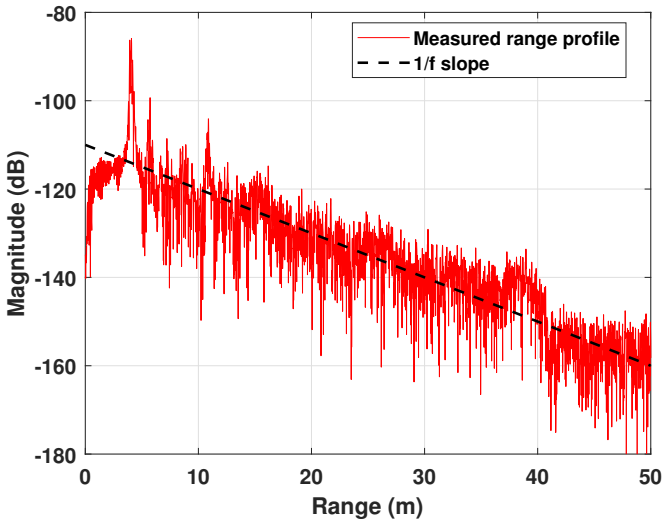

Figure 6.4: Measured range profile of a metal plate compared to the slope of 1/f pink noise

length that may be beneficial, though, such as avoiding range profile degradation in a changing environment.

6.2 Troubleshooting

To initially validate that the system works correctly, basic ranging is carried out with simple metal targets, such as a metal box, as shown in Fig. 6.5. This initial testing enabled the diagnosis of mixer distortion issues. All real mixers produce harmonics, though they may be too small to notice. Exceeding the mixer's rated power handling yields significant harmonics and a distorted range profile. Initial measurements of a large metal box are shown in Fig. 6.6. The range profile is mirrored several times about the range of 7.5 m, which is a classic sign of harmonics generated by the mixer.

To reduce these harmonics, the 6 dB attenuator between the coupler and the

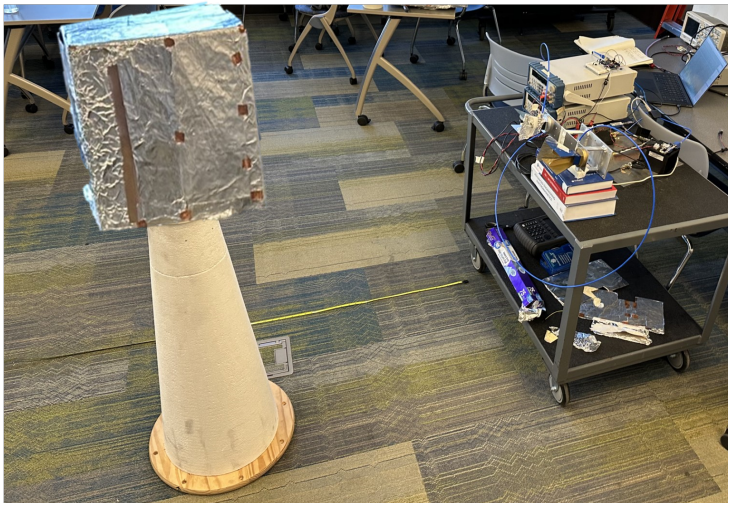

Figure 6.5: Measurement configuration for initial radar measurements

mixer has been replaced with a 9 dB attenuator. Additionally, metal baffles are placed between the antennas to reduce the antenna coupling [106]. The shape of the baffle is selected as a tradeoff between isolation and beam pattern distortion. Because this system aims to measure short-range targets, the antenna beamwidths must still overlap 1 m away from the radar to fully illuminate the target. Thus, rather than placing a large piece of metal between the antennas, smaller pieces of metal are placed on the inside edge of each antenna to provide moderate isolation improvement, as shown in Fig. 6.7. The coupling between the antennas is simulated in Ansys HFSS with and without the baffles from 2-4 GHz, which is the frequency range of the antennas' widest beamwidth, and up to a 25 dB isolation improvement is achieved, as shown in Fig. 6.8. The baffles are fabricated by custom-shaping cardboard to fit along the antennas and covering the cardboard with aluminum foil, as shown in Fig. 6.9. Similar isolation improvements are observed when measured with a Keysight FieldFox in an open outdoor environment.

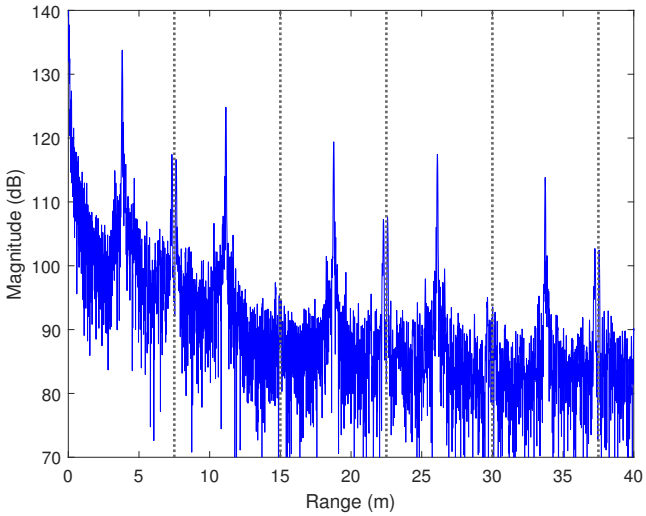

Figure 6.6: Measured range profile of a metal box with mixer distortion

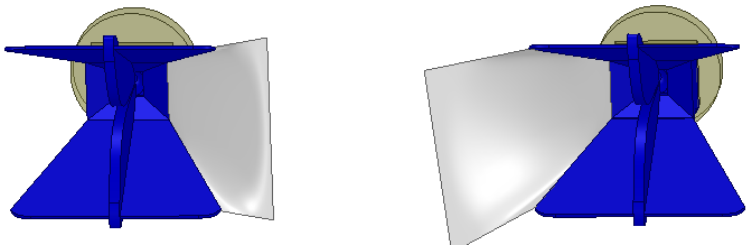

Figure 6.7: Simulation configuration of wideband horn antennas with metal baffles added on the sides

A loopback configuration, where the system's transmit and receive cables are directly connected to each other through an attenuator, is commonly used to isolate system performance from exterior environmental impacts. The range profile created by a loopback ideally has a single peak with a sharp rising edge. Sidelobes will accompany the peak, though adding a tapered window to the data should reduce the sidelobe levels [107]. Some small mixer harmonics distant in range from the primary return are expected as well.

To execute loopback measurements on the radar system, the transmit and receive

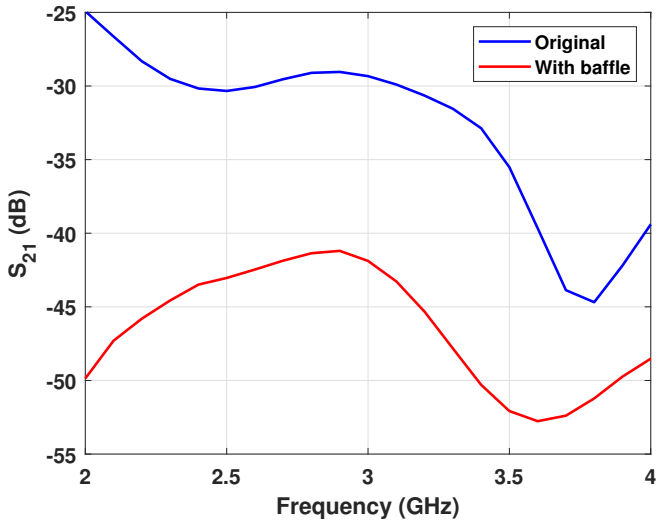

Figure 6.8: Simulated coupling between two wideband horn antennas with and without metal baffles added on their sides

ports of the radar are connected to each other through 3.66 m of coaxial cables and 49-dB of attenuation. The matched filter output is shown by the "3.66 m" trace in Fig. 6.10a. Note that the system has a non-zero reference range because there is some propagation delay through the reference path as well. Furthermore, the range is indicated in terms of one-way travel, whereas the cable length is provided in terms of total travel. Therefore, 1 m of cable corresponds to a range of $\sqrt{E_r}/2$. Coaxial cable permittivity typically varies from 1.7 to 2.2, depending on which dielectric is used to construct the cable. The group delay of a single cable is extracted from S_{21} measurements with

$$\text{group delay} = -\frac{\Delta\phi}{\Delta\omega} \tag{6.2}$$

where $\Delta\phi$ is the change in S_{21} phase angle and $\Delta\omega$ is the change in angular frequency from one measurement point to the next. The measured group delay for a single cable is shown in Fig. 6.11 to be approximately 8.725 ns across the full mea-

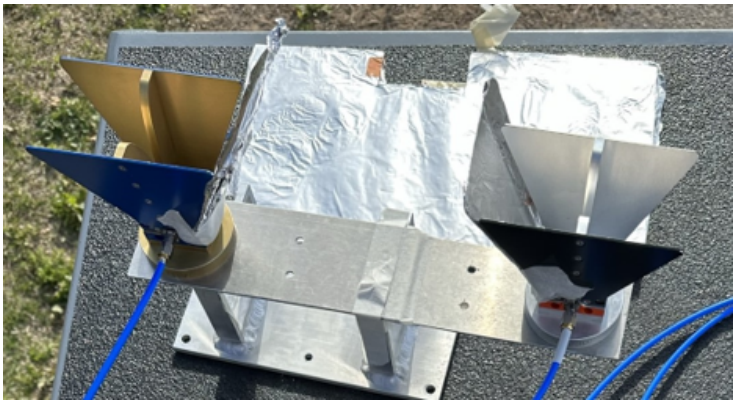

Figure 6.9: Metal baffles placed on the sides of wideband horn antennas for radar measurements

surement bandwidth. This group delay is equivalent to propagating to a scatterer at a range of 1.31 m. The system processing does not calibrate out the reference range, so instead, the peak spacing is the focus of this analysis. Looking at the relative peak spacing as the cable length is increased from 3.66 to 5.49 m, the primary peak moves 1.32 m, which is the same as the measured group delay, within measurement uncertainty.

This experiment provides confidence that the primary peak in the loopback correctly corresponds to the direct path. However, a loopback range profile ideally has no other peaks near the primary direct path. Applying a range taper should suppress these side peaks if the cause is range sidelobes or phase noise [108]. The range profiles of the two loopbacks with a Blackman-Harris window applied are shown in Fig. 6.10b. With the window applied, the side peaks are more distinct, and it is clear that the side peaks are evenly spaced on either side of the main peaks. The side peak magnitudes relative to the primary peaks are the same as the range profile without the window, indicating that there is a cause other than phase noise or range

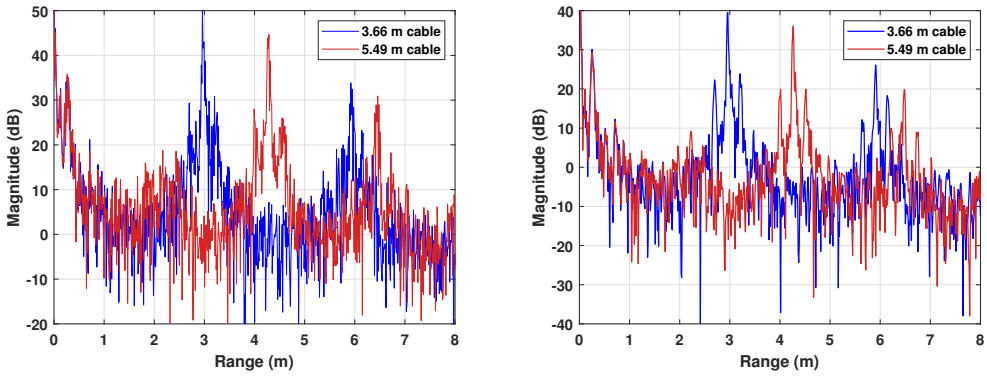

(a) No window (b) Blackman-Harris window

Figure 6.10: Loopback using two cable lengths measured with a 43.8 kHz sampling rate processed with and without windowing

sidelobes.

Upon further investigation, it has been discovered that the ADC control software sets the downsampling factor (DF) to 4 by default, so clocking the ADC to sample at 175.44 kHz would result in an effective sample rate of 43.8 ksps for Nyquist criterion purposes. The filter in this system's IF chain has a cutoff frequency of 60 kHz, so the ADC sample rate must be at least 120 ksps to avoid aliasing. Measurements are repeated with the ADC downsampling factor set to 1, for a sample rate of 175.44 ksps, and the subsequent range profile created with a Blackman-Harris window is shown in Fig. 6.12b. Now, the side peaks are gone, indicating that aliasing was the source. Note that the faster sampling fills the ADC memory more quickly. Therefore, less of the transmitted chirp is captured, and the reduced bandwidth corresponds to a coarser range resolution. In reality, the aliased range profile with DF = 4 captured the total transmitted bandwidth, while the correctly sampled range profile in Fig. 6.12b contains the 5.6 GHz bandwidth calculated previously.

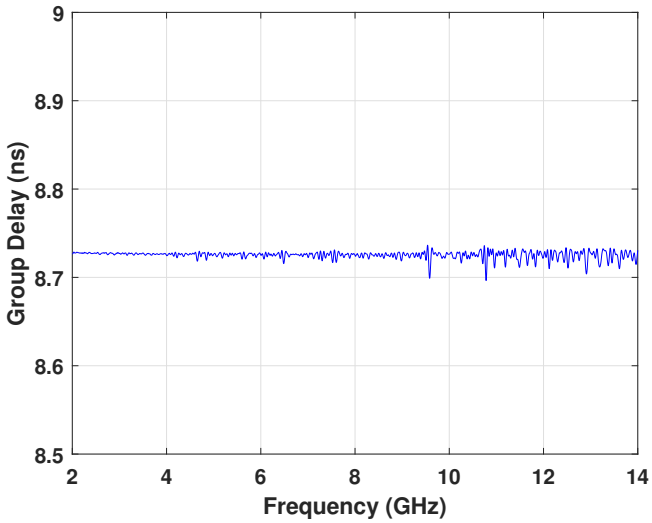

Figure 6.11: Group delay through a single 1.83 m cable

After confirming the successful loopback operation, some basic ranging is conducted to verify the radar functionality further. A metal plate is set on top of two-inch-thick foam slabs, and the antennas are mounted above the slabs and pointed down, as seen in Fig. 6.13. By altering the number of slabs, the plate can reliably be moved between ranges. The range profiles created by placing the plate on the ground and then on a varying number of slabs are shown in Fig. 6.14. The expected ranges relative to the return from the plate on the ground are plotted as dashed vertical lines. The measured plate locations align well with the calculated locations, indicating that the radar is ranging properly.

To capture more bandwidth within the ADC's limited collection time, the Windfreak signal generator is replaced by a VNA. By using the VNA's transmit port as a signal generator, the transmit frequency spacing can be maintained while covering the full 2-14 GHz bandwidth in less than the ADC's 370 ms maximum collection time. Initially, the Keysight FieldFox N9917B was selected due to its portability.

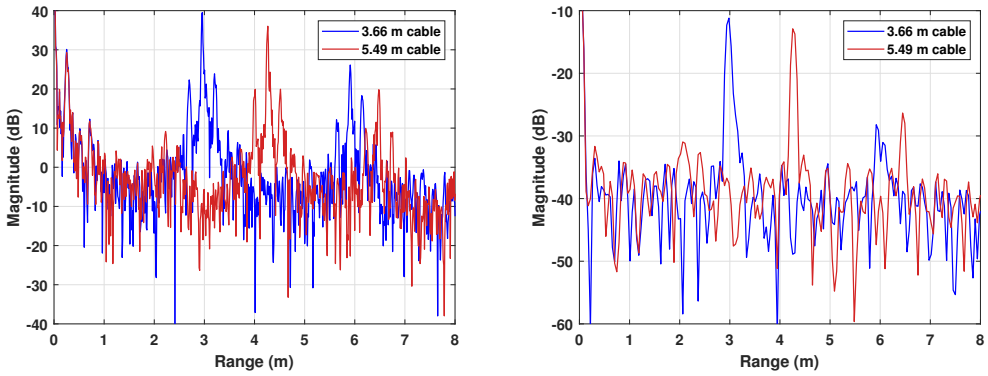

(a) 43.8 ksps (DF = 4) (b) 177.5 ksps (DF = 1)

Figure 6.12: Loopback using two cable lengths measured with a low sampling rate (a) leading to aliasing and a higher sample rate (b), Blackman Harris

However, spectral analysis revealed that the FieldFox transmitted non-trivial harmonics that negatively impacted the range profile quality. Instead, the transmitter is replaced with a benchtop Agilent PNA 5225A to reduce the transmitted harmonics. At some point during measurements, the range profile quality was degraded again, primarily with multiple peaks appearing when only a single peak was expected. Upon further investigation, the ADC capture fidelity had decreased. With the input port terminated into a 50 Ω load, the ADC collected the raw, time-domain samples shown in Fig. 6.15. While noise is expected, such as in the first 500 samples, the irregularly spaced peaks reaching almost -62 dB are not typical behavior. This performance persisted after reseating all connections within the control board.

An Agilent Infiniium DSO-80804B oscilloscope is employed to collect the measurements to replace the ADC. A microcontroller is still used to trigger the VNA and oscilloscope, and the 10 MHz reference clock from the oscilloscope is fed into the REF IN port on the VNA as opposed to using a separate crystal oscillator. For future compensation techniques that require knowledge of when the chirp begins, a

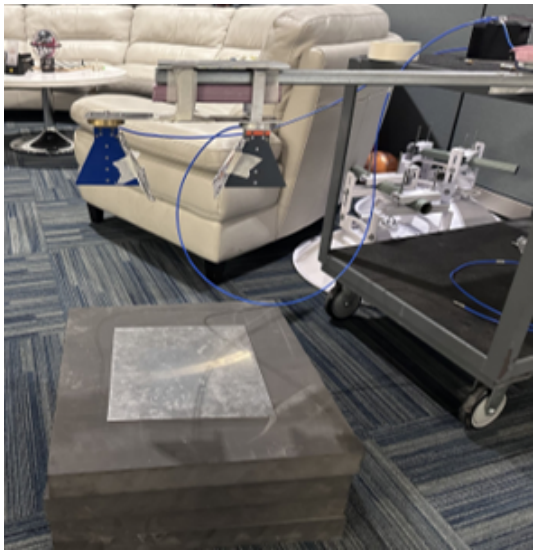

Figure 6.13: Configuration for experiment to verify radar ranging capabilities

trigger between the VNA and oscilloscope ensures that the receiver and transmitter begin operation simultaneously. The vertical and horizontal scales of the oscilloscope are adjusted to be as fine as possible while still capturing the entire chirp to maximize the capture quality, as the dynamic range depends on the vertical axis settings. The final system configuration is shown in Fig. 6.16, and the final system hardware is shown in Fig. 6.17. Table 6.2 summarizes the current system operating parameters.

Parameter	**System Value**
Frequency Range	2-14 GHz
Chirp Length	250 ms
Tx Frequency Spacing	15 MHz
Tx Power (VNA Port)	3 dBm
Tx Power (Antenna Port)	19-24 dBm
ADC sample rate	1 MHz
ADC RMS noise floor	-65 dB

Table 6.2: Final system parameters with oscilloscope functioning as the ADC

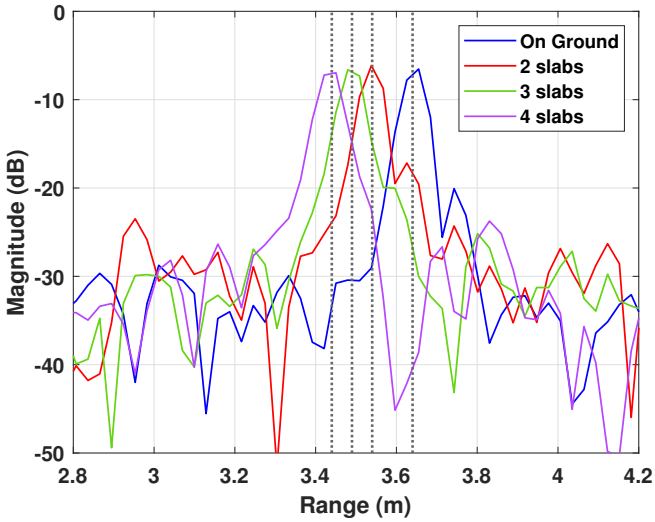

Figure 6.14: Measured range profile of metal plate elevated on varying numbers of foam slabs

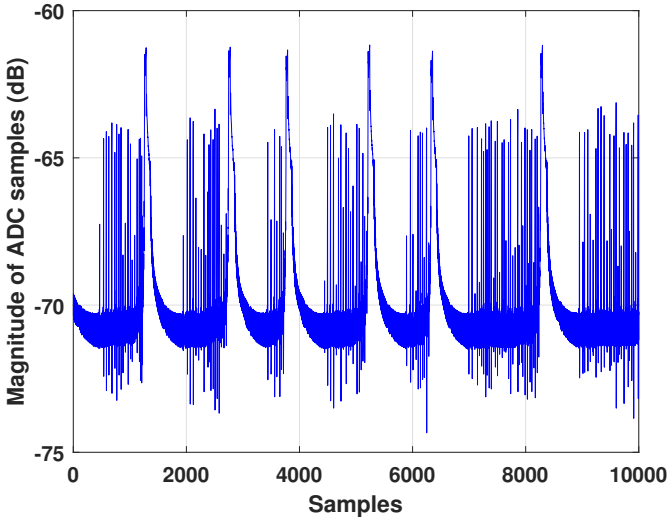

Figure 6.15: Samples from the Analog Devices DC2222A-C ADC demo board with both inputs terminated with a 50 Ω load

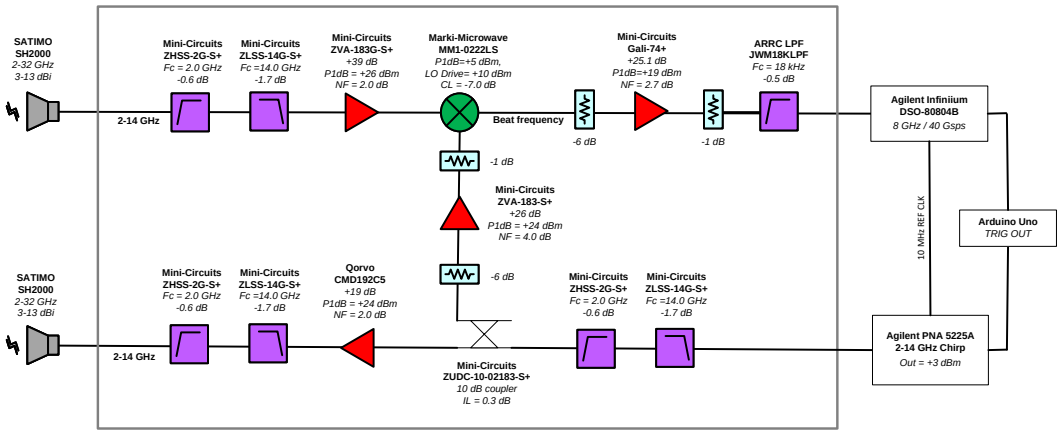

Figure 6.16: Block diagram of final FMCW radar design

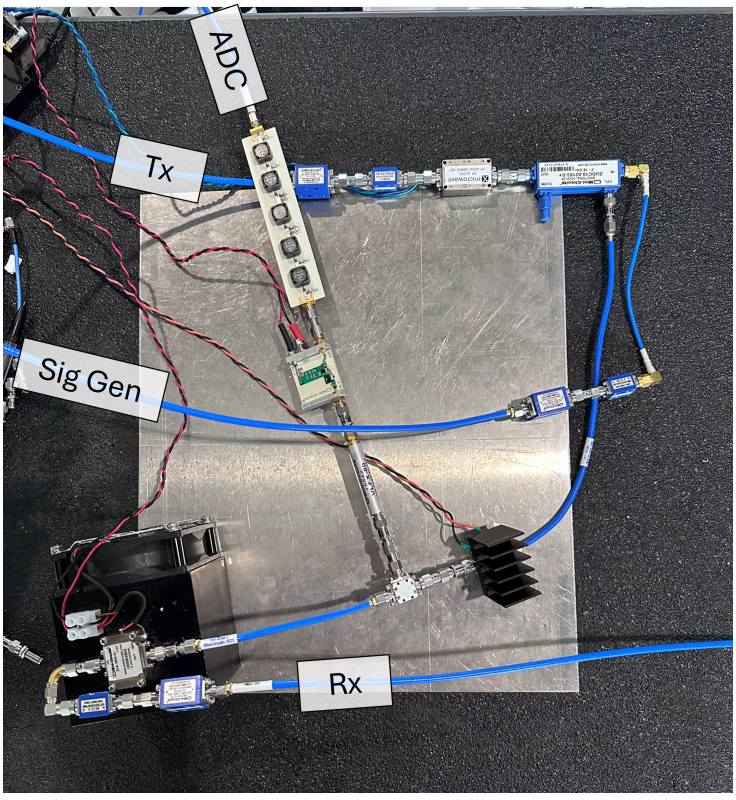

Figure 6.17: Current FMCW radar component configuration

6.3 Measurements Propagating Through Multiple Media

Now that the radar system can reliably capture an accurate range profile, the velocity of compensation techniques shown in Sections 5.1 and 5.3 can be tested in the real world. To reduce confounding variables, a relatively simple configuration is selected for initial tests. A simple geometry that can be easily replicated in simulation is desired. Furthermore, a propagation medium with low loss yields a high SNR, which will help separate the system performance from the compensation algorithm performance in initial testing.

As shown in Section 2.2, canola oil's permittivity varies slightly from 2-14 GHz while maintaining a relatively low conductivity. These electrical properties, low cost, and wide availability make canola oil a good candidate for a measurement target. A hollow 7-inch plastic cube is filled with canola oil and placed 1.2 m away from the radar's antennas, as shown in Fig. 6.18. An aluminum plate is mounted with 3D-printed brackets to sit inside the box of oil parallel to the front. The thickness of the oil layer can be adjusted by sliding the plate forward or backward within the box. In this configuration, the radar receives two main returns: the reflections from the air-oil boundary and the oil-aluminum boundary.

Even well-designed, high-performance radar systems commonly implement some post-processing to enhance the range profile quality and overcome phase and magnitude imperfections within the system. For example, placing a tapered window over the received samples is a well-known way to reduce the sidelobes inherent to the rectangular signal envelope [107]. Some radar applications implement vector background subtraction to remove unwanted scatterers [2]. To measure an object

Figure 6.18: Configuration to measure an aluminum plate placed 4-in. from the front face of canola oil-filled container

of interest, one measurement is collected with the object in the scene, and a second measurement is collected with the object removed from the scene. The scattering from the object can be isolated by taking the difference between the two scenes, which are otherwise static. This method relies on very stable phase progression within the system. An alternative to background subtraction is deconvolution. A measurement of a specular reflection is captured and then deconvolved with the measurement of interest to remove system effects such as phase imperfections [109]. For this system, the range profile is deconvolved by an element-wise division in the sample domain.

The post-processing techniques are studied with the oil box as a target, initially with no plate inside. Ideally, the range profile contains the reflection from the air-oil boundary at a range of 4 m. There is a much smaller reflection later from the

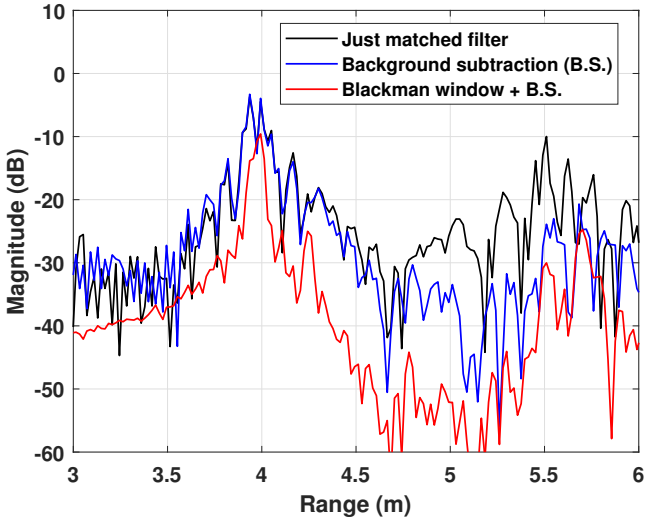

Figure 6.19: Measured range profile of the box of canola oil without a plate inside, using several post-processing improvement strategies

reflection at the back of the box. The range profile created with a matched filter and no other techniques has two peaks at the expected air-oil boundary, seen in Fig. 6.19. Performing background subtraction by subtracting off a measurement without the oil target reduces the clutter beyond the range of 4.5 m, such as reflections off the room's walls and ceiling. Applying both background subtraction and windowing improves the range profile significantly, yielding a single peak at the appropriate location for the air-oil boundary. However, the width of the shape of the main lobe is asymmetrical beyond what one would expect from typical range straddling.

The post-processing experiment is repeated with the aluminum plate placed 2 in. behind the front of the box. Two large returns are expected in this case. The matched filter output, shown in Fig. 6.20, again has more peaks than anticipated. Background subtraction similarly improves the distant clutter without reducing the distortion of the primary return. Adding the Blackman-Harris window suppresses

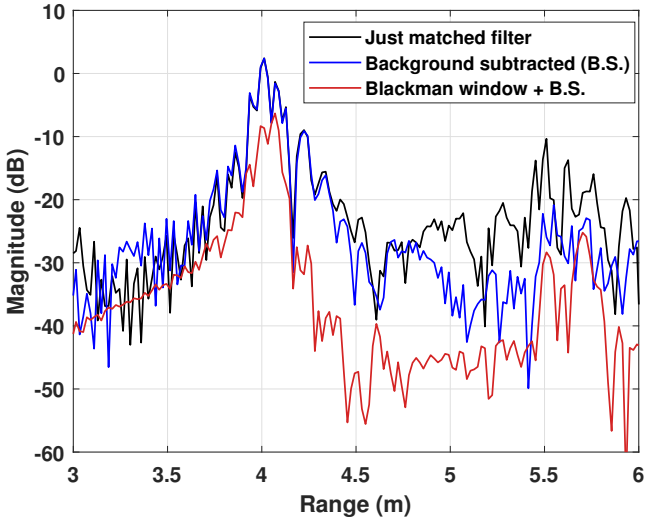

Figure 6.20: Measured range profile of the box of canola oil with an aluminum plate placed 2-in. behind the front face, using several post-processing improvement strategies

the clutter and sidelobes on either side of the main returns, but there are still not two clear peaks.

Background subtraction aims to suppress environmental effects but is unable to overcome phase and magnitude distortions from within the radar. Therefore, deconvolution is explored as an alternative. The oil box is replaced with a large box covered in aluminum foil for a measurement of a specular reflection. The same measurements used to create the range profiles in Figs. 6.19 and 6.20 are deconvolved with the aluminum box measurement and windowed with a Blackman-Harris window, and the results are shown in Fig. 6.21. The deconvolution process shifts the return ranges to appear relative to the aluminum box's return. The aluminum box is larger than the oil box, so the aluminum box's front side is closer to the radar. Thus, the single reflection at 0.21 m in the oil-only range profile is at the appro-

priate range for the air-oil reflection relative to the air-aluminum reflection. The deconvolved measurement with the plate 2-in from the box's front edge features the expected two peaks at the appropriate locations. The combination of deconvolution and windowing significantly improves the range profile quality.

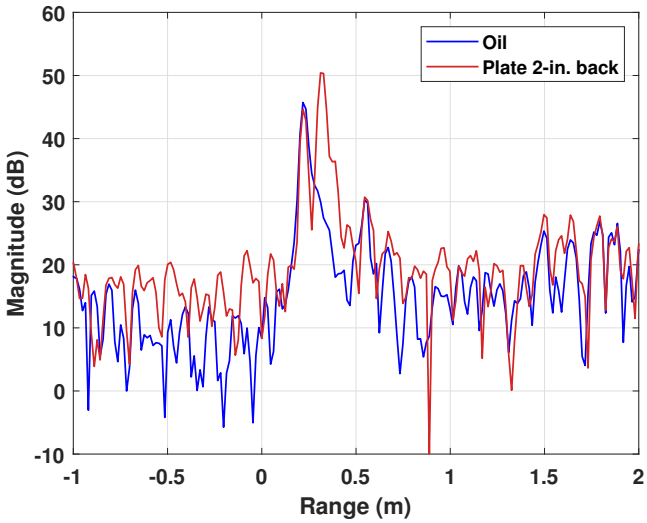

Figure 6.21: Measured range profiles after applying deconvolution and a Blackman-Harris window of an oil box, with and without a plate inside

6.3.1 Propagation Velocity Compensation

With a quality deconvolved range profile, the impact of the velocity of propagation compensation can be studied on measured results. The overall process for converting ADC samples into a range profile is summarized in Fig. 6.22. The first range profile studied is the oil box with the metal plate 4 in. from the front. The deconvolved and windowed range profile without any velocity compensation is shown by the "Uncorrected" trace in Fig. 6.23. The physical locations of the air-oil and oil-aluminum boundaries are indicated by the dashed vertical lines at 0.21

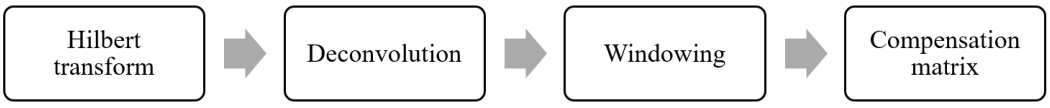

Figure 6.22: Steps to convert ADC samples into a range profile with velocity compensation

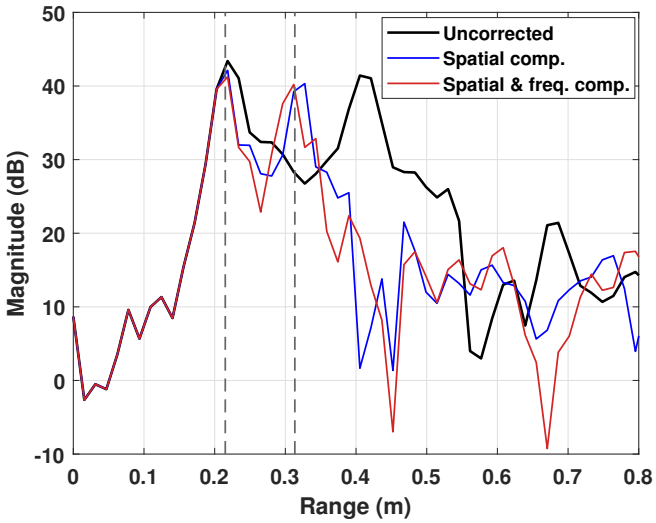

Figure 6.23: Measured range profile of a metal plate 4-in. from the front of a box of oil, without correction, with correction only across the spatial domain, and with correction across the spatial and frequency domains

and 0.31 m, respectively. The range profile expansion due to the slower velocity of propagation in the oil results in the oil-aluminum boundary return appearing farther in range than the physical reality. Additionally, the main lobe width is wider than the return from the air-oil boundary. Applying compensation along the spatial domain, as discussed in Section 5.1, shifts the return to approximately the correct location.

Because canola oil's properties do change slightly over frequency, adding the frequency-dependent compensation from Section 5.3 improves the range profile with a slight reduction in sidelobes, seen in the "Spatial & freq correction" trace of Fig. 6.23. This process is repeated with the plate 2 in. from the front of the oil, and the results are shown in Fig. 6.24. Applying the spatial and frequency-dependent velocity compensation once again moves the return's peak to the correct

location, and the main lobe narrowing is even more pronounced in this case.

To differentiate between waveform structure effects and physical system effects, the measured results are compared to a simulation of the same range profile. The simulation parameters are set to the values in Table 6.3 to mimic the physical system in range and magnitude as closely as possible. Because the simulation is implemented at the transmitted frequency to capture the wave behavior at its frequency of propagation, the data sample rate is much higher than simulations conducted at baseband. Therefore, only a 1 ms long chirp is implemented to yield a manageable data size. Because the waveform is normalized until the end of the simulation, this change can be accounted for by adjusting the time-bandwidth product pulse compression gain to match the physical system.

The simulation is configured with an aluminum plate behind a 4-in. layer of oil in order to compare to the measured results in Fig. 6.23. The white and pink noise levels within the simulation are adjusted to match the measured results as closely as possible. The uncorrected and corrected measured range profiles are compared to the corrected simulated results in Fig. 6.25. The simulated results have a "Batman ear" shape of two peaks with a plateau between them, which is similar

Parameter	**Simulated Value**
Frequency Range	2-14 GHz
Chirp Length	1 ms
Tx Frequency Spacing	10 MHz
Power	Normalized
RF sample rate	35 GHz
IF sample rate	100 kHz

Table 6.3: Radar parameters implemented in the simulation of oil and aluminum plate range profile

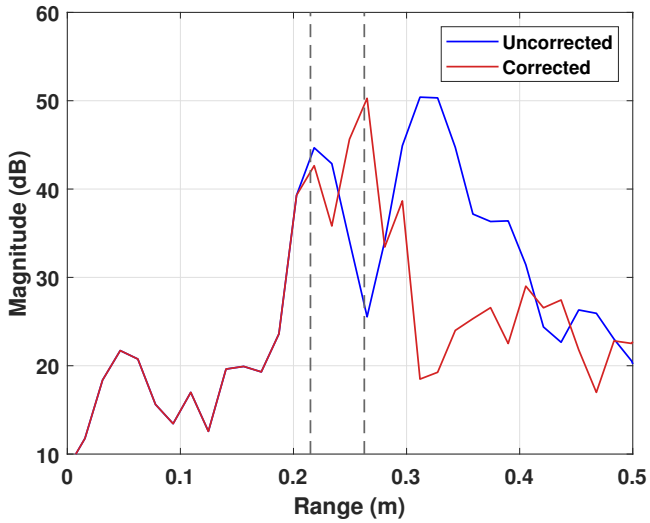

Figure 6.24: Measured range profile of a metal plate 2-in. from the front of a box of oil, without correction and with correction across the spatial and frequency domains

to the measured results. This similarity indicates that the high magnitude between the peaks in the 4-in. layer case relative to the 2-in. layer case is a consequence of the sidelobe structure and the location of the peaks within their respective range bins rather than being caused by some sort of system component issue.

For one perspective on the potential impacts of material parameter estimation error on the range profile, the simulated scene with the plate behind 2-in. of oil is studied with varying levels of velocity compensation, as shown in Fig. 6.26. A 50% correction indicates that the scale factors used are 50% between the full compensation and no compensation cases. As the peak is shifted through increasing compensation, one would expect the main lobe peak to increase in height as more power is condensed together and the matched filter is more closely suited to the received signal. However, one must also consider that the main lobe passes through

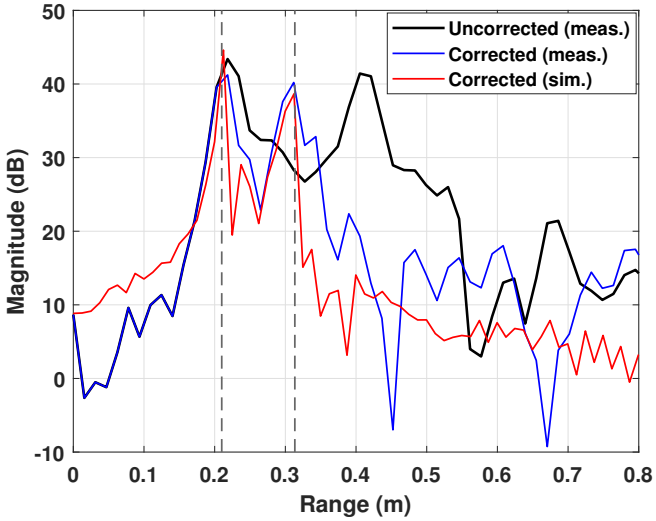

Figure 6.25: Measured range profile of a metal plate 4-in. from the front of a box of oil, with and without velocity compensation, compared to the simulated, corrected range profile

several locations within range bins, sometimes centered and other times straddling between the two. A different indicator that the compensation is having a positive impact on the range profile is the sidelobe reduction as compensation is added, reaching a minimum when the full compensation values are used.

To gain more insight into the potential consequences of incorrect material property estimates, the measured range profile is generated with oil material estimates 10% higher and 10% lower than the values extracted from the dielectric probe, similar to Fig. 5.8 that analyzed the simulation, the impact of material property estimation error is studied on the measured range profile. In the measurement case, there is not a ground truth where the material parameters fed into the compensation matrix are a 100% match to the properties encountered by the transmitted waveform. The values collected with the dielectric probe are likely close but not perfect,

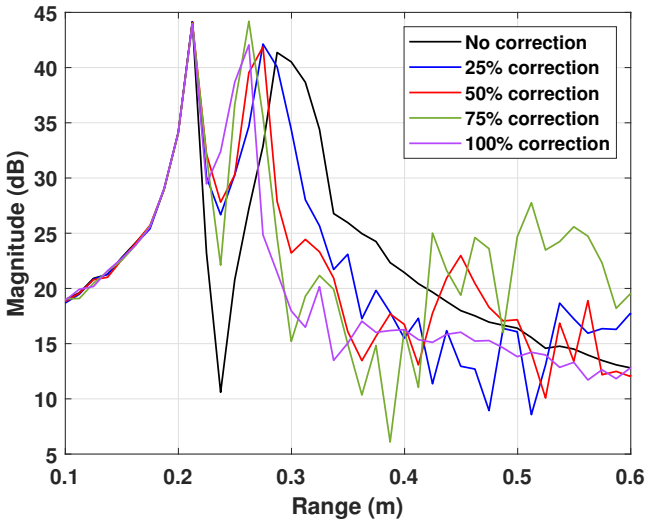

Figure 6.26: Simulated range profile of a plate behind two in. of oil with varying amounts of correction applied

with an expected permittivity error up to ± 0.1 [26]. Thus, in this case, increasing and decreasing the compensation parameters by 10% does not necessarily mean that the parameters have an error of exactly 10%. Instead, the changing parameters aim to show the impact of varying the electrical values on the output range profile.

For both the 2-in. oil thickness case in Fig. 6.27a and the 4-in. case in Fig. 6.25, the main peak shapes are similar in all variations, meaning that some variance in the estimate of material properties does not catastrophically ruin the measured range profiles. In most layered sensing applications, the relative spacing between peaks is more important than the absolute location of the peaks. For example, a snow radar computes the layer thickness relative to the air-snow interface [110]. An error along the frequency dimension changes the peak width, while an error along the spatial dimension shifts the peak location. Similar effects to spatial property mis-estimation are expected from an error in the layer thickness estimate.

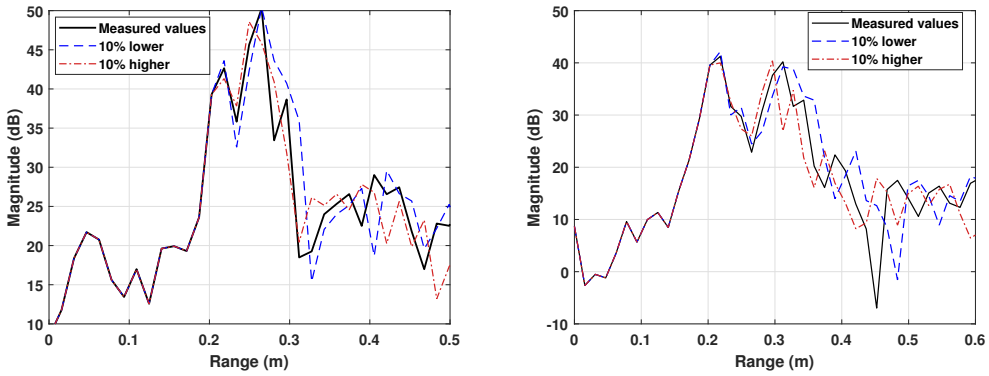

(a) 2-in. (b) 4-in.

Figure 6.27: Measured range profile of plate inside oil box with a velocity of propagation correction using the measured electrical properties as well as 10% above and below the measured values

6.3.2 Quantitative Analysis

To quantitatively describe the impact of velocity compensation, the thickness of the oil layer is analyzed for each of the range profiles. The thickness of the oil layer is calculated from the range profile as the difference between the center of the air-oil and oil-aluminum reflection peaks. It should be noted that there are several sources of error in these measurements that have nothing to do with the range processing technique. Lines are drawn on the box at 0.5-in. intervals on each side of the box, and the brackets holding the plate were visually aligned with these lines for measurement. However, the actual oil layer thickness was not re-measured each time. Furthermore, the dielectric probe has a potential measurement error of 0.1, so the material properties used for the compensation are not perfect.

The range profiles with 2-in. and 4-in thick oil layers from Figs. 6.24 and 6.25, respectively, are selected for the error analysis. The range profiles are upsampled

by increasing the number of points in the matched filter matrix to refine the beat frequency spacing and locate more specific peak values. The average errors of the thickness extracted from the range profiles relative to the designed thickness are summarized in Table 6.4. Note that one full range bin corresponds to 15.6% and 7.5% error for the 2-in. and 4-in. cases, respectively. As was seen visually before, compensating for the velocity of propagation clearly improves the accuracy of the range profile. While errors in the thickness and material property estimates fed into the compensation technique would increase the overall error, the range profile is still improved beyond the case without correction.

	No correction	Spatial & frequency correction
2 in. oil layer	120%	7.5%
4 in. oil layer	99%	9.0%

Table 6.4: Error in the measurement of oil layer's thickness calculated with range profiles with and without velocity of propagation correction

Chapter 7

Range Profile Enhancement

The traditional matched filter maximizes the output SNR after processing [104]. For a waveform with a rectangular envelope, applying the matched filter yields a sinc function with a peak sidelobe level of -13 dB [107]. However, radar systems often require much more than 13 dB of dynamic range. Thus, a smaller target may be masked by a more prominent target's sidelobes in the range profile [92]. Over the years, techniques have developed to address sidelobe levels to improve radar performance in post-processing. One of the simplest methods is applying a taper window, which has already been implemented on the measurements in Section 6.2. With a Blackman-Harris window, the sidelobes are pushed down at the expense of broadening in the main lobe [107]. Several alternatives have been developed to estimate the range profile, and the method selection depends on the properties of the range profile, whether real or complex magnitude is needed, and how much computational power is available.

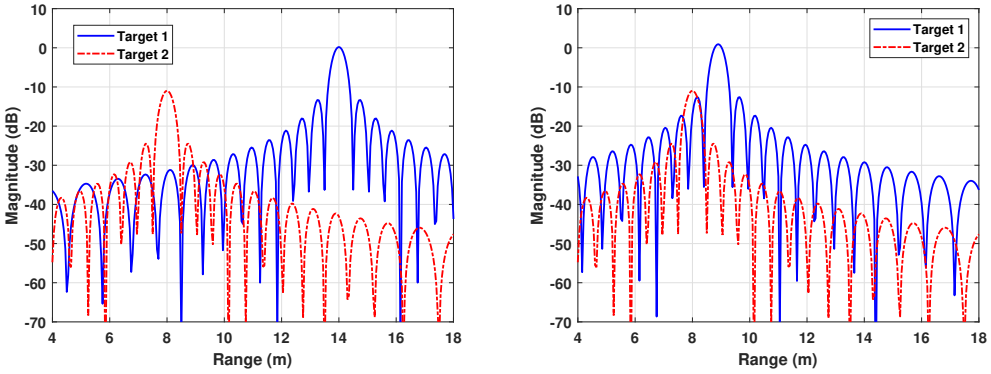

(a) Large Separation (b) Small Separation

Figure 7.1: Range profiles of two point targets with small and large separations [111]

7.1 Range Sidelobe Mitigation

To illustrate target masking, two point targets of different sizes are simulated at two separation distances. First, the individual matched filter outputs of the two targets with a significant range separation are shown in Fig. 7.1a. Next, the individual targets' matched filter outputs when the targets are closer in range are shown in Fig. 7.1b. Finally, the composite matched filter outputs when both targets are simulated together are shown in Fig. 7.2.

When the targets are well-separated in range, the peaks from both scatterers are visible. However, when the targets are closer together, it is impossible to determine where the peak of the smaller target occurs, even though the simulation's resolution is fine enough to separate the main lobes of each target's response. Thus, time-gating may not be able to separate the OUT from clutter, even if the range resolution given by (4.16) is sufficient.

Tapered windows can be applied in the frequency domain to lower range side-

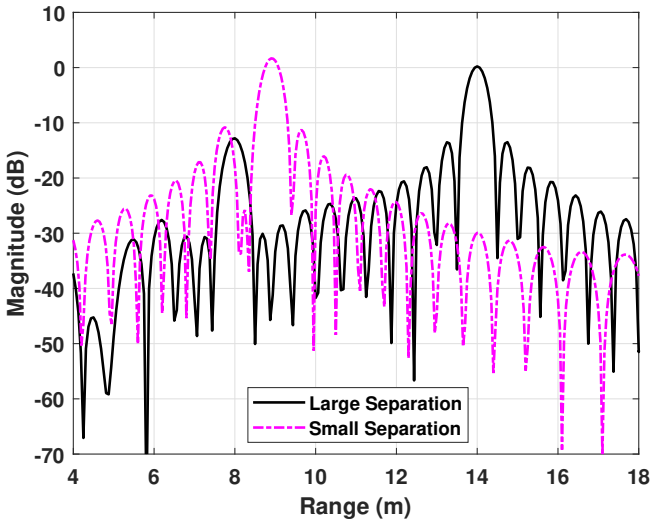

Figure 7.2: Comparison of the range profiles containing two targets with a small and a large separation

lobes at the cost of widening the main lobe [107]. However, a decrease in resolution is not always acceptable. Several other methods have been proposed to mitigate range sidelobes for radar applications. For example, the CLEAN algorithm separates targets by canceling one target at a time. However, this algorithm and its adaptations assume that each target is a point scatterer [112, 113]. This assumption is invalid for wideband high-resolution range profiles where even simple target returns, such as spheres, appear as distributed objects [114]. Therefore, the CLEAN algorithm cannot correctly reconstruct the range profile for high-resolution applications. Other sidelobe suppression methods in radar include the Yule-Walker autoregressive method and least-squares (LS) algorithms; however, these methods require a high signal-to-noise ratio (SNR) [115, 116, 117, 118]. A high SNR is not always realistic when detecting small targets or reflections from subtle changes in dielectric properties. Furthermore, LS solutions misestimate the range profile when

a significant scatterer is within the processing window before the initial range bin.

7.1.1 APC

Adaptive Pulse Compression (APC) based on Reiterative Minimum Mean-Square Error (RMMSE) estimation is a robust method to adaptively suppress sidelobes, particularly for collocated or closely spaced target scenarios [56, 119]. This Bayesian approach adaptively estimates a matched filter for each range cell based on the received signal. The filter is refined through several iterations until the noise level limits the range profile estimation accuracy [120].

The sampled version of an FMCW waveform starting at some initial frequency (f_o) with a frequency step size Δf between discrete samples can be written as

$$\mathbf{s} = \begin{bmatrix} e^{j2\pi f_0} & e^{j2\pi(f_0+\Delta f)} & \dots & e^{j2\pi(f_0+(N-1)\Delta f)} \end{bmatrix}^{\mathrm{T}} . \tag{7.1}$$

The range profile impulse response ($\mathbf{x}(\ell)$) is defined as

$$\mathbf{x}(\ell) = \begin{bmatrix} x(\ell) & x(\ell-1) & \cdots & x(\ell-N+1) \end{bmatrix}^{\mathrm{T}} \tag{7.2}$$

where ℓ is the range bin index and N is the number of samples in the transmitted waveform. The length-N demodulated receive signal ($\mathbf{y}(\ell)$) is then defined as

$$\mathbf{y}(\ell) = \mathbf{A}^{\mathrm{T}}(\ell)\mathbf{s} + \mathbf{v}(\ell) \tag{7.3}$$

where

$$\mathbf{A}(\ell) = \begin{bmatrix} x(\ell) & x(\ell+1) & \cdots & x(\ell+N-1) \\ x(\ell-1) & x(\ell) & \ddots & \vdots \\ \vdots & \ddots & \ddots & x(\ell+1) \\ x(\ell-N+1) & \cdots & x(\ell-1) & x(\ell) \end{bmatrix} \tag{7.4}$$

$$= \begin{bmatrix} \alpha_{11}e^{j2\pi f_1\tau_1} & \alpha_{12}e^{j2\pi f_1\tau_2} & \cdots & \alpha_{1L}e^{j2\pi f_1\tau_L} \\ \alpha_{21}e^{j2\pi f_2\tau_1} & \alpha_{22}e^{j2\pi f_2\tau_2} & \cdots & \alpha_{2L}e^{j2\pi f_2\tau_L} \\ \vdots & \vdots & \ddots & \vdots \\ \alpha_{N1}e^{j2\pi f_N\tau_1} & \alpha_{N2}e^{j2\pi f_N\tau_2} & \cdots & \alpha_{NL}e^{j2\pi f_N\tau_L} \end{bmatrix}. \tag{7.5}$$

is a collection of N sample-shifted snapshots of the radar impulse response, where τ_ℓ is the time delay for the signal to propagate to the ℓ^{th} range cell and return to the radar, $\alpha_{n\ell}$ is a scalar magnitude as a function of frequency n and range cell ℓ, L is the total number of range bins, and f_n is the n^{th} frequency in the transmitted waveform. The range-dependent noise vector ($\mathbf{v}(\ell)$) is defined as

$$\mathbf{v}(\ell) = \begin{bmatrix} v(\ell) & v(\ell+1) & \cdots & v(\ell+N-1) \end{bmatrix}^{\text{T}}, \tag{7.6}$$

where $v(\ell)$ is additive noise. The matched filter output ($\hat{x}_{\text{MF}}(\ell)$) is then

$$\hat{x}_{\text{MF}}(\ell) = \mathbf{s}^{\text{H}}\mathbf{y}(\ell) = \mathbf{s}^{\text{H}}\mathbf{A}^{\text{T}}(\ell)\mathbf{s} + \mathbf{s}^{\text{H}}\mathbf{v}(\ell)\ . \tag{7.7}$$

Examining (7.7) shows that any significant off-diagonal elements of $A(\ell)$ will yield range sidelobes capable of masking smaller targets when the matched filter is applied. In other words, for a given range profile index ℓ, nearby large values in $\mathbf{A}(\ell)$

affect the magnitude of $\hat{x}_{\text{MF}}(\ell)$ when added together during matrix multiplication.

The RMMSE algorithm is applied by replacing the matched filter $\mathbf{s}^{\text{H}}$ in (7.7) with a range-dependent MMSE filter ($\mathbf{w}^{\text{H}}(\ell)$). The MMSE cost function

$$J(\ell) = E\left[|x(\ell) = \mathbf{w}^{\text{H}}(\ell)\mathbf{y}(\ell)|^2\right] \tag{7.8}$$

is solved for each range bin ℓ [121]. If the range cells are uncorrelated with each other and with the noise, then the MMSE filter is given by:

$$\mathbf{w}(\ell) = \rho(\ell)(\mathbf{C}(\ell) + \mathbf{R})^{-1}\mathbf{s} \tag{7.9}$$

where

$$\rho(\ell) = |x(\ell)|^2 \tag{7.10}$$

and $\mathbf{R}$ is the $N \times N$ noise covariance matrix. With white noise, $\mathbf{R}$ is the diagonal matrix $\sigma_n^2\mathbf{I}$, where σ_n^2 is the noise variance, and $\mathbf{I}$ is the $N \times N$ identity matrix. The noise variance is estimated by separating the initial range profile estimate into short segments and finding the segment with the smallest variance. The segments are small enough that at least one of them only contains noise. The signal covariance matrix ($\mathbf{C}(\ell)$) is given by:

$$\mathbf{C}(\ell) = \sum_{n=-N+1}^{N-1} \rho(\ell + n)\mathbf{s}_n\mathbf{s}_n^{\text{H}} \,, \tag{7.11}$$

where $\mathbf{s}_n$ is created by shifting $\mathbf{s}$ by n samples and zero-filling the rest of the vector

[56]. Because $C(\ell)$ is a circulant matrix, the equation can be simplified as:

$$\mathbf{C}(\ell) = \mathbf{A} \begin{bmatrix} \rho(1) & \cdots & 0 \\ \vdots & \ddots & \vdots \\ 0 & \cdots & \rho(L) \end{bmatrix} \mathbf{A}^{\mathrm{H}} . \tag{7.12}$$

For the first iteration, the MMSE pulse compression filter is constant for all values of ℓ. For FMCW, the initial filter is just the fast Fourier transform (FFT). Estimating the power ($\rho(\ell)$), computing a new MMSE filter, and updating the range profile are repeated P times, where P is the number of iterations. For this application, the exponent on σ_n and $\rho(\ell)$ is reduced from 2 to 1.7 to prevent ill-conditioning during matrix inversion [56]. Each iteration pushes the range sidelobes down closer to the noise floor until the sidelobes cannot move any lower into the noise floor, and additional iterations do not improve the range profile estimate. Thus, P depends on the measurement's SNR.

APC is applied to the simulated small separation scenario in Fig. 7.2 to illustrate the RMMSE algorithm's impact on a range profile. The results after three iterations of the RMMSE algorithm are shown in Fig. 7.3. As can be seen, the return from the small target at 8 m is not visible with traditional matched filtering, indicating there is only one scatterer present, which is incorrect. However, both targets are revealed and easily distinguishable after applying the APC algorithm.

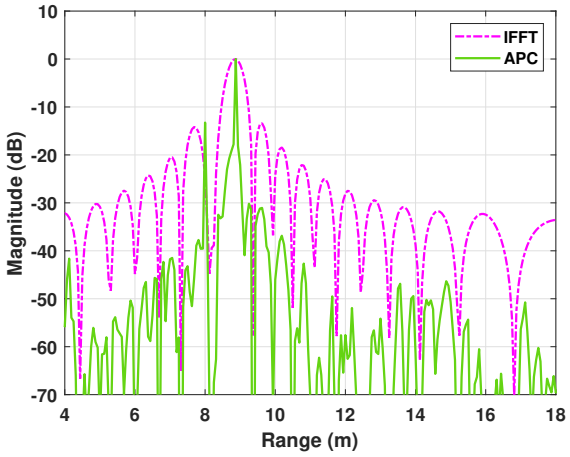

Figure 7.3: Comparison of matched filter and APC-generated range profiles of two targets with a small separation

7.1.2 RISR

The signal model in (7.7) depicts a convolutional matched filter, which is valid for the case of direct sampling a transmitted FMCW waveform. However, in the case of stretch processing, the received signal is mixed with the reference signal before being digitized. This means that the pulse compression in post-processing is no longer linear time-invariant (LTI) [122]. The transmitted signal is still convolved with the range profile, but an additional multiplication is applied during the mixing process. The structure of the received signals is represented by $\mathbf{W}$. Let $\mathbf{x}$ represent the oversampled (length N) received scattering over range and $\mathbf{u}$ represent the additive noise across the ADC sample domain (length L). Then, the received sample model is given by

$$\mathbf{y} = \mathbf{W}\mathbf{x} + \mathbf{u} \ . \tag{7.13}$$

Let the matched filter, which is the DFT from (4.15) in this case, be represented

by $\mathbf{p}$. Then the normalized signal model, $\mathbf{W}$ is

$$\mathbf{W} = \frac{\mathbf{p}}{||\mathbf{p}||_2} \ , \tag{7.14}$$

where $||\cdot||_2$ denotes an L^2 or Euclidean norm. To apply compensation for velocity of propagation, the DFT matrix is replaced with the compensatory matrix in (5.4). The spacing of the ω values is refined to match the desired oversampling to achieve a dimension of N.

Like APC, reiterative super-resolution (RISR) minimizes a mean-square error (MSE) cost function with an adaptive filter bank. For RISR, the adaptive filter bank is given by [122] to be:

$$\mathbf{W}_{\text{RISR}} = (\mathbf{WPW}^H + \mathbf{R})^{-1}\mathbf{WP} \ , \tag{7.15}$$

where

$$\mathbf{R} = E\{\mathbf{uu}^H\} = \sigma_u^2 \mathbf{I}_{L\times L} \ , \tag{7.16}$$

$$\mathbf{P} = E\{\mathbf{xx}^H\} \ , \tag{7.17}$$

and σ_u^2 is the variance of the additive noise. The previous range profile estimate, $\hat{\mathbf{x}}_{\text{RISR},i-1}$, is used in [123] to estimate $\mathbf{P}$ for iteration i as:

$$\hat{\mathbf{P}}_i = \hat{\mathbf{x}}_{\text{RISR},i-1}\hat{\mathbf{x}}^H_{\text{RISR},i-1} \odot \mathbf{I}_{N\times N} \tag{7.18}$$

where $\odot$ indicates an element-wise multiplication. The initial range profile estimate is the over-sampled matched filter output. The range profile estimate after iteration

i is given by [122] to be:

$$\hat{\mathbf{x}}_{\text{RISR},i} = \mathbf{W}_{\text{RISR},i}^{H}\mathbf{y} = \hat{\mathbf{P}}_i\mathbf{W}^H(\mathbf{W}\hat{\mathbf{P}}_i\mathbf{W}^H + \sigma_u^2\mathbf{I}_{L\times L})^{-1}\mathbf{y}\ . \tag{7.19}$$

In the case where compensation for changing velocity of propagation is necessary, then $\mathbf{W}$ is replaced with the compensation matrix in (5.4). This combination allows for the range profile conditioning to be consolidated, reducing the overall number of post-processing steps.

7.2 Application of RISR in Simulation

The parameters from the oil box measurements are replicated in the MATLAB simulator, including the materials' electrical properties, layer thicknesses, and system parameters. As seen in Fig. 6.24, the two returns can be easily differentiated in measurement when the oil layer is two inches thick. Therefore, a more challenging scenario is selected for this study. First, the plate is simulated 1-in. behind the front of the box, and the subsequent range profile is shown by the "Original" trace in Fig. 7.4. The output range profile contains only a single peak rather than two, corresponding to the air-oil and oil-aluminum reflections. Simply oversampling the range profile by refining the spacing of the frequency points in the compensation matrix does reveal two peaks at the correct locations. However, these peaks would be challenging to differentiate if more noise were present. Applying two iterations of the RISR algorithm deepens the null between the peaks and narrows the main lobes, resulting in a higher-quality range profile. Applying ten iterations of RISR yields a false peak just before the first peak with no improvement to the sidelobe

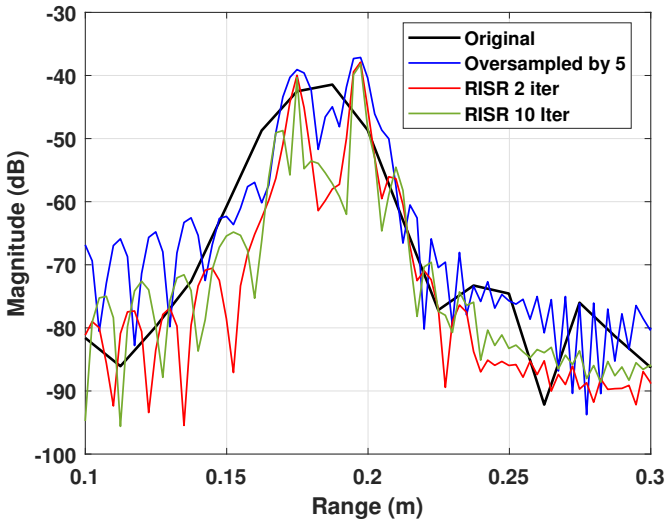

Figure 7.4: Simulated range profile of metal plate behind a 1-in. oil layer, with the application of oversampling or RISR

levels. Peak-splitting and false peaks are common challenges when working with oversampled data.

If the plate is instead only 0.5 inches from the front face, the main lobes are even more difficult to distinguish, as shown in Fig. 7.5. Even with oversampling, it is still difficult to distinguish where the two returns are located. After applying three iterations of RISR with the velocity compensation, the returns appear at the correct locations. The second peak after RISR appears lower in magnitude than the upsampled case because sidelobes from the first peak were contributing to the second main lobe in the upsampled case. RISR is also prone to mismatch loss, which could also be contributing to the magnitude reduction [124].

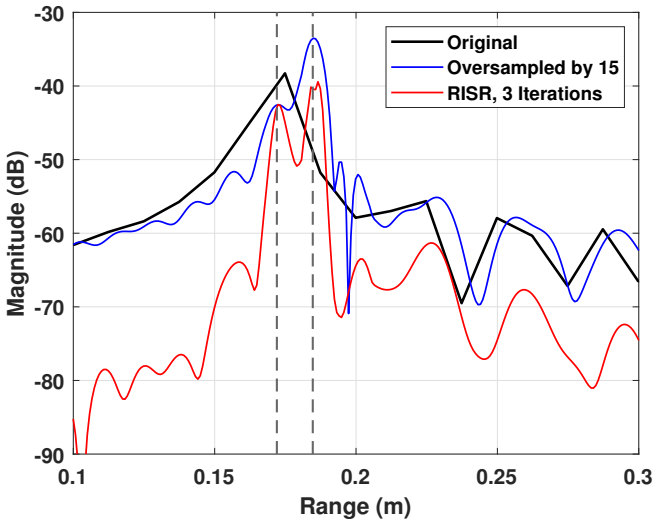

Figure 7.5: Simulated range profile of metal plate behind a 0.5-in. oil layer, with the application of oversampling or RISR

7.3 Application of RISR on Measurements

RISR works well in simulation because the received waveform is not distorted, and the noise is well-known. While a radar is designed to reduce noise as well as phase and magnitude irregularities, these imperfections still contribute to the measured results. As seen in Fig. 6.4, the measured range profile is expected to be predominantly pink noise, with some white noise also present. With only a few observations, it is challenging to generate an analytical model of the noise. Instead, the noise covariance is estimated directly from a measurement of the empty scene without a target present [124, 125]. The ADC samples of the empty scene are denoted as $\mathbf{x}_e$, and the estimate is given by

$$\hat{\sigma_u^2} = \mathbf{x}_e \mathbf{x}_e^{\mathrm{H}} \ . \tag{7.20}$$

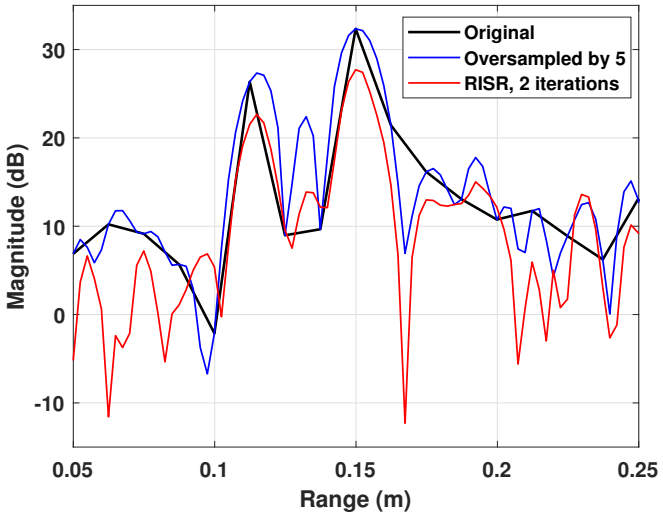

Figure 7.6: Mearued range profile of metal plate behind a 2-in. oil layer, with the application of oversampling or RISR

While this method addresses the noise estimation challenge, the signal model still fails to capture the magnitude and phase errors introduced within the system.

The impact of the real-world system behavior on RISR performance is studied by applying RISR to the measurements of the plate submerged in oil from Section 6.3. The "Original" trace in Fig. 7.6 shows the range profile created with deconvolution and velocity compensation. There are two peaks at approximately the correct locations for the air-oil and oil-aluminum boundary returns. Once oversampling is applied, an extraneous peak appears between the two returns at R = 0.13 m. After applying two iterations of RISR using the noise estimate in (7.20), the sidelobe is pushed back down.

For a more challenging scenario, RISR is applied to the measurement with only a 1-inch layer of oil, and the results are shown in Fig. 7.7. In this case, the return from the plate will be larger because the incident wave is not attenuated as much

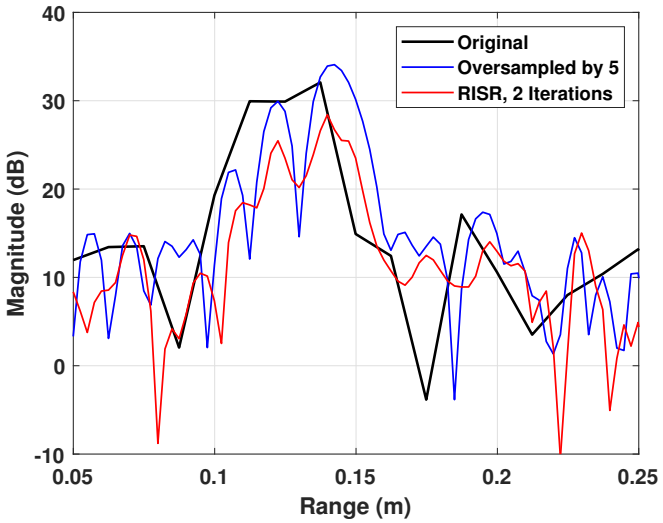

Figure 7.7: Mearued range profile of metal plate behind a 1-in. oil layer, with the application of oversampling or RISR

in the thinner oil layer. The closer proximity of the two returns also contributes to more sidelobe contamination of the peaks. The "Original" processing merges the two returns into a single, broad peak. By oversampling, the sidelobe interference with the main lobes becomes more apparent, and peaks appear at 0.106, 0.122, and 0.142 m. The expected peak locations are 0.115 and 0.137 m. Applying two iterations of RISR pushes the first peak down, though the remaining two peaks are not particularly distinct. It is possible that the box was shifted while moving the metal plate during measurements, leading to an offset in the range. If so, the two most prominent peaks after the RISR algorithm are spaced correctly. However, the shape of the range profile is still less than ideal. Refining the model could improve the results of using RISR on these measurements, as the system behavior is not fully encapsulated in the current model. Obtaining measurements with a higher SNR could also benefit the efficacy of this technique.

Chapter 8

Summary and Future Work

8.1 Summary

This work aimed to examine wave propagation through multi-media from a radar perspective to create a range profile that reflects the physical scene and unlock the potential of advanced radar tools for range profile enhancement. As radar hardware dynamic range has improved, even more applications for radar have become feasible. Small reflections from signals that have traveled deep into the ground or into a human body can now be detected, and the potential for applications like ground penetrating radar and biomedical imaging radar has been increased. As system bandwidths have increased, the impact of dispersion on range profiles has also increased, as range smearing is more likely to occur, necessitating compensation to correct this behavior.

First, the necessary electromagnetic propagation principles are presented as a foundation for later more advanced analysis. While the IT'IS foundation provides a database to reference the electrical properties of most human tissue types, many household materials' properties are only published at low frequencies or single fre-

quency points within the microwave frequency range. Thus, one must measure the materials themselves to understand the permittivity and conductivity over a wide bandwidth. Several measurement methods are presented, and several common household liquids like vinegar and oil are measured with the open-ended coaxial probe method. Then, a complete, multiple-bounce expression for boundary conditions in a thoracic cavity is derived, highlighting the importance of explicitly modeling tissue layers rather than combing them into an average material. The SAR calculated with the derived multi-path boundary conditions aligned well with a full-wave simulation.

As BIR is one of the fastest-growing applications of radar transmission through multiple media, the special considerations for illuminating biological tissue were reviewed. The commercially available medical imaging modalities led into the current developments of microwave imaging. Existing systems operate in tomographic or radar modes to target more simple tissue geometries close the body's surface. The phantoms for microwave imaging across literature have been designed to balance stability, cost, and frequency range to serve as a test bed for system prototypes. Attention was drawn to human safety, as safety requirements add another design constraint not typically present in classic radar design. To assess the power absorbed by the body as well as the power reflected back to the radar, the electrical properties of some relevant human tissues were introduced.

The radar methods to convert electromagnetic signals into information about the physical environment build upon the previous study of electromagnetic wave propagation. In particular, the trade-off space for radar design was outlined, including essential metrics like SNR and dynamic range, and several techniques to manipulate

these performances were discussed. Attention was then focused on FMCW radar and stretch processing. Stretch processing was shown to offer promising bandwidth capabilities with a relatively inexpensive prototype architecture.

To create a range profile reflecting the physical environment's dimensions when the waveform propagates through varying media, the matched filter was adapted to create a new method to correct for changes in the velocity of propagation. A MATLAB stretch processing radar simulation was built to demonstrate the new technique, initially to correct a stackup of dielectric slabs. After the compensation method was successful in the spatially varying case, one of the dielectric slabs was assigned a frequency-dependent permittivity. With traditional matched filtering, this dispersion yielded a wide main lobe from beat frequency smearing. The velocity compensation was extended to correct along both the spatial and transmitted frequency dimensions to successfully yield a range profile aligned with the physical boundaries between materials.

A prototype FMCW system was designed and assembled to operate from 2-14 GHz. After overcoming several challenges, particularly the pink noise and component compatibility challenges stemming from the very low beat frequency, successful basic ranging of a metal plate was demonstrated. The radar was then directed to a scene of a metal plate inside of an oil-filled plastic box. This configuration produced two primary reflections originating from the air-oil and oil-metal boundaries. After demonstrating the importance of deconvolution in improving the range profile quality by suppressing system imperfections, velocity compensation is applied to the measured data. Without compensation, the second return from behind the layer of oil appeared much farther in range than the physical reality. As

oil is only slightly dispersive, compensating through only the spatial domain significantly improves the alignment of the range profile. By applying compensation across space and frequency, the difference between the measured oil layer thickness compared to the physical thickness was less than 10%. Without compensation, the error was more than 99%.

When two scatterers are close together, one peak can be hidden in the other peak's sidelobes. APC and RISR algorithms were introduced as range-adaptive filtering techniques to reduce sidelobes, and the RISR technique was successfully applied to the FMCW simulation to suppress the sidelobes between peaks. Applying RISR to measurements was more challenging due to system behavior not captured by the model.

In conclusion, this work provides a comprehensive approach to radar captures through multi-media, from both an electromagnetics and radar perspective to enable the application of advanced radar enhancement techniques. The proposed correction technique significantly improves the range profile in both simulation and measurement.

8.2 Contributions

- First-time derivation of an FMCW matched filter that compensates for changing velocity of propagation across both space and frequency
- First time demonstration of two-dimensional velocity compensation in measurement
- First-time derivation of adaptive sidelobe suppression scheme for propagation

through multiple media

– First-time derivation of adaptive sidelobe suppression scheme with compensation for a velocity of propagation outside of free-space

– Analytical study of multi-path within realistic tissue layers to aid in simulation or calculation configuration

8.3 Future Work

This dissertation has begun to bridge the gap between radar and biomedical considerations to pave the way to a more robust BIR design. The human body's complex geometry does not always behave as the one-dimensional stack-up used in this analysis. The velocity of compensation matrix will need to be extended to match an application's dimensionality. For example, to construct a 3-D image of the body, the matrix must capture the velocity's variance across all three dimensions while maintaining the frequency-varying dimension. Future work will look into the tuning of the compensation to correct errors in the initial stackup estimate, both in thicknesses and electrical properties. The impact of multi-media propagation on Doppler will need to be explored in order to eventually generate radar images.

Demonstrating the power of the velocity compensation technique and evidence of its applicability to BIR would benefit from measuring more complex scenes. Thinner layers, more dispersive materials, and variance across more dimensions would showcase the technique's robustness. A non-human biological material, such as chicken breast, is also a good candidate for the near-future measurements. To carry out these measurements, system adjustments would be helpful to improve the

range profile quality. A signal generator designed with FMCW in mind, including a faster chirp rate and excellent harmonic filtering, would reduce the unwanted signals in the output. Packaging the system components more intentionally to avoid long cables and cross-talk would reduce phase distortion and improve system portability.

Tissue layers are often very close together with a significant disparity in their reflection magnitudes. Thus, the sidelobe suppression in Chapter 7 must be further explored to differentiate between closely-spaced scatterers. The improvements to the radar hardware may inherently improve RISR's performance. A faster chirp rate could increase the beat frequency into a white-noise dominant frequency band. In this case, common radar techniques like coherent averaging could be employed to improve the SNR, yielding a higher quality range profile. However, it is also possible that a more accurate signal model must be derived or other range estimation techniques must be considered.

References

[1] M. A. Richards, *Fundamentals of Radar Signal Processing*. McGraw-Hill Professional, 2005.

[2] E. F. Knott, *Radar cross section measurements*. Raleigh, NC: SciTech Pub., 2006.

[3] C. Balanis, *Advanced Engineering Electromagnetics, 2nd Ed.* Wiley, 2012.

[4] C. Gabriel, "Compilation of the dielectric properties of body tissues at RF and microwave frequencies." 1996.

[5] S. Kodera, J. Gomez Tames, and A. Hirata, "Temperature elevation in the human brain and skin with thermoregulation during exposure to RF energy," *BioMedical Engineering OnLine*, vol. 17, 01 2018.

[6] D. J. Panagopoulos, O. Johansson, and G. L. Carlo, "Evaluation of specific absorption rate as a dosimetric quantity for electromagnetic fields bioeffects," *PLOS ONE*, vol. 8, no. 6, pp. 1–9, 06 2013. [Online]. Available: https://doi.org/10.1371/journal.pone.0062663

[7] International Commission on Non-Ionizing Radiation Protection, "Guidelines for limiting exposure to time-varying electric, magnetic, and electromagnetic fields (up to 300 GHz)," *Health Physics*, vol. 118, no. 5, pp. 483–524, Mar. 2020.

[8] J.-B. Yan, D. Gomez-Garcia Alvestegui, J. W. McDaniel, Y. Li, S. Gogineni, F. Rodriguez-Morales, J. Brozena, and C. J. Leuschen, "Ultrawideband FMCW radar for airborne measurements of snow over sea ice and land," *IEEE Trans. on Geoscience and Remote Sensing*, vol. 55, no. 2, pp. 834–843, 2017.

[9] D. O'Loughlin, M. O'Halloran, B. M. Moloney, M. Glavin, E. Jones, and M. A. Elahi, "Microwave breast imaging: Clinical advances and remaining

challenges," *IEEE Transactions on Biomedical Engineering*, vol. 65, no. 11, pp. 2580–2590, 2018.

[10] R. Chandra, H. Zhou, I. Balasingham, and R. M. Narayanan, "On the opportunities and challenges in microwave medical sensing and imaging," *IEEE Trans. Biomed. Eng*, vol. 62, no. 7, pp. 1667–1682, 2015.

[11] A. E.-C. Tan, J. McCulloch, W. Rack, I. Platt, and I. Woodhead, "Radar measurements of snow depth over sea ice on an unmanned aerial vehicle," *IEEE Transactions on Geoscience and Remote Sensing*, vol. 59, no. 3, pp. 1868–1875, 2021.

[12] J.-B. Yan, D. Gomez-García Alvestegui, J. W. McDaniel, Y. Li, S. Gogineni, F. Rodriguez-Morales, J. Brozena, and C. J. Leuschen, "Ultrawideband FMCW radar for airborne measurements of snow over sea ice and land," *IEEE Transactions on Geoscience and Remote Sensing*, vol. 55, no. 2, pp. 834–843, 2017.

[13] J. Zhang, F. Li, and G. Yang, "Ray-based simulations of received signals from ground penetrating radar," in *2006 CIE International Conference on Radar*, 2006, pp. 1–4.

[14] M. Ardekani, P. Druyts, S. Lambot, A. De Coster, and X. Neyt, "Recovering the structure of a layered soil, including layer thickness and dielectric permittivity, using the interfaces and objects backscatter detected in GPR B-scans," in *Proceedings of the 15th International Conference on Ground Penetrating Radar*, 2014, pp. 397–400.

[15] T. Reimer, M. S. Nepote, and S. Pistorius, "Initial results using an MLEM-based reconstruction algorithm for breast microwave radar imaging," in *2018 18th International Symposium on Antenna Technology and Applied Electromagnetics (ANTEM)*, 2018, pp. 1–2.

[16] T. Varslot, J. H. Morales, and M. Cheney, "Synthetic-aperture radar imaging through dispersive media," *Inverse Problems*, vol. 26, 2010.

[17] Keysight Technologies, "Basics of measuring the dielectric properties of materials," Application Note 5989-2589EN, 8 2020.

[18] C. A. Nieves and M. T. Lanagan, "Exploring the dielectric polarization and ionic conduction mechanisms in sodium-containing silicate and borosilicate glasses," *Journal of Non-Crystalline Solids*, vol. 617, p. 122505,

2023. [Online]. Available: https://www.sciencedirect.com/science/article/pii/S002230932300371X

[19] K. S. Cole and R. H. Cole, "Dispersion and absorption in dielectrics i. alternating current characteristics," *The Journal of chemical physics*, vol. 9, no. 4, pp. 341–351, 1941.

[20] S. Cruciani, V. D. Santis, M. Feliziani, and F. Maradei, "Cole-Cole vs Debye models for the assessment of electromagnetic fields inside biological tissues produced by wideband EMF sources," in *2012 Asia-Pacific Symposium on Electromagnetic Compatibility*, 2012, pp. 685–688.

[21] R. Zoughi and B. Zonnefeld, "Permittivity characteristics of kevlar, carbon composites, E-glass, and rubber (33% carbon) at X-band (8–12 ghz)," 1991.

[22] D. Ghodgaonkar, V. Varadan, and V. Varadan, "A free-space method for measurement of dielectric constants and loss tangents at microwave frequencies," *IEEE Transactions on Instrumentation and Measurement*, vol. 38, no. 3, pp. 789–793, 1989.

[23] A. M. Mohammed, A. Hart, J. Wood, Y. Wang, and M. J. Lancaster, "3d printed re-entrant cavity resonator for complex permittivity measurement of crude oils," *Sensors and Actuators A: Physical*, vol. 317, p. 112477, 2021. [Online]. Available: https://www.sciencedirect.com/science/article/pii/S0924424720317921

[24] P. Bernard and J. Gautray, "Measurement of dielectric constant using a microstrip ring resonator," *IEEE Transactions on Microwave Theory and Techniques*, vol. 39, no. 3, pp. 592–595, 1991.

[25] Rohde & Schwarz, "Measurement of dielectric material properties," Application Note RAC0607-0019-1-4E, 4 2012.

[26] *N1501A Dielectric Probe Kit*, Keysight Technologies, 5 2020.

[27] U. Kaatze, "Complex permittivity of water as a function of frequency and temperature," *Journal of Chemical & Engineering Data*, vol. 34, no. 4, pp. 371–374, 1989. [Online]. Available: https://doi.org/10.1021/je00058a001

[28] N. Pavlov and Y. Baloshin, "Electromagnetic properties of water on GHz frequencies for medicine tasks and metamaterial applications," in *Journal of Physics: Conference Series*, vol. 643, no. 1. IOP Publishing, 2015, p. 012047.

[29] A. El-Damak, S. Thorson, and E. Fear, "Study of the dielectric properties of artificial sweat mixtures at microwave frequencies," *Biosensors*, vol. 10, p. 62, 06 2020.

[30] S. I. Latif, D. Flores Tapia, D. Rodriguez Herrera, M. Solis Nepote, S. Pistorius, L. Shafai *et al.*, "A directional antenna in a matching liquid for microwave radar imaging," *International Journal of Antennas and Propagation*, vol. 2015, 2015.

[31] J. Vrba and D. Vrba, "Temperature and frequency dependent empirical models of dielectric properties of sunflower and olive oil," *Radioengineering*, vol. 22, no. 4, pp. 1281–1287, 2013.

[32] L. M. Brekhovskikh, *Waves in Layered Media*. Academic Press, 1960.

[33] M. Cavagnaro, E. Pittella, and S. Pisa, "UWB pulse propagation into human tissues," *Physics in Medicine and Biology*, vol. 58, no. 24, pp. 8689–8707, Nov 2013.

[34] J. G. Metcalf, J. McDaniel, J. Ruyle, N. Goodman, and J. C. Borders, "An examination of frequency-modulated continuous wave radar for biomedical imaging," in *2020 IEEE Int. Radar Conf. (RADAR)*, April 2020, pp. 996–1001.

[35] K. Shiba, T. Nagato, T. Tsuji, and K. Koshiji, "Analysis of specific absorption rate and current density in an energy transmission system for a wireless capsule endoscope," in *2007 29th Annual Int. Conf. of the IEEE Engineering in Medicine and Biology Society*, 2007, pp. 6051–6054.

[36] R. E. Jarvis and J. W. McDaniel, "Impact of multi-path wave propagation on specific absorption rate in layered dielectrics," in *2024 IEEE Wireless and Microwave Technology Conference (WAMICON)*. IEEE, 2024, pp. 1–4.

[37] A. Christ et al., "The virtual family—development of surface-based anatomical models of two adults and two children for dosimetric simulations," *Physics in Medicine and Biology*, vol. 55, no. 2, pp. N23–N38, Dec 2009.

[38] J. Grund, K.-U. Rathjen, C. Rädel, M. Stiemer, and S. Dickmann, "Planar multilayer model of human tissue exposed to a plane electromagnetic wave," *IEEE Journal of Electromagnetics, RF and Microwaves in Medicine and Biology*, vol. 5, no. 4, pp. 305–312, 2021.

[39] A. Macovski, *Medical imaging systems*, ser. Prentice-Hall information and system sciences series. Englewood Cliffs, N.J.: Prentice-Hall, 1983.

[40] J. D. Mathews, A. V. Forsythe, Z. Brady, M. W. Butler, S. K. Goergen, G. B. Byrnes, G. G. Giles, A. B. Wallace, P. R. Anderson, T. A. Guiver, P. McGale, T. M. Cain, J. G. Dowty, A. C. Bickerstaffe, and S. C. Darby, "Cancer risk in 680 000 people exposed to computed tomography scans in childhood or adolescence: data linkage study of 11 million Australians," *BMJ*, vol. 346, 2013. [Online]. Available: https://www.bmj.com/content/346/bmj.f2360

[41] S. Servaes, G. Khanna, A. Naranjo, J. I. Geller, P. F. Ehrlich, K. W. Gow, E. J. Perlman, J. S. Dome, E. Gratias, and E. A. Mullen, "Comparison of diagnostic performance of ct and mri for abdominal staging of pediatric renal tumors: a report from the children's oncology group," *Pediatric radiology*, vol. 45, pp. 166–172, 2015.

[42] A. Ignee, N. S. Atkinson, G. Schuessler, and C. F. Dietrich, "Ultrasound contrast agents," *Endoscopic ultrasound*, vol. 5, no. 6, p. 355, 2016.

[43] J. Wahsner, E. M. Gale, A. Rodríguez-Rodríguez, and P. Caravan, "Chemistry of mri contrast agents: current challenges and new frontiers," *Chemical reviews*, vol. 119, no. 2, pp. 957–1057, 2018.

[44] A. Fasoula, B. Moloney, L. Duchesne, J. G. Cano, B. Oliveira, J.-G. Bernard, and M. Kerin, "Super-resolution radar imaging for breast cancer detection with microwaves: the integrated information selection criteria," in *2019 41st Annual International Conference of the IEEE Engineering in Medicine and Biology Society (EMBC)*, 2019, pp. 1868–1874.

[45] Y. Cheng and M. Fu, "Dielectric properties for non-invasive detection of normal, benign, and malignant breast tissues using microwave theories," *Thoracic Cancer*, vol. 9, no. 4, pp. 459–465, 2018. [Online]. Available: https://onlinelibrary.wiley.com/doi/abs/10.1111/1759-7714.12605

[46] D. Byrne, M. Sarafianou, and I. J. Craddock, "Compound radar approach for breast imaging," *IEEE Transactions on Biomedical Engineering*, vol. 64, no. 1, pp. 40–51, 2017.

[47] K. Smith, J. Bourqui, D. Garrett, S. Zarnke, M. Owjimehr, D. Deutscher, T. Fung, and E. Fear, "Microwave imaging of the breast: Consistency of measurements over time," *IEEE Journal of Electromagnetics, RF and Microwaves in Medicine and Biology*, vol. 6, no. 1, pp. 61–67, 2022.

[48] E. Fear, X. Li, S. Hagness, and M. Stuchly, "Confocal microwave imaging for breast cancer detection: localization of tumors in three dimensions," *IEEE Transactions on Biomedical Engineering*, vol. 49, no. 8, pp. 812–822, 2002.

[49] M. Solis-Nepote, T. Reimer, and S. Pistorius, "An air-operated bistatic system for breast microwave radar imaging: Pre-clinical validation," in *2019 41st Annual International Conference of the IEEE Engineering in Medicine and Biology Society (EMBC)*, 2019, pp. 1859–1862.

[50] T. Reimer and S. Pistorius, "An optimization-based approach to radar image reconstruction in breast microwave sensing," *Sensors*, vol. 21, no. 24, 2021. [Online]. Available: https://www.mdpi.com/1424-8220/21/24/8172

[51] M. Wang, R. Scapaticci, S. Abedi, H. Roussel, N. Joachimowicz, S. Costanzo, M. Cavagnaro, and L. Crocco, "A microwave imaging system prototype for liver ablation monitoring: Design and initial experimental validation," in *2022 International Workshop on Antenna Technology (iWAT)*, 2022, pp. 207–209.

[52] Y. Chen, I. J. Craddock, and P. Kosmas, "Feasibility study of lesion classification via contrast-agent-aided UWB breast imaging," *IEEE Transactions on Biomedical Engineering*, vol. 57, no. 5, pp. 1003–1007, 2010.

[53] M. Klemm, J. Leendertz, D. Gibbins, I. Craddock, A. Preece, and R. Benjamin, "Towards contrast enhanced breast imaging using ultra-wideband microwave radar system," in *2010 IEEE Radio and Wireless Symposium (RWS)*, 2010, pp. 516–519.

[54] Y. Chen, P. Kosmas, and S. Martel, "Microwave breast tumor detection and size estimation using contrast-agent-loaded magnetotactic bacteria," in *2013 35th Annual International Conference of the IEEE Engineering in Medicine and Biology Society (EMBC)*, 2013, pp. 5481–5484.

[55] A. Fasoula, L. Duchesne, B. Moloney, J. Gil Cano, C. Chenot, B. Oliveira, J.-G. Bernard, S. Abd Elwahab, and M. Kerin, "Pilot patient study with the wavelia microwave breast imaging system for breast cancer detection: Clinical feasibility and identified technical challenges," in *2020 14th European Conference on Antennas and Propagation (EuCAP)*, 2020, pp. 1–5.

[56] S. Blunt and K. Gerlach, "Adaptive pulse compression," in *Proceedings of the 2004 IEEE Radar Conference (IEEE Cat. No.04CH37509)*, 2004, pp. 271–276.

[57] "Stable and lifelong head phantoms using polymer composition mimicking materials to test electromagnetic medical imaging systems," *IEEE Journal of Electromagnetics, RF and Microwaves in Medicine and Biology*, vol. 5, pp. 322–328, 12 2021.

[58] J. Moll, D. Wcõrtge, V. Krozer, A. Santorelli, M. Popović, B. Bazrafshan, F. Hübner, T. J. Vogl, and N. Nikolova, "Quality control of carbon-rubber tissue phantoms: Comparative MRI, CT, X-ray and UWB microwave measurements," 3 2017, pp. 2723–2727.

[59] K. S. Sultan, B. Mohammed, P. C. Mills, and A. Abbosh, "Anthropomorphic durable realistic knee phantom for testing electromagnetic imaging systems," *IEEE Journal of Electromagnetics, RF and Microwaves in Medicine and Biology*, vol. 5, no. 2, pp. 132–138, 2021.

[60] A. V. Dem'Yanenko, Y. V. Nevstruev, D. E. Titova, and I. V. Semernik, "Fabrication of three-dimensional human chest phantom for investigation of the propagation of electromagnetic waves of the microwave range," *Proceedings of the 2021 IEEE Conference of Russian Young Researchers in Electrical and Electronic Engineering, ElConRus 2021*, pp. 1726–1731, 1 2021.

[61] L. Kranold, J. Boparai, L. Fortaleza, and M. Popovic, "Skin phantoms for microwave breast cancer detection: A comparative study," *IEEE Journal of Electromagnetics, RF and Microwaves in Medicine and Biology*, p. 1, 2021.

[62] B. McDermott, E. Porter, M. O'Halloran, A. Poudel, M. Biggs, N. S. Karode, and A. B. Coffey, "3D printable solid tissue-mimicking material for microwave phantoms," 9 2018, pp. 1–2.

[63] E. Fernandez-Aranzamendi, E. San-Román, P. Castillo-Araníbar, Luz-Ventura, V. González-Posadas, and D. Segovia-Vargas, "Breast tumor classification by age and size based on analysis of dielectric properties performed on in vivo and ex vivo measurements," in *2022 International Workshop on Antenna Technology (iWAT)*, 2022, pp. 192–195.

[64] L. Farina, G. Ruvio, R. Pinto, L. Vannucci, M. Cavagnaro, and V. Lopresto, "Development of a portable setup suitable for in vivo measurement of the dielectric properties of biological tissues," in *2017 11th European Conference on Antennas and Propagation (EUCAP)*, 2017, pp. 2732–2736.

[65] D. C. Garrett and E. C. Fear, "Feasibility study of hydration monitoring using microwaves–part 1: A model of microwave property changes with dehydra-

tion," *IEEE Journal of Electromagnetics, RF and Microwaves in Medicine and Biology*, vol. 3, no. 4, pp. 292–299, 2019.

[66] I. Farhat, L. Farrugia, D.-A. Pollacco, J. Bonello, and C. V. Sammut, "Wideband modelling of the dielectric properties of muscle as a function of hydration," in *2019 International Conference on Electromagnetics in Advanced Applications (ICEAA)*, 2019, pp. 606–609.

[67] L. Fortaleza and M. Popović, "Narrowband microwave breast screening: Repeatability study with phantoms," *IEEE Journal of Electromagnetics, RF and Microwaves in Medicine and Biology*, vol. 6, no. 2, pp. 260–266, 2022.

[68] S. Kumari and S. Raghavan, "Biological effects of microwave," in *International Conference on Information Communication and Embedded Systems (ICICES2014)*, 2014, pp. 1–6.

[69] M. Hampe, "Specific absorption rate in human tissues: Accurate and approximated values," in *2013 Int. Symp. on Electromagnetic Compatibility*, Sep. 2013, pp. 143–148.

[70] R. E. Jarvis, J. G. Metcalf, and J. W. McDaniel, "The impact of electromagnetic radation regulations on biomedical radar applications (under review)," *IEEE Journal of Electromagnetics, RF and Microwaves in Medicine and Biology*, 2023.

[71] "IEC/IEEE international standard – determining the peak spatial-average specific absorption rate (SAR) in the human body from wireless communications devices, 30 MHz to 6 GHz - part 1: General requirements for using the finite-difference time-domain (FDTD) method for SAR calculations," *IEC/IEEE 62704-1:2017*, pp. 1–86, 2017.

[72] R. A. Taylor, S. Gogineni, S. Gurbuz, S. Kolpuke, L. Li, C. O'Neill, J.-B. Yan, T. Akins, J. Carswell, D. Braaten, S. Tsutaki, A. Abe-Ouchi, S. Fujita, K. Kawamura, B. V. Liefferinge, and K. Matsuoka, "A prototype ultrawideband FMCW radar for snow and soil-moisture measurements," in *2019 IEEE Int. Geoscience and Remote Sensing Symp. (IGARSS)*, 2019, pp. 3974–3977.

[73] N. Galin, A. Worby, R. Massom, G. Brooker, C. Leuschen, S. Gogineni, and P. Jansen, "2-8 GHz FMCW radar for estimating snow depth on antarctic sea ice," in *2008 Int. Conf. on Radar*, 2008, pp. 276–281.

[74] M. Hussain, "Antenna patterns of nonsinusoidal waves with the time variation of a Gaussian pulse," *IEEE Transactions on Electromagnetic Compatibility*, vol. 30, no. 4, pp. 504–512, 1988.

[75] E. M. Staderini, "Everything you always wanted to know about UWB radar: a practical introduction to the ultra wideband technology," in *Online Symposium for Electronics Engineers*, 2016.

[76] R. Feghhi, D. Oloumi, and K. Rambabu, "Design and development of an inexpensive sub-nanosecond Gaussian pulse transmitter," *IEEE Trans. on Microw. Theory and Techniques*, vol. 67, no. 9, pp. 3773–3782, 2019.

[77] G. Varotto and E. M. Staderini, "On the UWB medical radars working principles," *Int. J. Ultra Wideband Commun. Syst.*, vol. 2, pp. 83–93, 2011.

[78] K. Rambabu, A. E.-C. Tan, K. K.-M. Chan, and M. Y.-W. Chia, "Estimation of antenna effect on ultra-wideband pulse shape in transmission and reception," *IEEE Transactions on Electromagnetic Compatibility*, vol. 51, no. 3, pp. 604–610, 2009.

[79] D. Oloumi, R. S. C. Winter, A. Kordzadeh, P. Boulanger, and K. Rambabu, "Microwave imaging of breast tumor using time-domain UWB circular-SAR technique," *IEEE Trans. on Medical Imaging*, vol. 39, no. 4, pp. 934–943, 2020.

[80] R. Feghhi, R. S. C. Winter, F. M. Sabzevari, and K. Rambabu, "Design of a low-cost UWB time-domain radar system for subcentimeter image resolution," *IEEE Trans. on Microwave Theory and Techniques*, vol. 70, no. 7, pp. 3617–3628, 2022.

[81] T. Kikkawa, Y. Masui, A. Toya, H. Ito, T. Hirano, T. Maeda, M. Ono, Y. Murasaka, T. Imamura, T. Matsumaru, M. Yamaguchi, M. Sugawara, A. Azhari, H. Song, S. Sasada, and A. Iwata, "CMOS Gaussian monocycle pulse transceiver for radar-based microwave imaging," *IEEE Trans. on Biomedical Circuits and Systems*, vol. 14, no. 6, pp. 1333–1345, 2020.

[82] D. Oloumi, J. Ting, and K. Rambabu, "Design of pulse characteristics for near-field UWB-SAR imaging," *IEEE Transactions on Microwave Theory and Techniques*, vol. 64, no. 8, pp. 2684–2693, 2016.

[83] S. Kolpuke, C. D. Simpson, F. Abushakra, A. K. Awasthi, O. Reyhanigalangashi, J. Pierce, T. Luong, J. Larson, D. Taylor, D. Braaten, and S. P. Gogineni, "Airborne UWB FMCW radar for snow depth measurements," *IEEE Trans. on Geoscience and Remote Sensing*, vol. 60, pp. 1–15, 2022.

[84] R. Feghhi, D. Oloumi, and K. Rambabu, "Tunable subnanosecond Gaussian pulse radar transmitter: Theory and analysis," *IEEE Trans. on Microw. Theory and Techn.*, vol. 68, no. 9, pp. 3823–3833, 2020.

[85] A. D. Pitcher, C. W. Baard, and N. K. Nikolova, "Design and performance analysis of a picosecond pulse generator," *IEEE Transactions on Instrumentation and Measurement*, vol. 71, pp. 1–14, 2022.

[86] M. Mokhtari and M. Popović, "Novel antenna design for surface wave suppression in microwave breast screening," in *2023 IEEE MTT-S International Microwave Biomedical Conference (IMBioC)*, 2023, pp. 157–159.

[87] A. Martellosio, M. Pasian, M. Bozzi, L. Perregrini, A. Mazzanti, F. Svelto, P. E. Summers, G. Renne, L. Preda, and M. Bellomi, "Dielectric properties characterization from 0.5 to 50 ghz of breast cancer tissues," *IEEE Transactions on Microwave Theory and Techniques*, vol. 65, no. 3, pp. 998–1011, 2017.

[88] W. van Rossum, F. Nennie, D. Deiana, A. J. van der Veen, and S. Monni, "Dielectric characterisation of human tissue samples," in *The 8th European Conference on Antennas and Propagation (EuCAP 2014)*, 2014, pp. 524–528.

[89] A. P. O'rourke, M. Lazebnik, J. M. Bertram, M. C. Converse, S. C. Hagness, J. G. Webster, and D. M. Mahvi, "Dielectric properties of human normal, malignant and cirrhotic liver tissue: in vivo and ex vivo measurements from 0.5 to 20 GHz using a precision open-ended coaxial probe," *Physics in medicine & biology*, vol. 52, no. 15, p. 4707, 2007.

[90] S. Gabriel, R. Lau, and C. Gabriel, "The dielectric properties of biological tissues: III. parametric models for the dielectric spectrum of tissues," *Physics in medicine & biology*, vol. 41, no. 11, p. 2271, 1996.

[91] F. Di Gennaro, C. Baumgartner, E. Neufeld, B. Lloyd, M. Gosselin, D. Payne, A. Klingenbock, N. Kuster, and P. Hasgall. (2022, Feb.) IT'IS database for thermal and electromagnetic parameters of biological tissues.

[92] M. A. Richards, J. A. Scheer, and W. A. Holm, *Principles of Modern Radar, Volume I - Basic Principles*. SciTech Publishing, 2010.

[93] H. Nyquist, "Certain topics in telegraph transmission theory," *Transactions of the American Institute of Electrical Engineers*, vol. 47, no. 2, pp. 617–644, 1928.

[94] J. E. Quirk, R. J. Chang, J. W. Owen, S. D. Blunt, and P. M. McCormick, "A simple yet effective metric for assessing doppler tolerance," *IEEE Transactions on Radar Systems*, vol. 1, pp. 12–20, 2023.

[95] L. Zhang, C. Ding, X. Zhou, H. Hong, C. Li, and X. Zhu, "Body movement cancellation using adaptive filtering technology for radar-based vital sign monitoring," in *2020 IEEE Radar Conference (RadarConf20)*. IEEE, 2020, pp. 1–5.

[96] C. Sturm, T. Zwick, W. Wiesbeck, and M. Braun, "Performance verification of symbol-based OFDM radar processing," in *2010 IEEE Radar Conf.*, 2010, pp. 60–63.

[97] C. A. Schroth, C. Eckrich, I. Kakouche, S. Fabian, O. von Stryk, A. M. Zoubir, and M. Muma, "Emergency response person localization and vital sign estimation using a semi-autonomous robot mounted sfcw radar," *IEEE Transactions on Biomedical Engineering*, 2024.

[98] J. Liu, Y. Li, C. Li, C. Gu, and J.-F. Mao, "Accurate measurement of human vital signs with linear fmcw radars under proximity stationary clutters," *IEEE Transactions on Biomedical Circuits and Systems*, vol. 15, no. 6, pp. 1393–1404, 2021.

[99] Copper Mountain Technologies, "Optimizing VNA measurement speed," Application Note, Jan 2023.

[100] J. R. Klauder, A. C. Price, S. Darlington, and W. J. Albersheim, "The theory and design of chirp radars," *The Bell System Technical Journal*, vol. 39, no. 4, pp. 745–808, 1960.

[101] W. J. Caputi, "Stretch: A time-transformation technique," *IEEE Transactions on Aerospace and Electronic Systems*, vol. AES-7, no. 2, pp. 269–278, 1971.

[102] Texas Instruments, "Noise analysis in operational amplifier circuits," Application Report SLVA043B, 2007.

[103] B. Meyer, J. B. de Swardt, and P. van der Merwe, "Comparing baseband and intermediate frequency fmcw radar receivers," in *2017 IEEE AFRICON*, 2017, pp. 563–568.

[104] M. I. Skolnik, *Introduction to Radar Systems*, 2nd ed. New York: McGraw Hill Book Co., 1980.

[105] A. V. Oppenheim and R. W. Schafer, *Discrete-Time Signal Processing*, 3rd ed. USA: Prentice Hall Press, 2009.

[106] M. Koerner and R. Rogers, "Gain enhancement of a pyramidal horn using E- and H-plane metal baffles," *IEEE Transactions on Antennas and Propagation*, vol. 48, no. 4, pp. 529–538, 2000.

[107] F. J. Harris, "On the use of windows for harmonic analysis with the discrete Fourier transform," *Proceedings of the IEEE*, vol. 66, no. 1, pp. 51–83, 1978.

[108] K. Siddiq, R. J. Watson, S. R. Pennock, P. Avery, R. Poulton, and B. Dakin-Norris, "Phase noise analysis in fmcw radar systems," in *2015 European Microwave Conference (EuMC)*, 2015, pp. 1523–1526.

[109] J. Li, F. Rodrigue-Morales, J.-B. Yan, D. Gomez-Garcia, A. Masud, A. Patel, T. Gaynes, C. Leuschen, and S. Gogineni, "Deconvolution of fmcw radars for operation icebridge missions," in *2014 United States National Committee of URSI National Radio Science Meeting (USNC-URSI NRSM)*, 2014, pp. 1–1.

[110] J. Li, F. Rodriguez-Morales, E. Arnold, C. Leuschen, J. Paden, J. Shang, D. Gomez-Garcia, and C. Larsen, "Airborne snow measurements over alaska mountains and glaciers with a compact fmcw radar," in *IGARSS 2019 - 2019 IEEE International Geoscience and Remote Sensing Symposium*, 2019, pp. 3906–3909.

[111] R. E. Jarvis, J. G. Metcalf, and J. W. McDaniel, "Application of adaptive pulse compression in cluttered radar cross section measurements," *IEEE Transactions on Instrumentation and Measurement*, vol. 71, pp. 1–8, 2022.

[112] R. Bose, "Lean CLEAN: Deconvolution algorithm for radar imaging of contiguous targets," *IEEE Transactions on Aerospace and Electronic Systems*, vol. 47, no. 3, pp. 2190–2199, 2011.

[113] J. Tsao and B. Steinberg, "Reduction of sidelobe and speckle artifacts in microwave imaging: the CLEAN technique," *IEEE Transactions on Antennas and Propagation*, vol. 36, no. 4, pp. 543–556, 1988.

[114] D. Jenn, *Radar and Laser Cross Section Engineering, Second Edition*, 2nd ed., ser. AIAA education series. Washington, DC: American Institute of Aeronautics and Astronautics, Inc, 2005.

[115] P. van Genderen and I. Nicolaescu, "Imaging of stepped frequency continuous wave GPR data using the Yule-Walker parametric method," in *European Radar Conference, 2005. EURAD 2005.*, 2005, pp. 77–80.

[116] T. Sarkar and R. Brown, "An ultra-low sidelobe pulse compression technique for high performance radar systems," in *Proceedings of the 1997 IEEE National Radar Conference*, 1997, pp. 111–114.

[117] M. H. Ackroyd and F. Ghani, "Optimum mismatched filters for sidelobe suppression," *IEEE Transactions on Aerospace and Electronic Systems*, vol. AES-9, no. 2, pp. 214–218, 1973.

[118] B. Zrnic, A. Zejak, A. Petrovic, and I. Simic, "Range sidelobe suppression for pulse compression radars utilizing modified RLS algorithm," in *1998 IEEE 5th International Symposium on Spread Spectrum Techniques and Applications - Proceedings. Spread Technology to Africa (Cat. No.98TH8333)*, vol. 3, 1998, pp. 1008–1011.

[119] B. Zhao, L. Kong, M. Yang, and G. Cui, "Adaptive pulse compression for stepped frequency continuous-wave radar," in *Proceedings of 2011 IEEE CIE International Conference on Radar*, vol. 2, 2011, pp. 1780–1783.

[120] S. Blunt and K. Gerlach, "Adaptive pulse compression via MMSE estimation," *IEEE Transactions on Aerospace and Electronic Systems*, vol. 42, no. 2, pp. 572–584, 2006.

[121] S. M. Kay, *Fundamentals of Statistical Signal Processing: Estimation Theory*. USA: Prentice-Hall, Inc., 1993.

[122] L. Harnett, D. Hemmingsen, P. M. McCormick, S. D. Blunt, C. Allen, A. Martone, K. Sherbondy, and D. Wikner, "Optimal and adaptive mismatch filtering for stretch processing," in *2018 IEEE Radar Conference (RadarConf18)*. IEEE, 2018, pp. 0682–0686.

[123] S. D. Blunt, T. Chan, and K. Gerlach, "Robust DOA estimation: The reiterative superresolution (RISR) algorithm," *IEEE Transactions on Aerospace and Electronic Systems*, vol. 47, no. 1, pp. 332–346, 2011.

[124] L. A. Harnett, "Mismatched processing for radar interference cancellation," Ph.D. dissertation, University of Kansas, 2022.

[125] I. Reed, J. Mallett, and L. Brennan, "Rapid convergence rate in adaptive arrays," *IEEE Transactions on Aerospace and Electronic Systems*, vol. AES-10, no. 6, pp. 853–863, 1974.